ALTERNATIVE INVERSION STRATEGIES TO RESISTIVITY DATA FOR TARGETS WITH SHARP BOUNDARIES

by

Mehrez H Elwaseif

A Dissertation submitted to the

Graduate School-Newark

Rutgers, The State University of New Jersey

in partial fulfillment of the requirements

for the degree of

Doctor of Philosophy

Graduate Program in

Environmental Sciences

written under the direction of

Professor Lee Slater

and approved by

_____

_____

_____

_____

Newark, New Jersey

May, 2012

ABSTRACT OF THE DISSERTATION

Alternative Inversion Strategies to Resistivity Data for Targets with Sharp Boundaries

By Mehrez H Elwaseif

Dissertation director:

Professor Lee Slater

Estimating the geometry and resistivity of archeological structures using resistivity models produced as a result of applying smoothness constraints in most inversion algorithms is difficult, especially when structures are closely spaced. However, such quantification is important to facilitate conservation and to minimize the potential of damage when excavations are undertaken. Alternative inversion approaches more appropriate for imaging such targets require either a priori information about the subsurface (e.g. disconnected inversion) or require two or more geophysical datasets to be collected at the same site (e.g. joint inversion). The research outlined in this dissertation presents three novel approaches to improve resistivity imaging of discrete targets without the need to incorporate a priori information in the inversion. The first approach combines an initial 2D smoothness constraint inversion coupled with a digital image processing technique known as a watershed algorithms and a second inversion step incorporating a disconnect in the regularization based on the output of the watershed algorithm. This approach has improved estimate of the geometries of individual targets, but it was not very effective at predicting the resistivity of the targets or resolving closely spaced targets. The second approach combines an initial 2D smoothness constraint

inversion coupled with the watershed algorithm and a trained Artificial Neural Network (ANN). Although this approach has been proven effective for resolving widely and closely spaced archeological targets, the results depend largely on the quality of ANN training and on the accuracy of the watershed algorithm geometry prediction. Finally, the third strategy is an iterative approach that combines an initial 3D smoothness constraint inversion that is used only at the first iteration to recover a resistivity model that is fairly consistent with the measured data, from which an initial target location is estimated using an edge detector method and from which a disconnect in the inversion is identified. The disconnect defining the target outline is then progressively improved following each iteration of the inverse procedure. This approach has been proven more effective for resolving widely and closely spaced archeological targets over other approaches, but it is partially sensitive to artifacts in the initial smoothness constraint model.

Acknowledgments

All praise be to ALLAH (God), the sovereign of the heavens and the earth and those who dwell in them. My heartfelt thanks go to my parents who always support me and pray for me. I have many people to thank:

First and foremost, I would like to express my appreciation to my advisor Dr. Lee Slater for countless personal and academic helps and advises. His faith in my capabilities has served as a continual encouragement during my research. Dr. Dimitrios Ntarlagiannis, Dr. Kristina Keating and Dr. Jonathan Nyquist deserve particular thanks for their critical reviews of my work, and for serving as my committee members.

I would like to express my sincerest gratitude to Liz Morrin for many helps particularly when I first started my Ph.D. research and for making my life at Rutgers easy. A particular appreciation goes to Dr. Alexander Gates for being so supportive and helpful whenever I needed him. I also acknowledge the Rutgers Newark graduate school for awarding me a dissertation fellowship in the final year of my Ph.D. research. I am thankful to my colleagues in the National Research Institute of Astronomy and Geophysics, Egypt, for teaching me so much and for their continuous encouragement.

Finally, many thanks go to my wife for her incredible support and patience over the last year. Particular thanks go to my son for making me awake all the time, which indirectly helped me to finish this research on time.

TABLES OF CONTENTS

LIST OF TABLES

LIST OF ILLUSTRATIONS

Chapter 1: Introduction

1.1. Overview

Resistivity imaging is a popular geophysical method frequently used to predict the location of subsurface structures and objects having a detectable electrical resistivity contrast relative to the host medium. The method is routinely used to probe the shallow subsurface, common applications including mapping of near surface geology (Gokturkler et al., 2008; Chambers et al., 2006; Gibert et al., 2006), characterization of contaminated sites (Frohlich et al., 2008; Casas et al., 2007; Soupios et al., 2007), delineation of engineered structures (Marescot et al., 2008; Kemna et al., 2004), location of cavities (Leucci, 2006; El-Qady et al., 2005; Weinstein-Evron et al., 2003) and mapping of archeological features (Leucci et al., 2007; Urbini et al., 2007). The ability of the resistivity method to locate isolated features largely depends on the employed array configuration, unit electrode spacing, and the used inversion approach. The array configurations have different spatial resolutions and noise sensitivities (function of the position and the spacing between electrical and potential dipoles). The unit electrode spacing controls the depth of investigation and subsurface data coverage. The smoothness constrained regularization is widely used in inverting resistivity data, since the method does not require *priori* subsurface information and produces models that are highly consistent with the measured data (e.g. Loke and Dahlin, 2003). Smoothness regularization is typically applied using either smooth inversion (L2 norm) or robust inversion (L1 norm) (Loke, 2004). Regularization using a smoothness constraint results in models that contain minimal structure relative to some starting model (usually a

homogeneous medium) subject to fitting the measured data to a predefined level of accuracy (Loke and Barker, 1996b). This regularization constraint is inappropriate for imaging targets characterized by sharp change in resistivity relative to host medium (e.g., sinkholes, cavities, bedrock, etc.). Other inversion strategies more appropriate for defining sharp resistive targets such as disconnect or joint inversion can be utilized. However, time constraints in the field and lack of available subsurface priori information make these approaches difficult to apply for many field sites. More research is thus needed to develope a new resistivity inversion strategy that does not require a priori information, and is more appropriate for imaging targets with high resistivity contrasts. Such an inversion strategy would be appropriate for a wide range of applications particularly studies related to archaeological geophysics and engineering geophysics (e.g. locating sinkholes).

This dissertation presents three different inversion strategies to modify the smoothness constraint inversion in order to improve the geometry and resistivity recovery of archaeological targets without the need of incorporating a priori information in the inverse procedure. The first approach combines (1) an initial 2D inversion using the standard smoothness constraint and a homogeneous starting model, (2) an image processing technique known as the watershed algorithm to subsequently predict target dimensions (width and height) and depth from the smooth image, and (3) a second inversion step incorporating a disconnect in the regularization based on the output of the watershed algorithm. Although this approach resulted in an improved estimate of the geometries of individual targets, it was not very effective at predicting the resistivity of

the targets or resolving closely spaced targets. The second approach enhanced the previous approach by replacing the second disconnect inversion step with a trained Artificial Neural Network (ANN). This approach has been proven effective for resolving widely and closely spaced targets, but the processing steps are time consuming and the results depend largely on the ANN training. The third approach is a 3D resistivity inversion that combines smoothness constraint and disconnect inversion coupled with a digital edge detector technique called Roberts' cross-gradient operator to improve the inverted resistivity model through iterative updates of both the resistivity model parameters and the disconnect boundary. Although the approach is sensitive to the artifacts obtained from the initial smoothness constraint inversion step, it has been proven more effective for resolving widely and closely spaced targets than the other two approaches. The developed approaches as well as digital image processing, ANN, smoothness constraint and disconnect inversions are described in details in the next three chapters.

1.2. Objectives

The main objective of this research is to explore and develop alternative resistivity inversion strategies that are specifically designed to recover isolated and closely spaced targets representative of expected features at archaeological sites in Egypt. That objective was achieved by: [1] applying digital edge detector techniques such as watershed algorithm on smooth resistivity images coupled with disconnect inversion approach, [2] using artificial neural networks technique coupled with digital image processing and smoothness constraint inversion, and [3] developing an iterative 3D resistivity inversion

strategy that combines smoothness constraint inversion, digital image processing and disconnect inversion.

1.3. General findings

Digital image processing can be used explicitly or implicitly during the resistivity inverse procedures to improve imaging of high resistivity targets. The boundaries of targets predicted from the smooth resistivity images using edge detector techniques are consistent with the actual edges. In addition, those boundaries can subsequently be used to define disconnects in the inversion in order to estimate an updated model of the resistivity structure that better predicts the geometry and resistivity structure of the targets. Furthermore, a properly trained ANN appears to be a viable approach for determining the resistivity and location of discrete targets in resistivity datasets. Detailed interpretations and discussions of these findings can be found within the following related dissertation chapters.

Information is provided in the appendices that present further details on how to apply the described approaches, in addition to a related published research in archaeological geophysics. It contains a geophysical and hydrological study to characterize the near-surface setting and groundwater conditions at an archaeological site in Egypt.

Chapter 2: Quantifying Tomb Geometries in Resistivity Images Using Watershed Algorithms[1]

Abstract

Quantifying the geometries of archeological structures within resistivity models produced as a result of the regularization constraints used in most inversion algorithms is difficult, especially when structures are closely spaced. Here we apply the watershed by simulated immersion method of boundary detection to smooth 2D resistivity images generated for synthetic and field data over 3D targets. The synthetic studies include a single cavity model, a model for two widely spaced cavities (spacing >> unit electrode spacing) and a model for two closely spaced cavities (spacing < unit electrode spacing). We also examine a single-cavity model where a relatively resistive overburden, common at archaeological sites in Egypt, is included. In the case of the single cavity models, the maximum error for any geometries are 18% for the model without the resistive overburden and 10% for the model where the overburden is included, whereas it increases to 24% for the widely spaced model and 40% for the closely spaced model. Despite, the higher errors in the closely spaced cavity model, application of the algorithm confirms the presence of two features, which is not ascertainable from the smooth resistivity images. Boundaries detected with the watershed algorithm are subsequently used to define a disconnect in the regularization, resulting in a markedly improved estimate of the resistivity structure (particularly for the closely-spaced cavity model) in a

[1]This chapter is published as: Elwaseif, M., Slater, L., 2010, Quantifying Tomb Geometries in Resistivity Images Using Watershed Algorithms: Journal of Archaeological Science, Vol. 37, Issue 7, pp 1424-1436.

second inversion step using the model obtained from the smoothness constraint inversion as the starting model. This revised resistivity model also results in a lower root-mean-square (rms) misfit between measured and theoretical data, and between synthetic and inverted models. We demonstrate how the method can be applied on images from the archaeological site at Qurnet Murai, Luxor City Egypt.

2.1. Introduction

Resistivity imaging is a well established technology for predicting the location of subsurface structures and objects having a detectable electrical resistivity contrast relative to the host medium. The method is routinely employed to obtain an image of subsurface structures (i.e. the targets) in the absence of *a priori* information on the geometry and distribution of the targets. Under such conditions, the widely adopted smoothness regularization constraint is usually utilized to choose an inverted resistivity model that is, (1) consistent with the measured data (subject to some desired fitting criteria), and (2) geologically reasonable, from the large number of models that could fit the data equally well as a result of the underdetermined nature of the inverse problem (Gunther et al., 2006; Christiansen, and Auken, 2004). Smoothness regularization typically employs one of two minimization schemes, described here as smooth inversion and robust inversion (Loke, 2004). Smooth inversion emphasizes models with smoother variations of resistivity, whereas the robust inversion emphasizes models with sharper boundaries between regions of different resistivity.

Two dimensional resistivity inversion codes are based on the assumption that the subsurface is two dimensional. This assumption is not accurate in the case of imaging 3D bodies such as cavities. The 2D inversion assumes that there are no changes in the subsurface resistivity in the direction perpendicular to the survey line, which may leads to significant artifacts in the resultant model for 3D targets. Despite this limitation, 2D surveys and 2D inversion are still often used to image inherently 3D targets such as cavities (e.g., El-Qady et al., 2005), since fully 3D surveys are often cost-prohibitive and a substantial computational burden.

Regularization using the smoothness constraint results in models that contain minimal structure relative to some starting model (e.g., a homogeneous medium) subject to fitting the measured data to a predefined level of accuracy. However, resistivity imaging is increasingly used to predict the distribution of buried targets that are characterized by sharp, rather than gradational, resistivity contrasts. Archaeological features, e.g. tombs and walls (Negri et al., 2008; Negri and Leucci, 2006), are typically characterized by sharp resistivity contrasts. In this case, the smoothness constraint is conceptually inappropriate as our *a priori* expectation is that such targets represent a sharp change in resistivity across some unknown boundary location. Yet, the smoothness constraint is still often applied due to its 'off the shelf' availability and the fact that it at least provides a blurred representation of the distribution of such structures, usually predicting the center of such targets relatively well (for a single target or multiple targets separated by spaces considerably greater than the unit electrode spacing). However, the adoption of the

smoothness constraint makes it very difficult to reliably determine quantitative information on a discrete target, such as its dimensions or depth of burial.

Slater and Binley (2006) describe a modification of the smoothness constraint to accommodate sharp boundaries whereby a ‘disconnect’ in the smoothing is defined along the boundary of an object. This method requires that the boundary of the target be known a priori, and the inversion then solves for a smoothly varying model structure across the host medium and within the disconnected target. This constraint is conceptually consistent with many archaeological targets where resistivity may vary both within a structure with well defined boundaries and external to it, e.g., a foundation wall and the earth away from it. However, the need to know the location of the boundary a priori clearly limits the application of this technique. Recently, Blaschek et al. (2008) describe a complex resistivity inversion that incorporates a focused regularization scheme based on minimum gradient support that attempts to incorporate sharp boundaries without a priori information while still allowing for smooth model structure within the target and away from it. However, the main drawback of this approach is that a suitable smoothness parameter depending on priori information has to be determined by the user.

Here we describe an approach to imaging the location of tombs and cavities that combines (1) an initial 2D inversion using the standard smoothness constraint and a homogeneous starting model (as typically most often done in practice), (2) an image processing technique known as the watershed algorithm to subsequently predict target dimensions (width and height) and depth from the smooth image, and (3) a second

inversion step incorporating a disconnect in the regularization based on the output of the watershed algorithm to obtain an improved estimate of the variation in resistivity within and outside of the targets based on the incorporation of *a priori* data (the location of the disconnect and the resistivity model obtained from the standard smoothness constraint inversion). The approach assumes that the edges in the image predicted from the watershed algorithm are consistent with the edges of some unknown resistivity model characterized by sharp boundaries for which we have a smooth image.

Although we cannot expect such an algorithm to provide the perfect filter to remove the smoothing resulting from smooth regularization constraints in resistivity inversion, synthetic studies demonstrate the effectiveness of the watershed algorithm in estimating depths and dimensions for single and multiple cavity/tomb features representative of expected features at archaeological sites in Egypt. We also compare the results of implementing the watershed algorithm with the results obtained when implementing other edge detection methods (image gradient, curve evolution and snake method). Finally, we apply the approach on field data from sites in Egypt where the problem is the detection of unknown tombs. We recognize that the approach attempts to undo an initial regularization effect that is conceptually inconsistent with the resistivity model structure. However, given the current popularity of the smoothness constraint in commercially available (and academic freeware) resistivity imaging software, the method could be readily implemented by the archaeologist interested in imaging discrete targets.

2.2. Watershed algorithm by simulated immersion

Image processing techniques based on edge detection can be used to predict the location of sharp edges based on mathematical properties of the image parameter space. There are four basic edge detection techniques used in image processing; image gradient methods (e.g. Sobel, Prewitt, Roberts, or Canny operators), curve evolution, method of active contour (snake), and watershed algorithms. The success of the image gradient methods in detecting edges is based on the difference in grey level between the object and the background (Gonzalez and Woods, 1992). The method works well in locating single features, but typically fails in separating multiple objects due to the low grey level contrast within anomalies. The curve evolution technique is a powerful tool for extracting features with definite boundaries, but in the case of features with smooth boundaries, the method segments the boundary area into different contours based on the pixel intensity. The 'method of active contour' (snake) approach requires an initial user-defined selection within the image. However, the final solution differs for different initial selection, and moreover, its success is based on a high grey level contrast between the object and the surrounding region.

The watershed by simulated immersion is a powerful technique for segmenting a given image into regions with distinctive boundaries (Roueff et al., 2004; Barraud, 2006). In this study, we apply the method to predict the edges of features manifest in resistivity inversion results as smooth boundaries. Direct application of the method to smooth resistivity images produces problems such as over segmentation (i.e. the output segmented image has an excessively large number of regions), which can result from

noise (outliers) and/or significant resistivity variability (often smooth) in the host formation (e.g., moisture, lithological or pore water variation) at the scale of the resistivity survey. We therefore apply a sequence of pre-processing steps to increase the contrast between different pixels, reduce noise, and enhance the boundary between different features within the images. The order of these processing steps is described in Figure (2.1). The first step converts the 32-bit RGB (red, green, blue) input image into a 32-bit grayscale image more amenable to further processing (required only when not starting with a grayscale image). Gaussian blur and mean filters are then applied to preserve feature boundaries whilst reducing noise (extreme values) in the image by replacing each pixel with its neighborhood mean (Nixon and Aguado, 2002).

The first post-processing step is critical to determining an estimate of a target dimensions from the watershed algorithm. The watershed method predicts many boundaries depending on the complexity of the resistivity image, and so judgment must be applied to isolate the boundary that is associated with the anomalies in the resistivity images assumed to represent the cavities. Although a somewhat speculative exercise when multiple boundaries are present, the resistivity image can usually be used to make an informed choice on the boundaries associated with the cavity target. This boundary is then enhanced relative to all other detected boundaries associated with other changes in resistivity within the image e.g., due to change in moisture and/or pore chemistry across the site. This process is facilitated by selecting the cavity region (the region of interest (ROI)) and increasing the gray value intensity of this region. Finally, a threshold is applied to the resistivity image based on the maximum intensity value to enhance the

anomaly region and weaken all other boundaries. The final post-processing step is done simply to provide a rendition of the outline of the body. The Java-based image processing program, Image J, developed at the National Institutes of Health, was utilized to conducting all image processing steps, including the watershed algorithm (Burger and Burger, 2008).

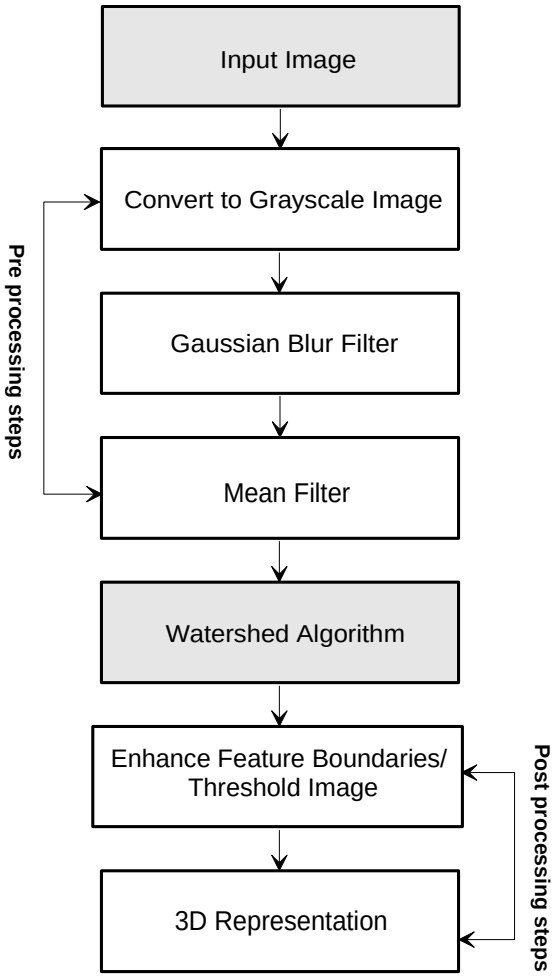

Figure 2.1: Flow chart showing the processing steps, centered on the use of the watershed algorithm, used in this study.

Beucher (1992) defines the watershed transformation by an immersion operation as follows; Let a grayscale image 'I' be considered a topographic surface (S) and the watershed lines and the catchment basins of 'I' be defined by means of a flooding process

(Roerdink and Meijster, 2001). If each minimum of the topographic surface has been pierced and the surface plunged at a constant vertical speed into a lake, then during the flooding two or more floods from different minima may merge. In order to avoid this merging, a dam is built on the points S where the floods would merge. At the end of the process, these dams separate various catchment basins, where each basin contains one minimum, this defining the watershed of the image (Roerdink and Meijster, 2001). The set of the catchment basins of *'I'* is equal to the set X_{hmax} obtained after the following recursion (Roerdink and Meijster, 2001),

$$X_{h_{\min}} = \left\{ \mathrm{P} \in D \mid I(\mathrm{P}) = h_{\min} \right\} = T_{h_{\min}} \tag{2.1}$$

$$X_{h_{\max}} = MIN_{h_{\max}} \cup IZ_{T_{h_{\max}}}(X_{h_{\max}-1}), \quad h \in [h_{\min}, h_{\max}] \tag{2.2}$$

where D is a set of pixels within a grayscale image, P is a vertex , $I: D \rightarrow N$ is a function assigning an integer value to each $P \in D$ (grayscale image takes integers from 0 to 255), h is a grey value (from 0 to 255), h_{max} is the maximum grey value in a grayscale image, X_h denotes the union of the computed set of basins at a grey value h, $IZ_{Th+1}(X_h)$ defines the skeleton by influence zones (SKIS), which consists of all equidistant points (in the sense of the geodesic distance) to at least two nearest connected components in X_h. Further, T_h is the threshold of the image at level h where;

$$T_h = P \in D \mid I(P) \leq h \tag{2.3}$$

According to the previous recursion, the iteration process starts at grey level $h_{min,}$ with all pixels potential candidates for getting assigned to a catchment basin “Equation 1”. At grey level $h_{\max}$ (i.e. equal 255), all non-basin pixels are potential candidates to become

new basins (first part of equation 2), and pixels which are equidistance to at least two nearest basins (geodesic distance) will be merged with a basin (second part of equation 2). A detailed description of the method and the pseudo code are given in Roerdink and Meijster (2001).

2.3. Synthetic models

The watershed method could be applied on the output model parameters from any resistivity code that employs the smoothness constraint in the regularization. We chose to use the Res2dInv program (Loke and Barker, 1996) for performing all inversions simply due to its popularity. We calculated the synthetic apparent resistivity pseudosections for a single cavity and two widely (separation >> unit electrode spacing) and closely spaced (separation < unit electrode spacing) cavities. We also consider a single cavity model that includes a resistive overburden to simulate fieldsites in Egypt. The 2D (i.e. measurements made along a line of electrodes) synthetic datasets were generated using a 3D forward modeling code, Res3dMod (Loke and Barker, 1996), to simulate real data collected in the field over cavity features by accounting for the 3D current flow and the 3D nature of the cavities. The cavities are assigned a resistivity (500-1000 Ohm m) consistent with infill of sediments/debris (the typical state prior to excavation), whereas the host medium is assigned a resistivity of 100 Ohm m, based on the results of previous studies (e.g., Elwaseif, 2006; El-Qady et al., 2005). In each case, thirty two electrodes were used to create the synthetic data and a dipole-dipole array was chosen due to its relatively high sensitivity to horizontal changes in resistivity (e.g., Dahlin and Zhou, 2004). An analysis of the resolution of electrical targets as a function of array type is beyond the scope of

this paper and can be found elsewhere (e.g., Furman et al., 2003; Dahlin and Zhou, 2004; Stummer et al., 2004). The electrode spacing used here was 1 m and six depth levels (integer dipole spacings) were utilized. To improve subsurface resolution additional measuring points were added in-between these depth levels, providing 390 measurements and a maximum investigation depth of about 4.5 m based on theoretical relations between electrode spacing/geometry and investigation depth for a homogeneous earth medium (e.g., Loke, 2004).

Four model scenarios were created, known to be generally representative of target depths/dimensions of cavities of interest at archaeological sites in Egypt (as we show later). In the first scenario, a single cavity was buried at 1.2 m depth, having a width and a length of 4 m and resistivity of 1000 Ohm m (Figure 2.2a). The second scenario involved two cavities having resistivity values of 500 and 1000 Ohm m. Two cases of this two cavity model were considered (a) a widely-spaced cavities model involving cavities with widths/lengths of 4 m and outside edges spaced 4 m apart (Figure 2.4a); (b) a closely-spaced cavities model involving cavities with widths/lengths of 2.8 and 2.7 m and outside edges spaced 0.6 m apart (i.e. less than the unit electrode spacing) (Figure 2.5a). In the last scenario, a single cavity was buried at 1.9 m depth, having a width of 4 m and resistivity of 1000 Ohm m, overlain by a high resistivity (3000 Ohm m), 1.4 m thick layer (Figure 2.6a). All synthetic datasets were contaminated with 2% Gaussian noise, representative of noise levels (based on repeatability tests) at the archaeological sites of interest in Egypt.

2.3.1. Resistivity Inversion: Smooth vs. robust model norms

As previously explained, we elected to perform a 2D inversion of the datasets generated using 3D forward modeling as this best represents the typical situation for real datasets: i.e., cavity features are inherently three dimensional but 2D datasets and 2D inversion of these 3D features (and 3D current flow) is, more often than not, the norm. The objective of regularized resistivity inversion is to find a model that contains a resistivity structure consistent with expectations regarding the likely distribution of resistivity within the subsurface, whilst providing a set of theoretical measurements (forward response) that fit the measured data to some pre-described acceptable level (here quantified by the root-mean-square (rms) error between the predicted dataset for model solution and the measured dataset) (e.g., Loke et al., 2003; Gunther et al., 2006).

As very little is commonly known *a priori* about the subsurface, by far the most common regularization method employed is to find the model with the minimum required structure (or minimum deviation from a homogeneous earth model) that fits the measured data to the pre-described level. An objective function is typically defined that contains a term related to minimizing the differences between the theoretical data and the measured resistances (data misfit), and a term related to minimizing model structure (model misfit).

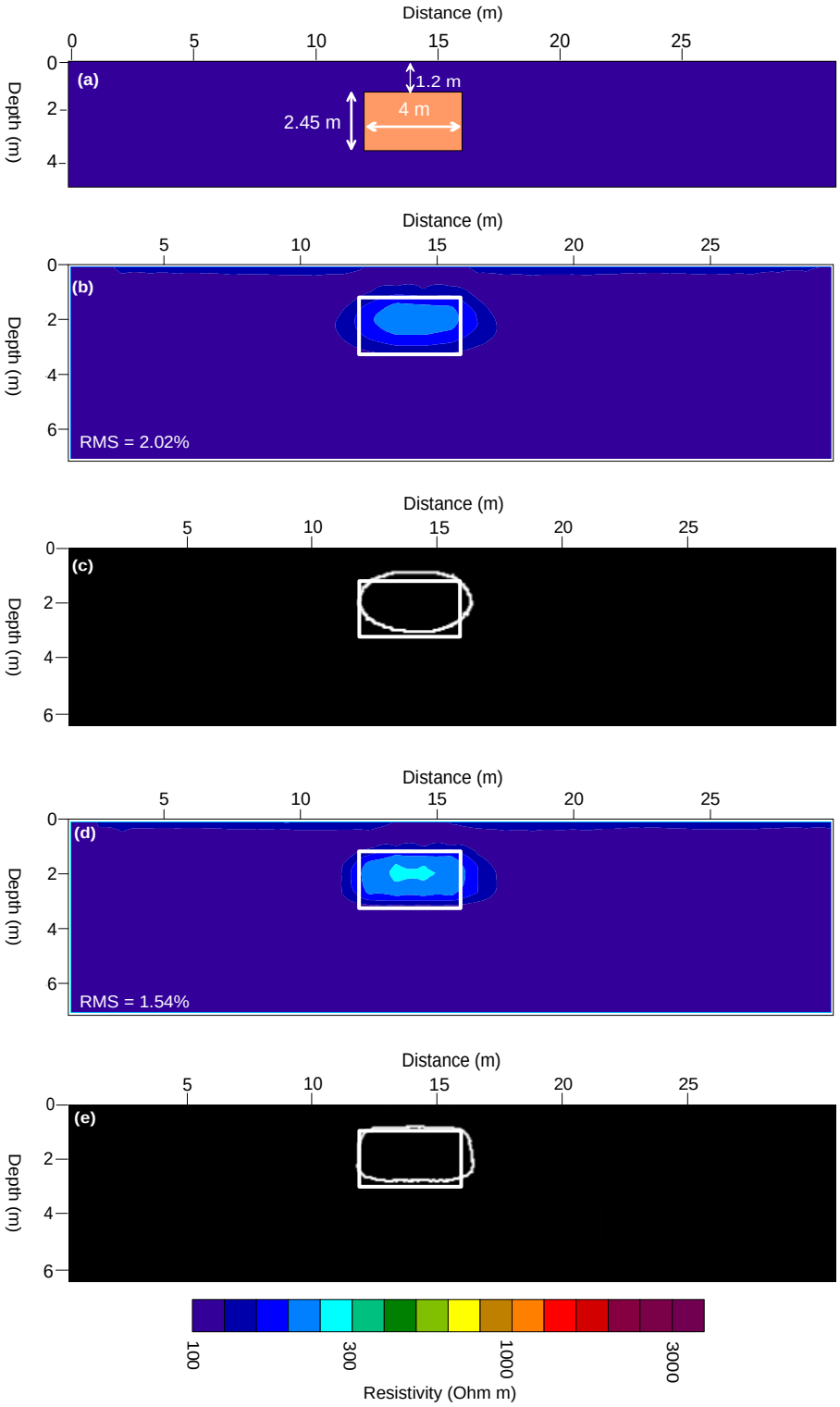

Figure 2.2: Results of applying the watershed by immersion technique on the single cavity model (a) subsurface model (b) smooth section (c) detected boundary based on b (d) robust inversion (e) detected boundary based on d (white boxes denote true cavity outline)

It is most common to minimize the squares of the differences between the measured and modeled (theoretical) transfer resistances and/or differences between the estimated model and expected model structure (L2 norm). This method typically produces a smooth distribution of resistivities over a broad range of values and is defined here as the smooth inversion. Minimization of the absolute differences between measured and modeled resistivity values (and/or differences between the estimated model and expected model structure) (L1 norm) typically results in sharper boundaries between regions with different resistivity values, although resistivity values vary less within each region (Loke et al., 2003).

The L1 norm (hereby referred to as the robust inversion) is intuitively more appropriate for imaging cavities/tombs than the L2 norm as we expect such cavities to represent sharp contrasts with the host medium at distinct boundaries. However, as real cavities are filled with a heterogeneous mixture of sediments prior to excavation some variability of resistivity within the cavity boundary is possible (although not considered in our synthetic trials). For completeness we show the results obtained with both the robust and smooth inversion. In all cases a homogeneous medium was used as the starting model, the data misfit weights were assigned based on a 2% error in the measured data and five iterations were performed. The results of applying the inversion on the single, widely spaced, closely space cavity, and the synthetic model of the field site are presented in Figures 2.2, 2.4, 2.5 and 2.6, respectively. In each case the smooth inversion is shown in part ‘b’ of the figure and the robust inversion is shown in part ‘d’ of the figure.

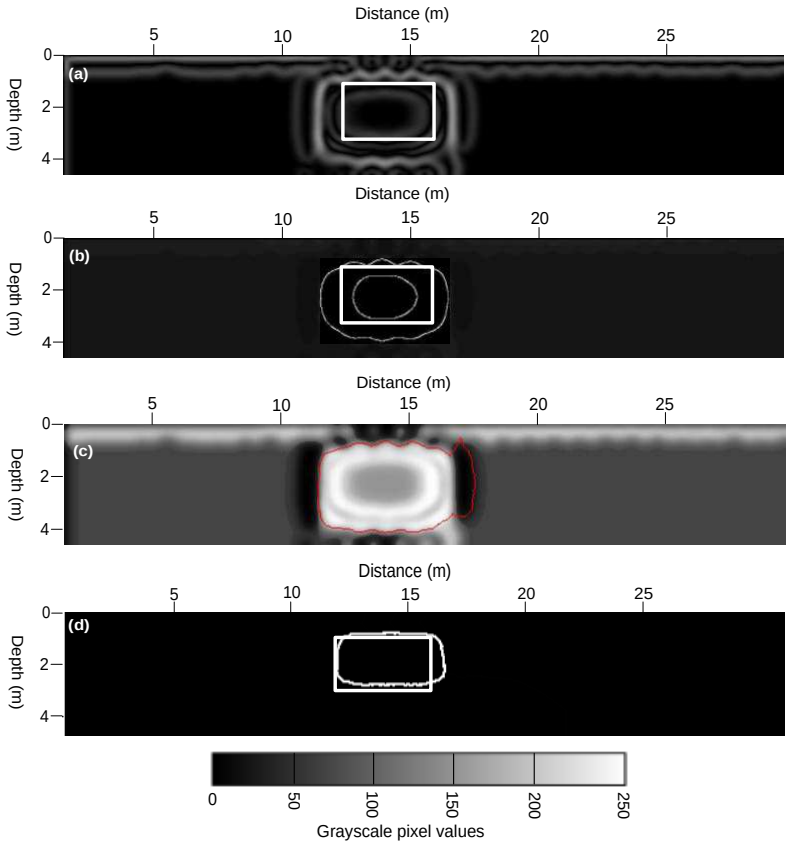

Figure 2.3: Results of applying the image gradient, curve evolution, and the snake methods on the single cavity model (a) boundaries based on image gradient (b) boundaries based on curve evolution method (c) snake model (after 500 iterations) (d) boundaries based on watershed algorithms (boxes denote true cavity outline)

White outlines show the true cavity dimensions. The rms errors for each inversion are included in the figures. As expected, the inversion produces smooth models of the true resistivity structure associated with the cavities. The models from the robust inversion are less smooth, with sharper boundaries and less resistivity variation within the model space represented by the cavities. The widely spaced cavities are clearly associated with individual anomalies in the resistivity images (Fig. 2.4b). However, the two closely spaced cavities in both smooth and robust images appear as a single anomaly, instead of

two separate features, due to the small spacing between cavities (here less than the unit electrode spacing).

To assess performance of the robust and smooth inversions in a more quantitative way, the data misfit (relative to the noisy synthetic data) and model misfit (relative to the known synthetic model) curves are plotted at all five iteration steps for the different model scenarios in Figure 2.7. Although data misfits are very low for all models, the model misfits are significantly lower in the case of robust inversion.

2.3.2. Predicted locations from the watershed algorithm

The watershed by simulated immersion method was applied on the inverted resistivity images to locate the boundaries of the cavities and to compare the estimated boundaries with the true boundaries of the resistive targets in the synthetic models. The results from application of the watershed algorithm are summarized in Table 2.1, showing the mean depth, width and length of each boundary associated with a cavity estimated by the watershed algorithm. Figure (2.2c & 2.2e) shows the results of applying the watershed method on the smooth and robust images for the single cavity. The detected cavity boundary of the smooth image has an average error of 14%, while the average error for the robust image is ~ 18%. Although the average error is less for the smooth image, the shape of the detected cavity boundary of the robust image better reflects the actual shape of the subsurface model (i.e. rectangular).

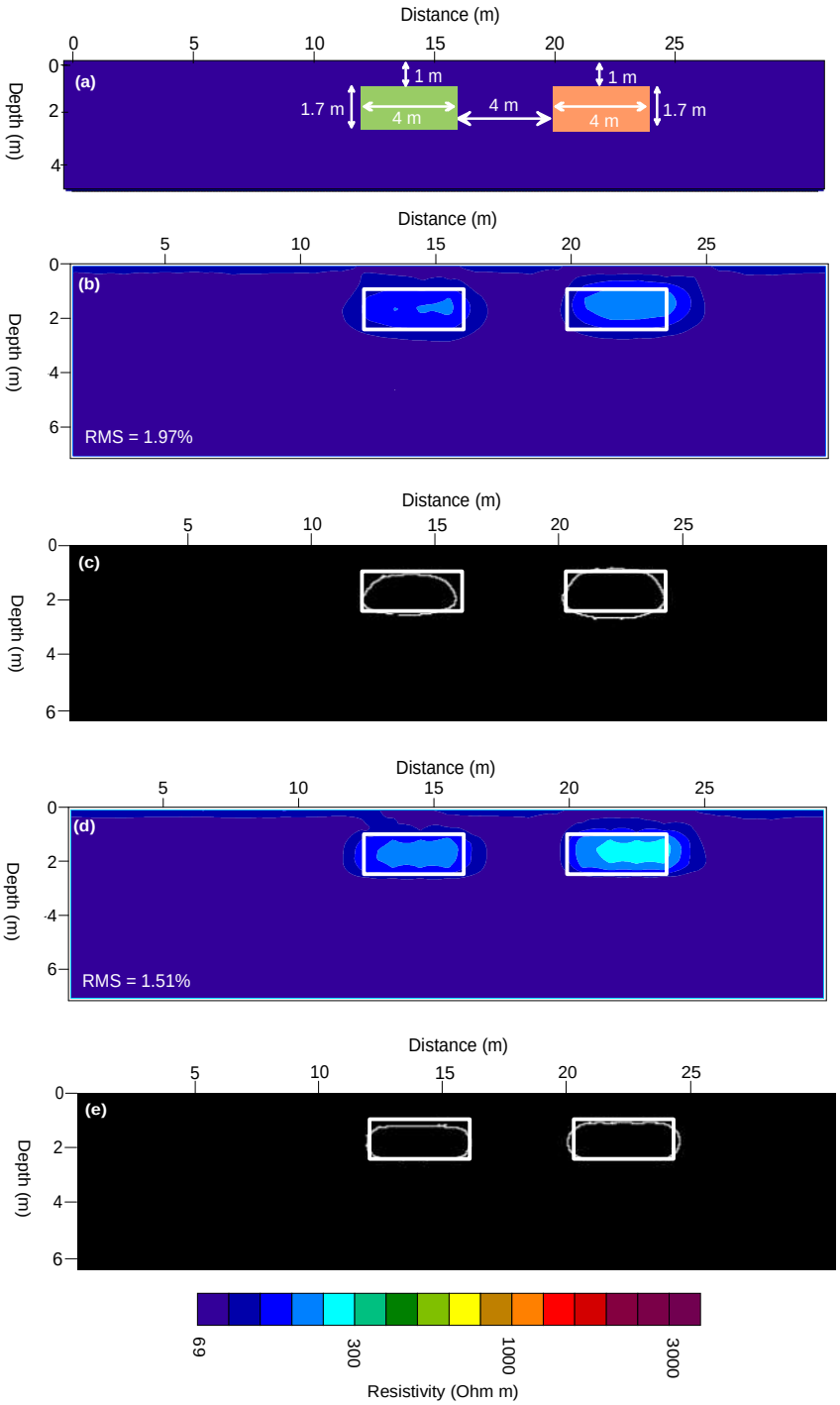

Figure 2.4: Results of applying the watershed by immersion technique on the widely spaced cavities (a) subsurface model (b) smooth section (c) detected boundary based on b (d) robust inversion (e) detected boundary based on d (white boxes denote true cavity outline)

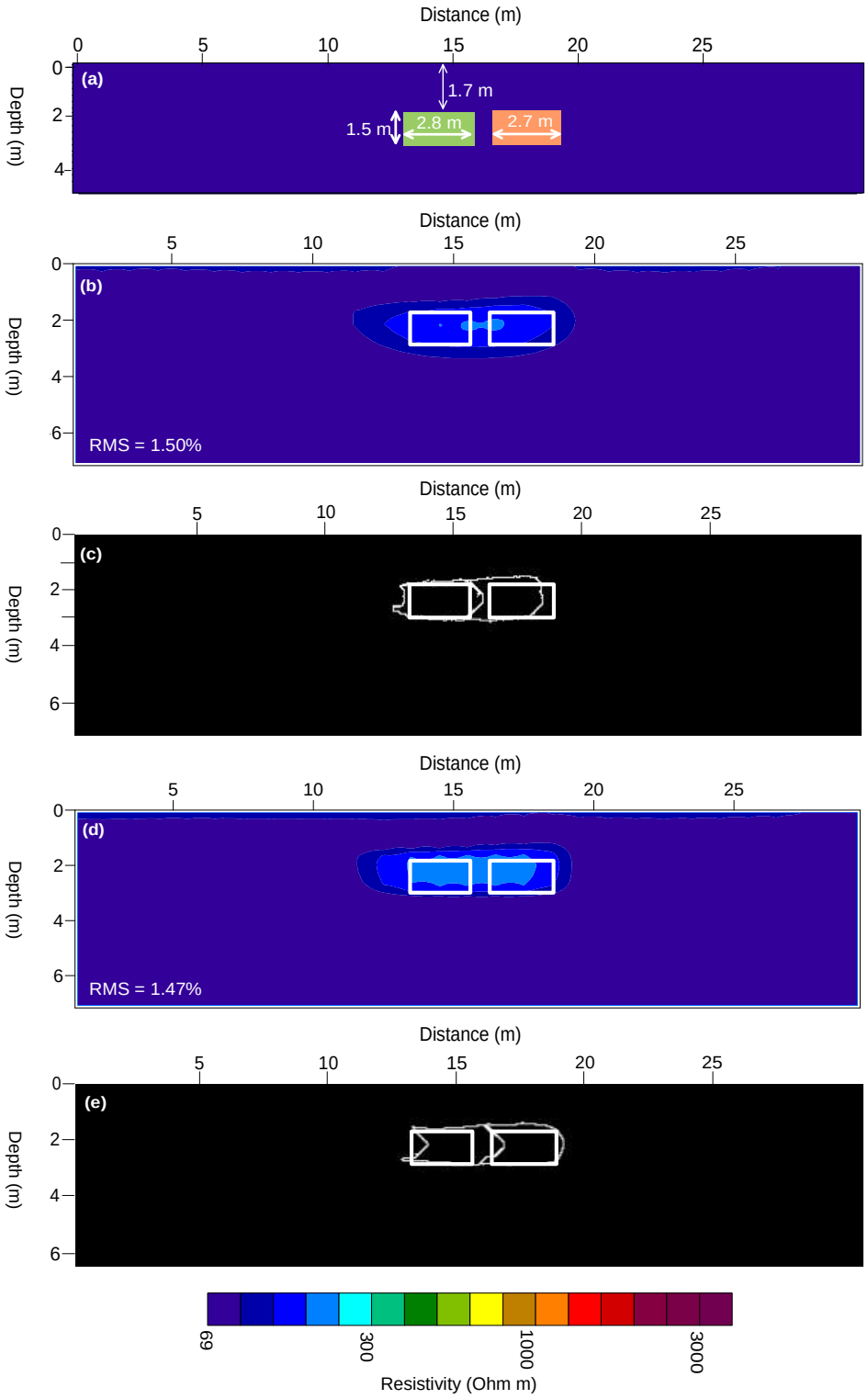

Figure 2.5: Results of applying the watershed by immersion technique on the double cavity model (a) subsurface model (b) smooth section (c) detected boundary based on b (d) robust inversion (e) detected boundary based on d (white boxes denote true cavity outline)

To compare the effectiveness of the watershed method relative to other edge detection techniques, the image gradient, curve evolution, snake method and watershed algorithm were also applied on the inverted image of the single cavity model. Note that identical pre-processing steps were used for each method (Figure 2.1). The results of applying these techniques are shown in Figure 2.3 and summarized in Table 2.2. The watershed algorithm predicts the cavity dimensions with significantly less error than all other edge detection methods tested here, since the success of other methods depends mainly on the presence of high grey level contrast between the object and the background (not the case in the single cavity model). The average error of the watershed method is 16% (based on the three dimensions), while the errors of the Snake and image gradient methods are 43% and 34%, respectively. Note that the curve evolution method located multiple edges (i.e. multiple widths, heights, and depths) making it impractical to assign a single edge as representative of the cavity boundary.

Figure 2.4c & 2.4e shows the results of applying the watershed algorithm on the widely spaced cavity for smooth and robust models respectively. Table 2.1 summarizes the effectiveness of the algorithm in predicting the boundaries of the two cavities. The average error of the method for locating the cavities in the smooth model is 4%. In contrast, for the robust model it is 6.5%.

The results of applying the watershed algorithm on the closely spaced cavities for smooth and robust models are shown in Figures 2.5c & 2.5e respectively. The method predicts a boundary in the resistivity anomaly associated with the closely spaced cavities, despite

that evidence for this boundary cannot be visually ascertained from the inverted image of resistivity variation. In this case, the cavity boundaries estimated from the robust image are more accurate than those obtained from the smooth image. The average error of the method in estimating cavity dimensions in the smooth image is 6 % relative to 10 % in the robust image. Figure (2.6c & 2.6e) shows the results of applying the watershed method on the smooth and robust images for the synthetic model of the field site incorporating the resistive upper layer. The detected cavity boundary of the smooth image has an average error of 12%, while the average error for the robust image is 16%. We note that the technique also successfully predicted the thickness of the top resistive layer in both robust and smooth images, where the average error for both robust and smooth images is 11%.

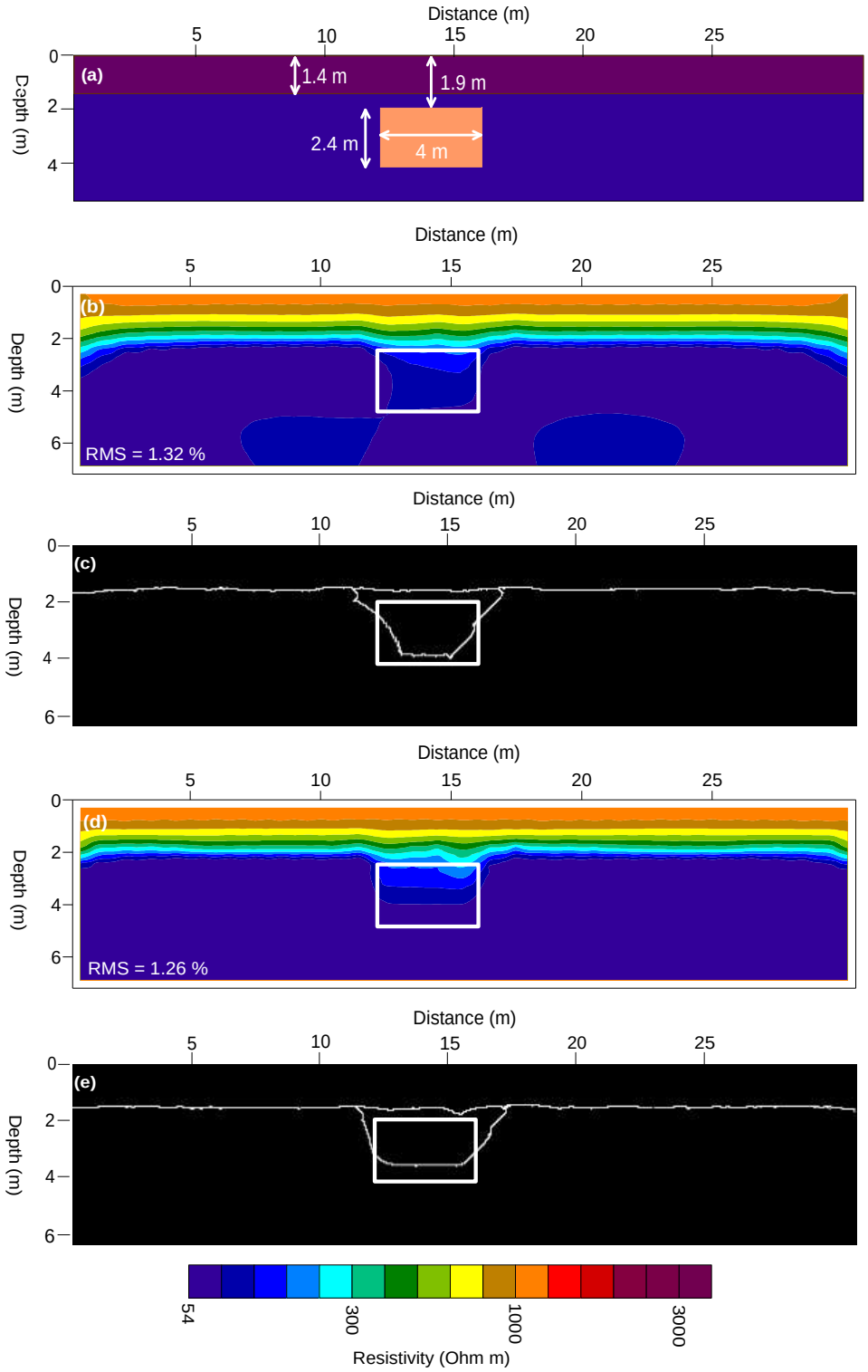

Figure 2.6: Results of applying the watershed by immersion technique on the synthetic field data model (a) subsurface model (b) smooth section (c) detected boundary based on b (d) robust inversion (e) detected boundary based on d (white boxes denote true cavity outline)

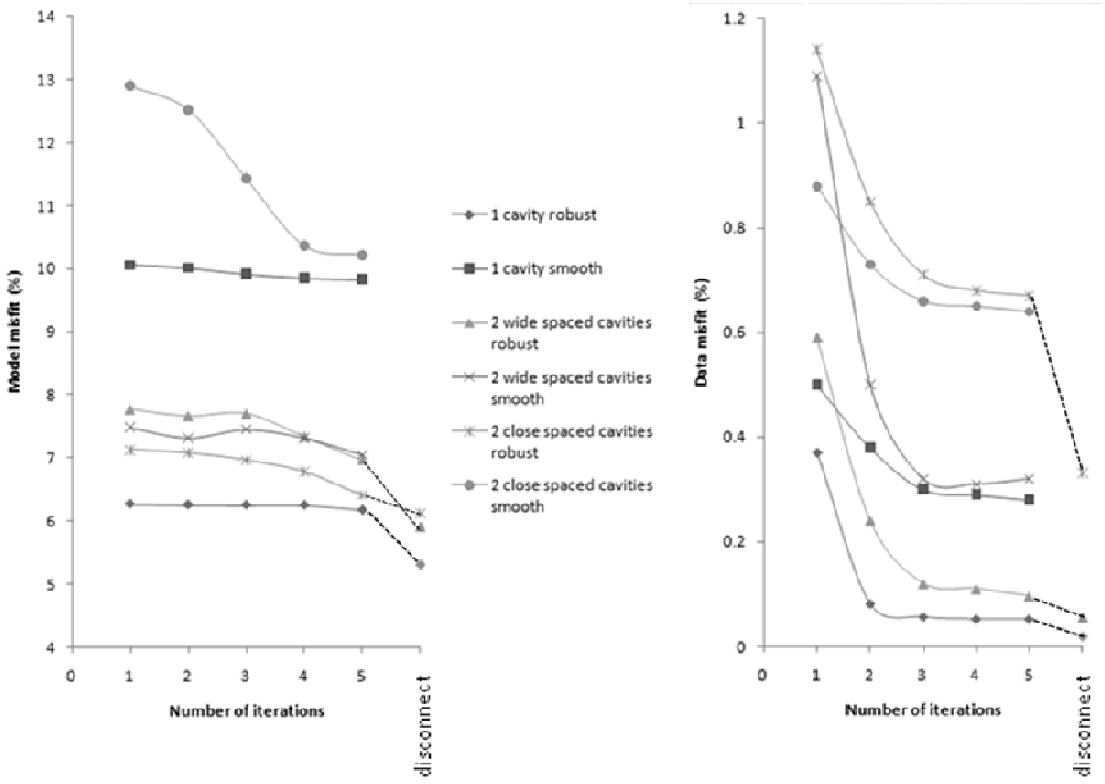

Figure 2.7: Model misfit and data misfit curves for the synthetic studies conducted here. The progress of the misfits for five iterations are shown, along with the misfit following the use of the disconnect (final iteration) where applied

2.3.3. Re-inverting datasets using a disconnect boundary in the regularization

Once boundaries are estimated, it is possible to incorporate this as *a priori* information and subsequently re-invert the dataset using the disconnect approach (Slater and Binley, 2006), where the inversion solves for smooth model structure within the cavities and within the background, but prevents any smoothing of model structure across the boundaries. However, it is important to verify that the predicted edges applied to the regularization result in a model that fits the data at least as well as the model obtained

without this constraint as, in the case of field data (where the model structure is unknown), it is possible that unrealistic edges could be inferred from the processing. Re-inverting the data with this additional constraint on the inferred location of cavity boundaries could lead to an improved estimate of resistivity structure within the host medium or even within the target.

Table 2.1, quantitative analysis of the accuracy of the watershed algorithm by simulated immersion method, where 'D' – depth, 'W'– width, 'H' – height, and 'Th' – upper layer thickness.

Resistivity Models	Inversion approach	True dimensions (m)				Estimated dimensions (m)				Error (%)			
		D	W	H	Th	D	W	H	Th	D	W	H	Th
One cavity	Smooth	1.2	4	2.45	-	0.9	4.3	2.2	-	25	7	11	-
	Robust					0.8	4.3	2.1	-	33	7	14	-
Two cavities-widely spaced	Smooth	1.0	4.0	1.7	-	1.0	3.8	1.8	-	0	5	6	-
						1.0	4.0	1.9	-	0	0	12	-
	Robust	1.0	4.0	1.7	-	1.2	4	1.5	-	20	0	12	-
						1.0	4.3	1.7	-	0	7	0	-
Two cavities-closely spaced	Smooth	1.7	2.8	1.5	-	1.7	2.6	1.5	-	0	7	0	-
						1.6	2.4	1.4	-	6	14	7	-
	Robust	1.7	2.7	1.5	-	1.6	3.1	1.4	-	6	15	7	-
						1.4	2.9	1.6	-	18	7	7	-
Synthetic field site model	Smooth	1.9	4	2.4	1.4	1.7	3.7	2.2	1.7	11	8	8	21
	Robust					1.7	4.4	1.9	1.7	11	10	21	21

Figure 2.8 shows the final inverted images of the single cavity, widely spaced double cavity, closely spaced double cavity and single cavity with resistive overburden models after robust inversion using the disconnect constraint based on the predicted boundaries from application of the watershed algorithm to the robust inversion (i.e. watershed

predicted boundaries shown in Figures 2.2e, 2.4e, 2.5e and 2.6e respectively). The Res2dInv program was used for

Table 2.2, Comparison between the results of different edge detection methods for the single cavity model

Edge detection method	Estimated dimensions (m)			Error (%)		
	Depth	Width	Height	Depth	Width	Height
Snake	0.7	6	3.3	42	50	35
Watershed	0.9	4.3	2.2	25	7	11
Curve evolution	-	-	-	-	-	-
Image gradient	0.7	5	3.3	42	25	35

the disconnect robust inversion (Loke and Barker, 1996). In each case, we use the model result obtained from the smooth inversion as the starting model for this second inversion step employing the disconnect (i.e. images shown in Figures 2.2d, 2.4d, 2.5d and 2.6d respectively). The disconnect inversion results in an improved recovery of resistivity structure of the single cavity and widely spaced cavity models relative to that obtained without the use of the disconnect constraint (Figure 2.4). The improvement in both model misfit and data misfit is most obvious from the data and model misfit curves shown in Figure 2.7. Most obviously, the inversion of the closely spaced model now clearly depicts the presence of two resistive features coincident with the cavities. Consistent with the true model, the cavity on the right is predicted as the more resistive. The inversion of the synthetic field model also results in improved recovery of resistivity structure relative to that obtained without using the disconnect in the inversion (Figure 2.6).

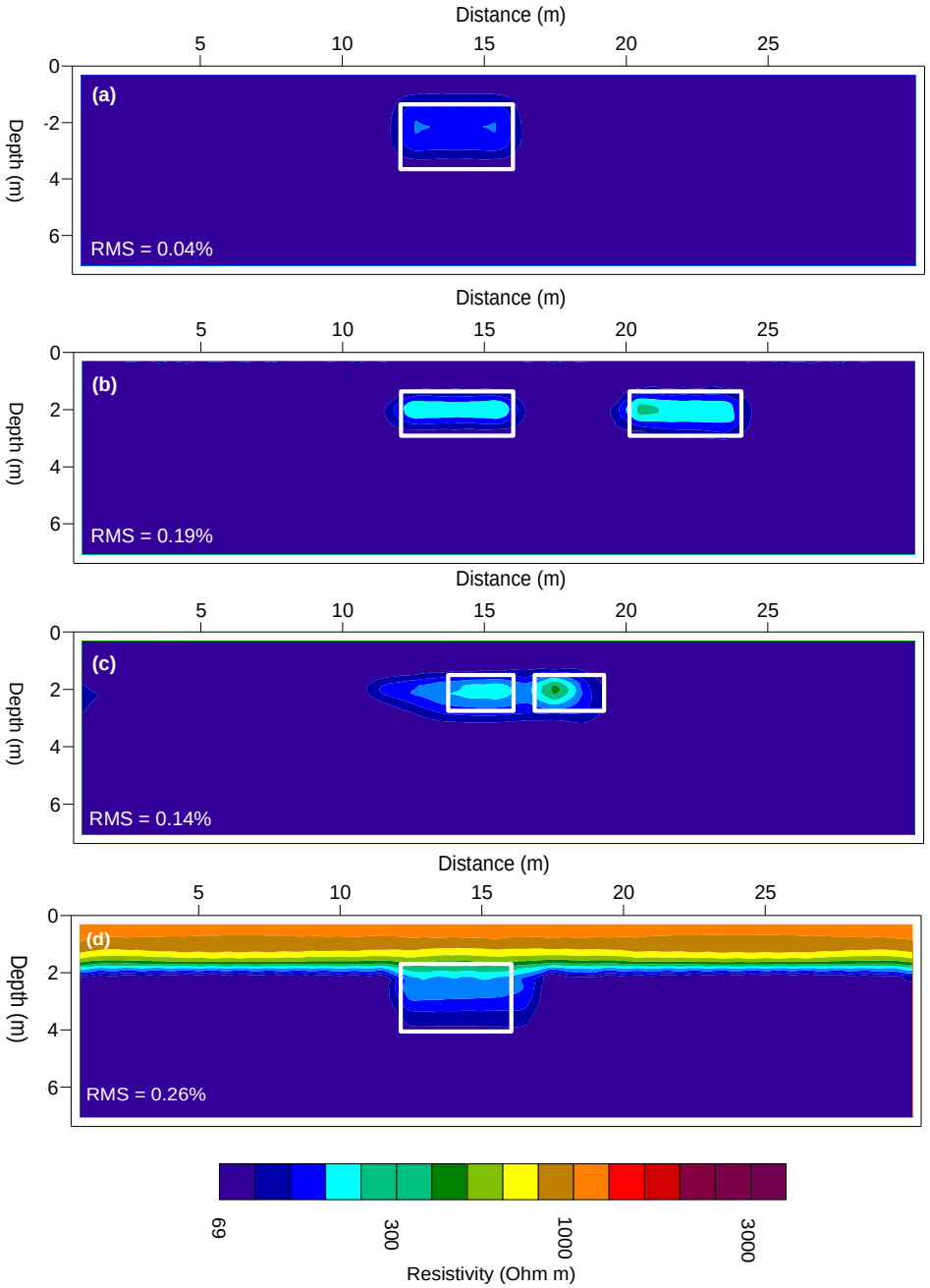

Figure 2.8: Disconnect inversion results for the single cavity, widely and closely spaced cavities, and for the synthetic field site model (a) single cavity model (b) widely spaced cavities (c) closely spaced cavities (d) synthetic fieldsite model (white boxes denote true cavity outline)

2.4. Application to real data: Mapping cavities in Qurnet Murai

In order to illustrate this image processing approach on field datasets we applied the watershed by simulated immersion processing on datasets acquired from Qurnet Murai, Egypt (Figure 2.9). The site is located about 30 m to the west of Merenptah temple and

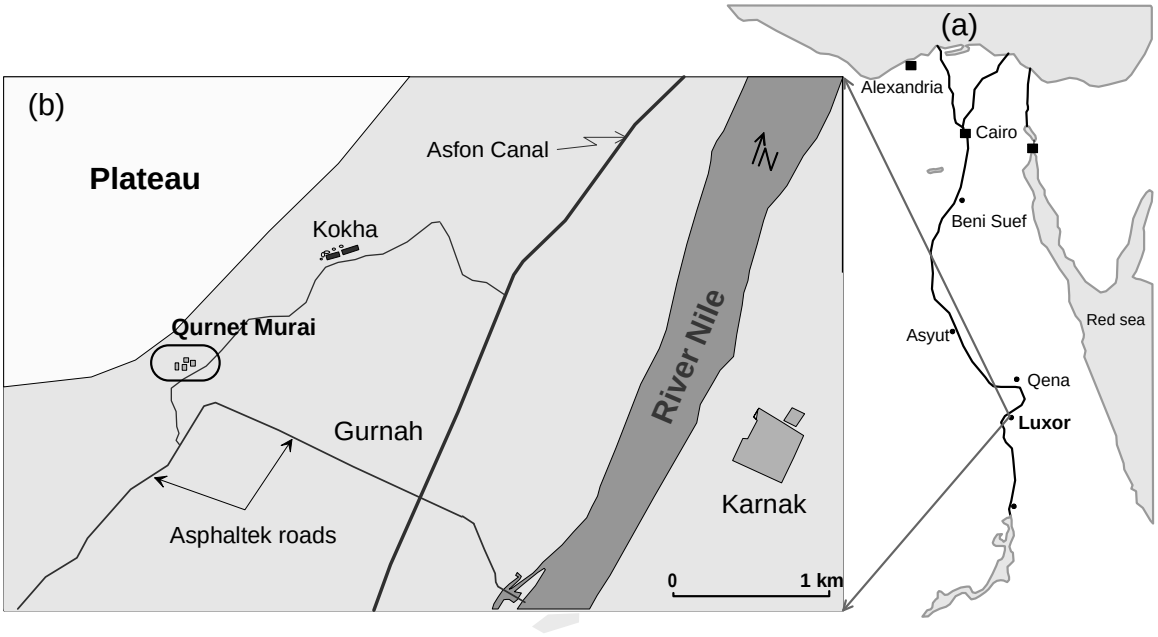

Figure 2.9: location map of a- Egypt, and b- the western bank of Luxor

near the western limestone plateau of Luxor. The western bank of Luxor contains more than thirty known temples, such as Hatshepsut, mostly built by the rulers of the new Kingdom (1549-1069 BC) (Baines and Malek, 1980). Geophysical surveys have been conducted at this site in an effort to locate undiscovered artifacts, primarily tombs such as that shown in figure 2.9. Note that the photos in Figure 2.10 show the features after excavation of soil, debris and antiquities that typically fill these features *in situ*. These geophysical surveys include eight parallel 2D resistivity lines, 32 m long and spaced 5 m

apart, that were acquired during a field effort in May 2006. A 2D dipole-dipole array with 1 m electrode spacing and 6 depth levels was acquired with a Syscal R1 (Iris Instruments, France) automatic resistivity system, providing 111 measurements on each parallel line, with a modeled maximum investigation depth of about 4 m. Due to time constraints in the field, the additional quadripoles used in the synthetic modeling described previously were not collected during this experiment.

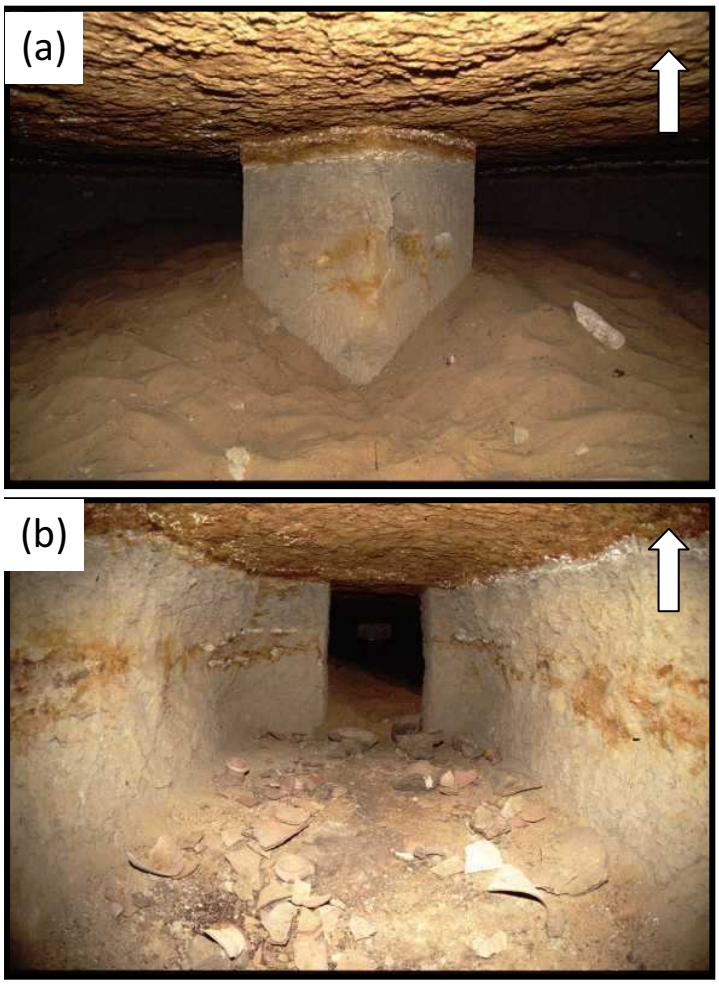

Figure 2.10: Examples of expected artifacts at the archaeological sites in Saqqara, Egypt, (a) buried tomb, and (b) tunnel leading to a tomb (~ 5 m x 2 m). Such artifacts represent resistive targets likely to be detected with electrical methods. Note that, in both cases, the photos show the cavities post excavation, following removal infilling soil, debris and artifacts. Arrow denotes direction towards surface

The inversion followed the same processing steps as described in Figure 2.1 and as performed on the synthetic datasets. Figure (2.11a) shows an inverted resistivity profile along one of the eight parallel lines obtained using the robust inversion and a homogeneous starting model. The section displays a wide range of resistivity values.

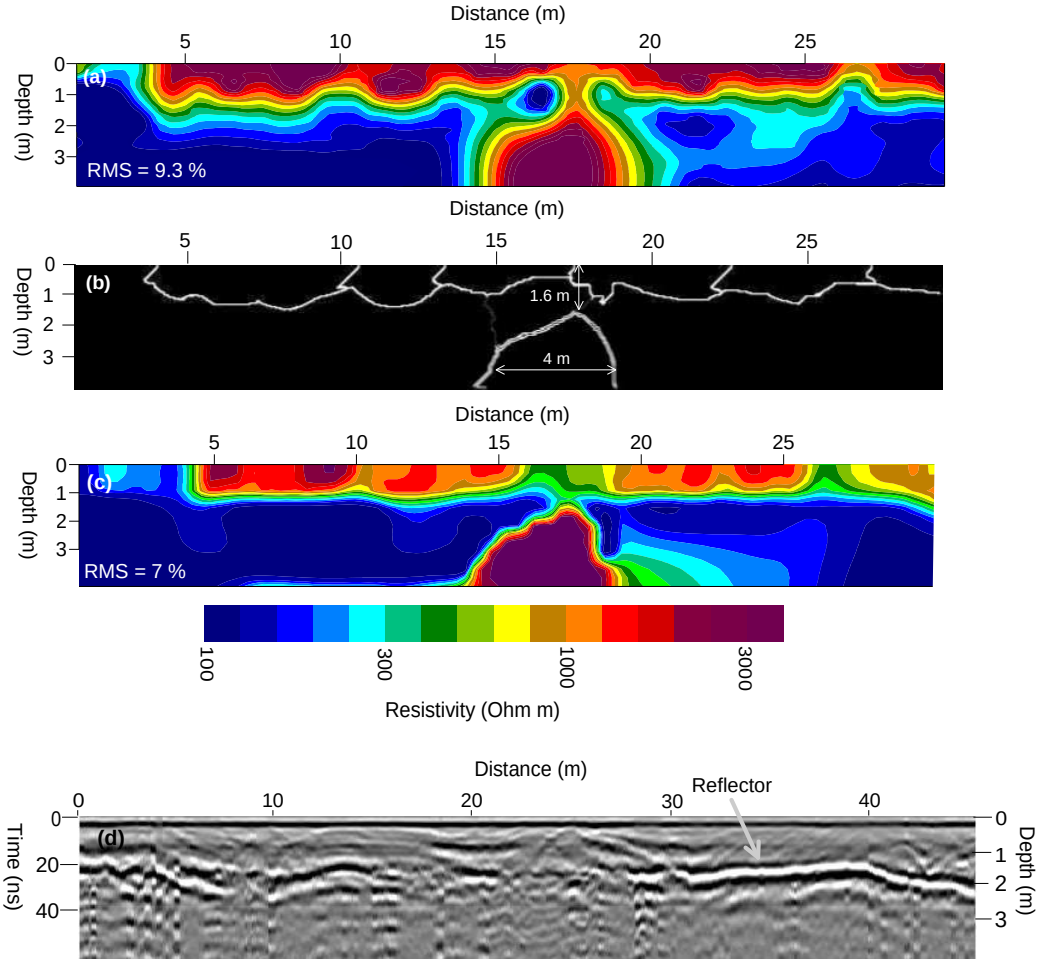

Figure 2.11: Results of the watershed application on the western bank of Luxor resistivity profile (a) Res2dinv section (b) detected boundaries based from 'a' (c) disconnect inversion model (d) Collected GPR profile using 200 MHz shielded antenna, trace increment of 0.05 m, and an average velocity of 0.136 m/ns estimated from the hyperbolic shapes in the figure.

The top resistive layer (~ 3000 Ohm m) is often encountered in this environment due to very dry sediments on the earth's surface (high temperatures, regularly reaching 46°C at this site, result in very low moisture contents due to evaporative loss). Beneath this surface layer, resistivities are much lower, ranging from 20-300 Ohm m, primarily due to increasing moisture content with depth. An anomalous relatively high resistivity zone (between 1-3.5 m depth) occupies the area between 16 to 20 m along the line and is believed to relate to a cavity filled with friable soils.

The results of applying the watershed by simulated immersion technique on Figure 2.11a is shown in Figure 2.11b. A number of boundaries are predicted in the near surface and reflect the upper resistive layer. One boundary is detected at depth and associated with the cavity. Based on this model, the cavity is located at 1.6 m depth and is 4 m wide (Fig. 2.11b), which is consistent with the excavations shown in Figure 2.10. The dataset was then re-inverted using all boundaries determined in Figure 2.11b with the model shown in Figure 2.11a as the starting model. This disconnect inversion result is presented in Figure (2.11c). The root mean square (RMS) error between the theoretical and measured data was 9.3% without using the disconnect boundary in the inversion, compared with 6.6% after employing it.

In addition to predicting the cavity boundaries, we note that the watershed method also detected the boundary between the resistive upper layer and the underlying half space. The estimated depth of this boundary, varying from ~ 1m to 1.5 m, is consistent with a horizontally continuous reflection recorded in a radar profile collected very close to the

resistivity line (Figure 2.11d). This GPR profile was collected using the common-offset method. The GSSI Subsurface Interface Radar (SIR) System-2000 equipped with 200 MHz shielded antenna was employed for the data collection. The number of traces, number of samples per trace, trace increment, and time increment were 899,512, 0.05 m, 0.195 ns, respectively. A strong GPR reflection at 20-30 ns (1-1.5 m depth based on a velocity of 0.136 m/ns calculated from diffraction hyperbolae in the data), at a depth consistent with the boundary identified in the resistivity image, suggests that it results from an increase in soil moisture at depth.

2.5. Discussion and conclusion

We have shown that the boundaries of cavities predicted using the watershed algorithm are consistent with the edges of resistivity models characterized by sharp boundaries for which we only have a smooth resistivity model. However, the success of the watershed algorithm to predict accurate target boundaries depends on the success of the inversion in reconstructing the investigated targets. The performance of the watershed algorithm will vary depending on the minimization procedure used (e.g. smooth vs robust) as shown here. The effect of the watershed algorithm will also likely depend on the inversion code used, although this is beyond the scope of our paper. Clearly, the final image produced following the disconnect inversion is very sensitive to the definition of the boundary extracted from the watershed algorithm. One advantage of this approach is that it can be applied to images, without needing raw data, to extract quantitative information on target dimensions not available from the inversion. Furthermore, the boundaries can subsequently be used to define disconnects in the inversion in order to estimate an

updated model of the resistivity structure that better predicts the resistivity structure of the cavities.

Synthetic studies show that our approach facilitates the estimation of boundaries from smooth resistivity images and improves the reconstruction of the geometry of buried archaeological targets, with high accuracy (< 15% error) in most synthetic cases examined. However, the method will generate boundaries within images wherever the resistivity changes significantly, making it somewhat subjective to pick a boundary assumed to relate to an anomaly in the image associated with a cavity. The selection of the boundary associated with an anomaly of a buried tomb is based upon the main criterion that the selected boundary exists in the same location as the anomaly. Most often, as in the scenarios presented here (including the field site), the boundary is obvious.

Even when the watershed method cannot accurately reproduce the target dimensions, we find that it may still improve the interpretation of the subsurface model structure from a smooth inversion. For example, based on the synthetic studies, the single cavity and the two closely spaced cavity inversion results look similar and both would likely be interpreted as a single buried cavity model (compare inversion results presented in Figure 2.2b and 2.5b). However, the watershed identifies boundaries in the closely spaced cavity image that are not present when it is applied to the single cavity model (compare Figure 2.2c and e with Figure 2.5c and e). Although the dimensions of the two cavities are not well predicted, the presence of two features (rather than just one, as might be inferred

from the resistivity image) is predicted. Moreover, by using the located boundaries as a constraint in a second inversion step (using the smooth model as the starting model), the reconstruction of the geometries of these closely spaced cavities significantly improved. The disconnect inversion, based on these boundaries, also improves the estimation of the true resistivity of the targets, although the true resistivity remains poorly resolved. This is an inherent limitation of using 2D imaging over 3D targets with small dimensions.

We have demonstrated the application of our methodology to field datasets collected over archaeological sites where cavities/tombs are suspected. Results from these field studies suggest that the cavity outline can be predicted even with the additional model complexity caused by a highly resistive, thin overburden as often found at these sites. In fact, the watershed algorithm also appears to predict the overburden thickness based on comparison with a strong reflector (assumed to represent a sharp transition in moisture content) from GPR data collected at the site.

Electrical imaging of buried archaeological targets can potentially be improved when acquiring and inverting three dimensional (3D) datasets using a 3D inversion code, since cavities are 3D structures and the 2D inversion approach is based on the assumption that the buried features are two dimensional (e.g., Negri et al., 2008). Our approach could equally be applied to 3D datasets as well, whereby the watershed method could be used to extract boundaries of different anomalies from 3D resistivity vertical or horizontal slices of the model domain. Such boundaries could also be used as *a priori* information in a final inversion step to better reconstruct the 3D resistivities of those targets.

Chapter 3: Improving Reconstruction of Discrete Resistivity Targets Using Coupled Artificial Neural Networks and Watershed algorithms[1]

Abstract

Estimating the dimensions of discrete targets within resistivity models produced as a result of applying smoothness constraints in most inversion algorithms is difficult, especially when targets are closely spaced. Here we couple an image processing technique with a trained Artificial Neural Network (ANN) model to arrive at predictions of the geometry and resistivity of discrete targets from an initial smoothness constraint resistivity model. These predictions are compared with those obtained from applying the watershed algorithm alone, the L1 norm and when a smoothing disconnect is defined using the image processing and data subsequently re-inverted to arrive at a revised model estimate. Synthetic studies were first conducted on a single cavity model, a model for two widely spaced cavities (spacing >> unit electrode spacing), a model for two closely spaced cavities (spacing < unit electrode spacing) and a model for three closely spaced cavities (spacing < unit electrode spacing). In all model scenarios, the average Root Mean Square (RMS) model error for any dimension is below 1 whilst the average combined rms model error when including target resistivity is 35 for the single cavity, 30 for widely spaced targets, and 75 for the closely spaced targets. Despite the higher errors in the closely spaced cavity models, application of the algorithm confirms the presence of

[1]This chapter has been submitted as: Elwaseif, M., and Slater, L., Improving Reconstruction of Discrete Resistivity Targets Using Coupled Artificial Neural Networks and Watershed Algorithms. Submitted to Near Surface Geophysics Journal (submitted on March 09, 2011 and revisions were requested on Jan 23, 2012)

multiple features, which is not ascertainable from the smooth inversion, or even when using the disconnect constraint. The ANN derived model significantly reduces the root-mean-square (RMS) misfit between synthetic and inverted models. We demonstrate the approach using field measurements collected over a precisely known void and also apply the method to smooth resistivity images obtained from measurements collect over the archaeological site at Qurnet Murai, Luxor City, Egypt.

3.1. Introduction

The smoothness regularization is conceptually appropriate when the objective is to predict changes in resistivity due to variations in moisture and/or salinity across space and time. However, when the objective is to predict targets that are characterized by sharp resistivity contrasts (e.g., sinkholes, tunnels, voids), the smoothness constraint is often conceptually inappropriate as our prior expectation is that such targets represent a sharp change in resistivity across some unknown boundary location. In addition, it is difficult to assess the true resistivity and quantify the dimensions (defined here as width, height and depth of burial) of these targets from smooth resistivity models (Nguyen et al., 2005). Two-dimensional (2D) surveys and 2D inversion are still most often used to image inherently three-dimensional (3D) targets such as cavities (e.g., El-Qady et al., 2005), since fully 3D surveys are often time consuming and cost-prohibitive. Although 3D current flow is usually modeled, the 2D inversion assumes that there are no changes in the subsurface resistivity in the direction perpendicular to the survey line, which may lead to significant artifacts in the resulting model for 3D targets.

Several studies have been conducted to improve the reconstruction of targets characterized by sharp boundaries (Kaipio et al., 1999; Slater and Binley (2006); Hordt et al., (2007); Blaschek et al. (2008)). Slater and Binley (2006) describe a disconnect inversion whereby a 'disconnect' in the model domain is defined along the boundary of an object. However, the approach requires that the boundary of the object to be known a *priori*. Hordt et al. (2007) and Blaschek et al. (2008)) describe a complex resistivity inversion that incorporates a regularization parameter that attempts to estimate sharp boundaries based on minimum gradient support (Portniaguine and Zhdanov, 1999) without *a priori* information while still allowing for smooth model structure within the target and away from it. However, since different values of that regularization parameter will lead to different models, these studies still require additional constraints on expected subsurface geology to achieve a reliable model.

Elwaseif and Slater (2010) describe processing procedures for the reconstruction of geometries and resistivities of buried targets characterized by sharp boundaries without the need for incorporation of subsurface *priori* information. Their approach combines (1) an initial 2D inversion using the standard smoothness constraint and a homogeneous starting model (as typically most often done in practice), (2) an image processing technique known as the watershed algorithm to subsequently predict target dimensions (width and height) and depth from the smooth image, and (3) a second inversion step incorporating a disconnect in the regularization based on the output of the watershed algorithm. Although this approach resulted in an improved estimate of the geometries of

individual targets, it was not very effective at predicting the resistivity of the targets and resolving closely spaced targets.

Here, we describe three processing procedures for improving the reconstruction of discrete targets characterized by sharp resistivity contrasts. We focus on synthetic studies of discrete targets with dimensions typical of cavities found at archaeological sites in Egypt. We emphasize that, in such archaeological studies, recovering the geometry and resistivity of those targets is needed to fulfill the objectives of a non-invasive archaeological survey. The resistivity of these targets provides information on the material filling the cavities, whereas the geometry of these targets is important for performing a successful excavation operation.

We explore an approach whereby the secondary disconnect inversion step used by Elwaseif and Slater (2010) is replaced by a trained Artificial Neural Network (ANN) method and compare the results of the two approaches (Figure 3.1). We apply the approach to the synthetic models described in Elwaseif and Slater (2010) for consistency and to facilitate comparison with results reported in their study involving a final model improvement step based on a disconnect inversion. Synthetic studies demonstrate that the ANN approach is more effective than either the smoothness constraint inversion (using L1 norm) or the disconnect inversion for resolving the geometry and resistivity of both widely and closely spaced targets. We also demonstrate the approach on field data collected over a bridge in New Jersey (NJ) where the problem is the detection of a void

of known dimensions underneath the bridge. Finally, we apply the approach on datasets collected at an archaeological site in Egypt where a cavity is suspected.

3.2. Methodology

3.2.1. Inversion with Smoothness Constraints

The objective of regularized resistivity inversion is to find a model that contains a resistivity structure consistent with expectations regarding the likely distribution of resistivity within the subsurface, whilst providing a set of theoretical measurements that fit the measured data to some pre-described acceptable level (e.g., Loke et al., 2003; Gunther et al., 2006). The smoothness constraint inversion is utilized to produce smooth resistivity images in the absence of *a priori* information about the subsurface structures. This regularization constraint is conceptually inappropriate, when the objective is to predict targets that are characterized by sharp resistivity contrasts (e.g., sinkholes, tunnels, voids), as our priori expectation is that such targets represent a sharp change in resistivity across some unknown boundary location. In addition to that, it is difficult to assess the true resistivity and quantify the geometries of the targets from smooth resistivity models.

Smoothness regularization is typically employed with one of two minimization schemes commonly referred to as the L2 norm and the L1 norm (Ellis and Oldenburg, 1994). The L2 norm minimize the squares of the differences between the measured and modeled transfer resistances and/or differences between the estimated model and expected model

structure, and it tends to emphasize models with smoother variations of resistivity. The L1 norm minimizes the absolute differences between measured and modeled resistivity values (and/or differences between the estimated model and expected model structure), and it tends to emphasize models with sharper boundaries between regions of different resistivity, although resistivity values vary less within each region (Loke et al., 2003). The L1 norm is therefore conceptually more appropriate for imaging cavities/tunnels than the L2 norm, since cavities typically present sharp resistivity contrasts within the host medium at distinct boundaries. However, the data noise is more likely to be propagated into the model space using the L1 norm (Hordt et al., 2007).

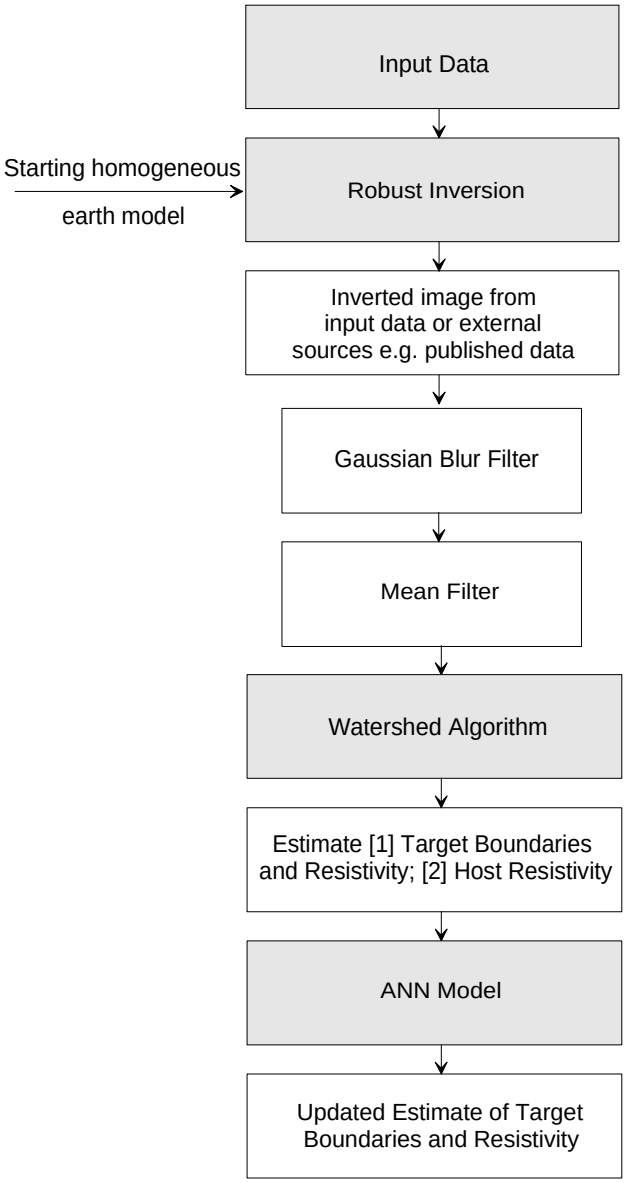

Figure 3.1: Flow chart showing the processing steps used in this study.

3.2.2. Watershed by Simulated Immersion

The watershed by simulated immersion is a technique for segmenting a given image into regions with distinctive boundaries based on mathematical properties of the image parameter space (Roueff et al., 2004; Barraud, 2006). The watershed method could be applied on the output model parameters from any resistivity code that employs the

smoothness constraint in the regularization (Elwaseif and Slater, 2010). Following Elwaseif and Slater (2010), we apply the method to predict the edges of the resistivity anomaly manifest in conventional resistivity inversion models as smooth boundaries. The predicted boundaries are assumed to be consistent with the edges of some unknown resistivity model characterized by sharp boundaries for which we have a smooth image. We apply a sequence of pre-processing steps to increase the contrast between different pixels, reduce noise, and enhance the boundary between different features within the images. The order of these processing steps is described in Figure 3.1. The result of the initial smoothness constraint inversion is plotted as a grayscale image to facilitate image processing. Gaussian blur and mean filters are then applied to preserve feature boundaries whilst reducing noise in the image by replacing each pixel with its neighborhood means (Nixon and Aguado, 2002). The watershed algorithm is then applied to the filtered image. We refer to Elwaseif and Slater (2010) for further details of this approach.

3.2.3. Disconnect Inversion Approach

The smoothness constraint inversion is appropriate for predicting targets that are characterized by gradational, rather than sharp, resistivity contrasts. Several studies have been conducted to improve the reconstruction of targets characterized by sharp boundaries (e.g., Slater and Binley, 2006; Hordt et al., 2007; Blaschek et al., 2008). For example, Slater and Binley (2006) describe a modification of the smoothness constraint to accommodate sharp boundaries whereby a ‘disconnect’ in the model space is defined along the boundary of an object. They applied the technique to a highly conductive target, a permeable reactive barrier made of zero valent iron, being buried in a relatively less

conductive host medium. The disconnect inversion is implemented by giving small weights within the weighting matrix at the position of the known boundary and the regularization matrix is then updated, which results in inverted models with sharp gradients at the locations of the known boundary (e.g., Loke and Lane, 2002; Bouchedda et al., 2012). However, this method requires that the boundary of the target be known a *priori*, and the inversion then solves for a smoothly varying model structure across the host medium and within the disconnected target. Elwaseif and Slater (2010) suggested an approach based on applying the watershed algorithm to a smooth resistivity image in order to define the likely boundary of a target, which subsequently was used as a priori information to define a disconnect in the regularization.

3.2.4. Artificial Neural Networks (ANN)

An Artificial Neural Network (ANN) is based on a parallel computational system that attempts to simulate the interconnected system of neurons in the human brain (Smith, 1993). The method has been previously used to process geophysical data (e.g., Raiche, 1991; Zhang and Poulton, 2001; Winkler and Seiberl, 2003; Park et al., 2010). An ANN consists of an interconnected group of artificial 'neurons' that learn through trial and error. Figure 3.2 shows the learning steps of the ANN used in this study. The ANN consists of an input layer, which has a number of neurons equal to the number of input parameters, and an output layer

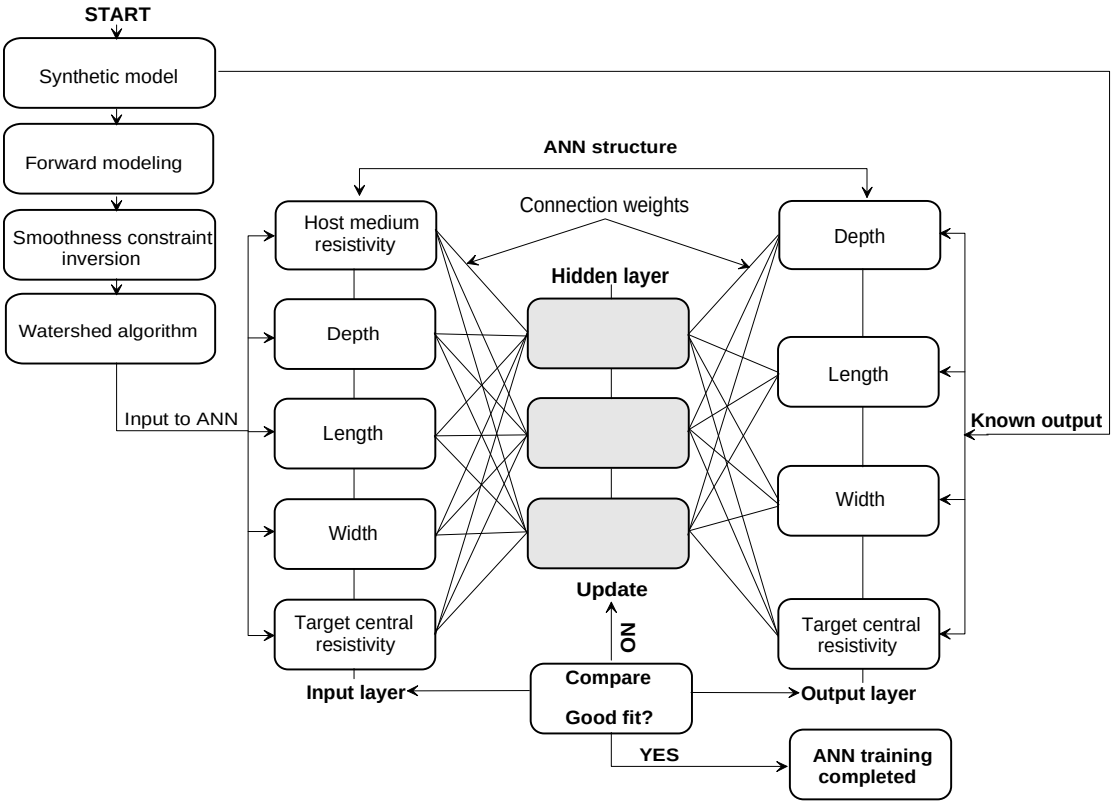

Figure 3.2: Artificial Neural Networks training steps. The input layer is compared with the output layer and connection weights are updated via the hidden layer until a good fit between both is achieved.

which consists of neurons forming the output parameters. In our case, the input parameters are the target dimensions predicted from applying the watershed on the initial smoothness constraint inversion, the average host medium resistivity surrounding each resistivity anomaly and the central resistivity of the target. Note that these two input resistivities are determined from the initial smoothness constraint inversion step (Figure 3.1). Furthermore, the ANN only takes the parameters of individual target anomalies as an input. That said, in case of multiple targets, the watershed algorithm predicts the geometry of those targets and we feed each target geometry as input to the ANN. The output parameters are the revised dimensions and resistivity of buried targets based on

the trained ANN. Due to the highly non-uniform host resistivity at our field sites, an estimate of the host resistivity is not output for the field datasets. The number of layers forming the ANN (i.e. complexity) can be increased by including more hidden layers between the input and output layers. All the layers are connected via connection weights that are established during a training phase, and the value of each output parameter depends on the combined values of all the input parameters.

During the learning (or training) stage, a large number of known models are input into the neural network. In this research, we created data for approximately 250 model scenarios for single and multiple closely and widely spaced cavity targets having resistivity and geometry values cover our expected possible range of targets typically found at archaeological sites in Egypt. The modeled cavities have different dimensions (length and width) that range from 1 m^2 up to 20 m^2, and were buried at different depths up to 3 m. In addition, the cavities were assigned resistivity values ranges from 400 Ohm m up to 100k Ohm m. Furthermore, we assumed a homogeneous host medium resistivity values that ranges from 50 Ohm m up to 500 Ohm m. Finally, the resultant synthetic data were contaminated with different Gaussian noise levels of 2, 3, 5, 6 and 10%.

The resulting output from the hidden layers is compared with the desired output (i.e. the known model parameters) and the hidden layers are used to adjust the connection weights until a good approximation between the input and the desired output is achieved (Figure 3.2). There are different approaches to minimize the error between the input and the desired output (e.g., Simpson, 1990; Stanley and Miikkulainen, 2002). In the back-

propagation method used in this study, the error at the output layer is quantified and propagated backwards to the hidden layers and the connection weights attached to the hidden layers are updated to minimize that error (Rumelhart, 1986). After the network is correctly trained (i.e., the lowest RMS error between known input and desired output is achieved), the ANN can predict the output for new inputs quickly and accurately, assuming it is within the range of different parameters included in the trained models (Smith 1993). Here, we use the ANN to predict the dimensions and resistivity of buried targets characterized by sharp boundaries relative to the host medium.

Conventional smoothness regularization constraints in resistivity inversion result in a highly underdetermined problem, where the number of model parameters much exceeds the number of measurements. In contrast, the input of the ANN consists of five model parameters (one model parameter for the host mediumand four model parameters for each resistive target within the model space (depth, width, length and resistivity value)), whereas the output consists of four parameters (depth, width, length and resistivity value for each resistive target) (Fig. 3.3). Our ANN recovery approach is thus an overdetermined problem. A disadvantage of an over-determined problem is that it can be difficult to minimize the data misfit due to the limited number of model parameters, which cannot fully describe the whole model space. We show here that the ANN approach results in a much reduced model misfit for the case of such discrete targets.

3.3. Synthetic models

Here we calculate synthetic apparent resistivity pseudosections for the same synthetic

models as described in Elwaseif and Slater (2010), and subsequently invert these data using Res2dInv (Loke and Barker, 1996) to allow for direct comparison between the ANN approach and the L1 norm and disconnect inversion reported previously. The

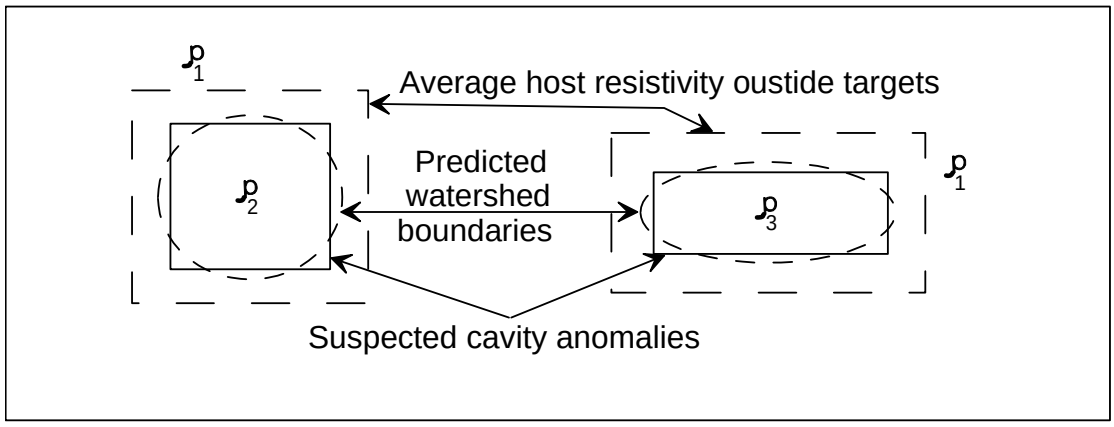

Figure 3.3: sketch showing the input parameters for two cavities with different shapes buried in non-uniform host medium.

synthetic models considered are , [i] a single cavity, [ii] two widely spaced cavities (separation > unit electrode spacing), [iii] two closely spaced cavities (separation < unit electrode spacing), and [iv] three closely spaced cavities (separation < unit electrode spacing). The 2D forward modeling datasets were generated using a 3D forward modeling code, Res3dMod (Loke and Barker, 1996), to simulate real data collected in the field over cavity features, by accounting for both 3D current flow and a 3D resistivity structure (Elwaseif and Slater, 2010). The cavities were assigned a resistivity of either 500, 1000 or 100k Ohm m, whereas the host medium was assigned a resistivity of 100 Ohm m in all scenarios. These were considered reasonable representative values based on known results from cavities at archaeological sites in Egpyt (e.g., El-Qady et al., 2005) (Figure 2.10). Following Elwaseif and Slater (2010), thirty two electrodes were used to

create the synthetic data and a dipole-dipole array was chosen due to its relatively high sensitivity to horizontal changes in resistivity (e.g., Dahlin and Zhou, 2004). The electrode spacing was 1 m and ten depth levels (inter dipole spacings) were utilized, providing 390 measurements and a maximum investigation depth of about 4.5 m based on theoretical relations between electrode spacing/geometry and investigation depth for a homogeneous earth medium (e.g., Loke, 2004). All synthetic datasets were contaminated with 2% uniformly distruted noise, representative of noise levels expected in typical field data such that

$$data_{noise} = data_{noise\text{-}free} + 0.02*R \qquad (3.1)$$

where R is a random variable with mean = 0 and variance = 1.

We created the same three model scenarios as described in Elwaseif and Slater (2010), in addition to a fourth model that consists of three closely spaced cavities filled with sediments and air. In the first scenario, a single cavity was buried at 1.2 m depth, having a width, a breadth and a length of 4 m and resistivity of 1000 Ohm m (Figure 3.4a). The second scenario involved two cavities having resistivity values of 500 and 1000 Ohm m. Two cases of this two cavity model were considered (a) a widely-spaced cavities model involving cavities with widths, breadths and lengths of 4 m and spaced 4 m apart (edge to edge) i.e. greater than unit electrode spacing (Figure 3.4b); (b) a closely-spaced cavities model involving cavities with widths, breadths and lengths of 2.8, 2.8 and 2.7 m and spaced 0.6 m apart (edge to edge) i.e. less than the unit electrode spacing (Figure 3.4c). In addition, we created a three closely- spaced cavities model having resistivity values of 500, 1000 and 100k Ohm m (air filled), and having widths, breadths and lengths of 2.8,

2.8, and 2.7 m and spaced 0.6 m apart (Figure 3.4d).

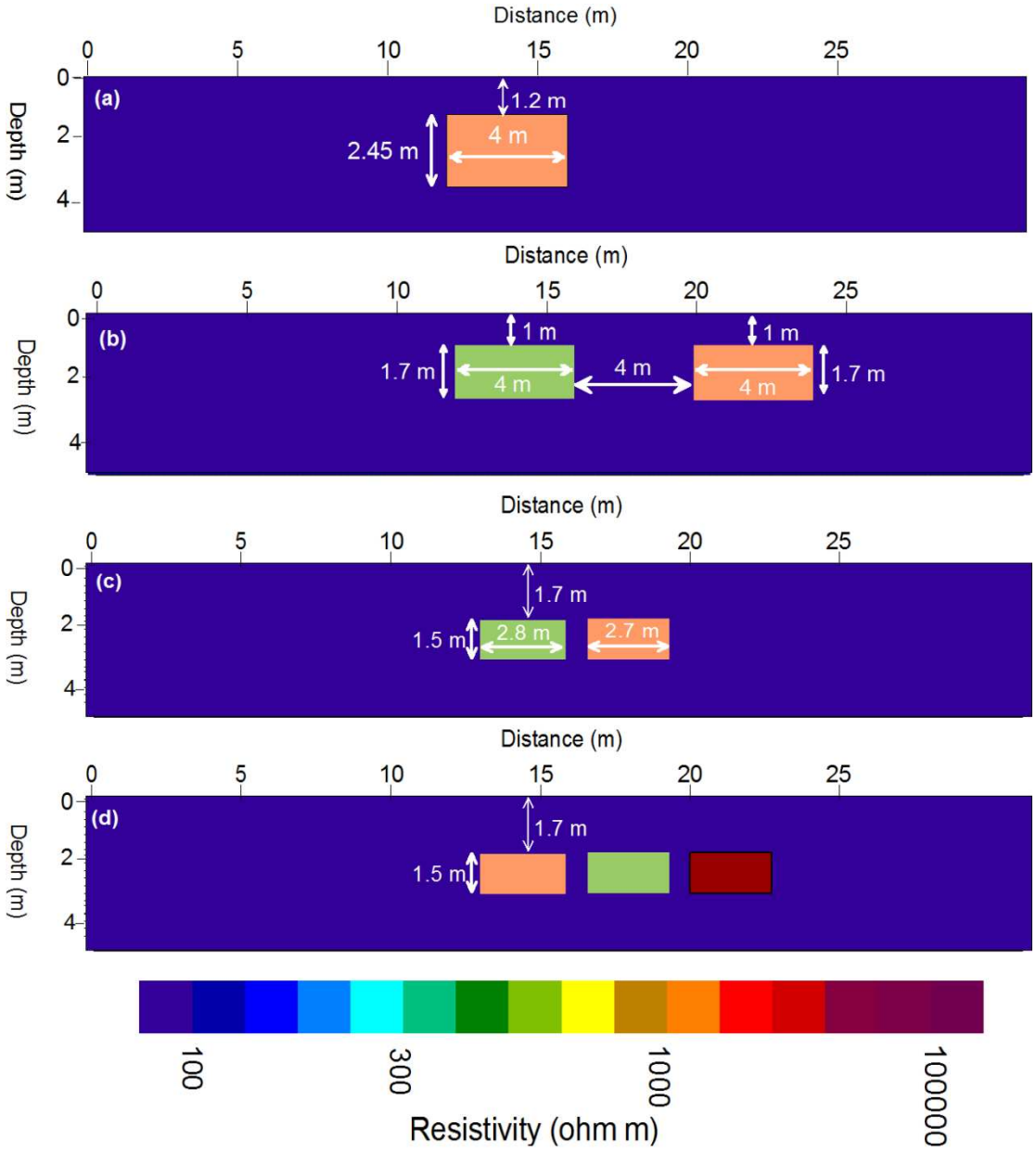

Figure 3.4: Synthetic 3D model scenarios. (a) single cavity (b) widely spaced cavities (c) two closely spaced cavities (d) three closely spaced cavities. The breadth of the single cavity and widely spaced cavities is 4 m, whereas the breadth of the closely spaced cavities is 2.8 m.

3.4. L1 norm Inversion

As outlined earlier, we chose to perform a 2D inversion of the datasets generated using 3D forward modeling as this best represents the situation for datasets typically obtained from the field i.e. 2D resistivity profiles over cavities will record measurements resulting from 3D current flow through 3D structures but will be interpreted with codes that assume the structures are two dimensional.

We chose to invert all the data using the L1 norm approach, since it is more appropriate for imaging cavities/tunnels than the L2 norm, since cavities exhibit sharp contrasts within the host medium at distinct boundaries. In all cases, a homogeneous medium was used as the starting model, and five iterations were performed. The results of applying the inversion on the single, widely spaced, and closely spaced cavity models are shown in Figures 3.5a, 3.6a, 3.7a and 3.8a, respectively. White outlines show the true cavity dimensions. The RMS model errors for each inversion are estimated using the following formula and included in the figures:

$$RMS = \sqrt{mean((m_{real} - m_{est})^2)} \quad (3.2)$$

where m_{real} is the actual model parameters and m_{est} is the estimated model parameters.

The widely spaced cavities are clearly associated with individual anomalies in the resistivity images (Fig. 3.6a). However, the closely spaced cavities appear as a single anomaly (Fig. 3.7a and 3.8a), instead of separate features, due to the small spacing between cavities (here less than the unit electrode spacing) (Elwaseif and Slater, 2010).

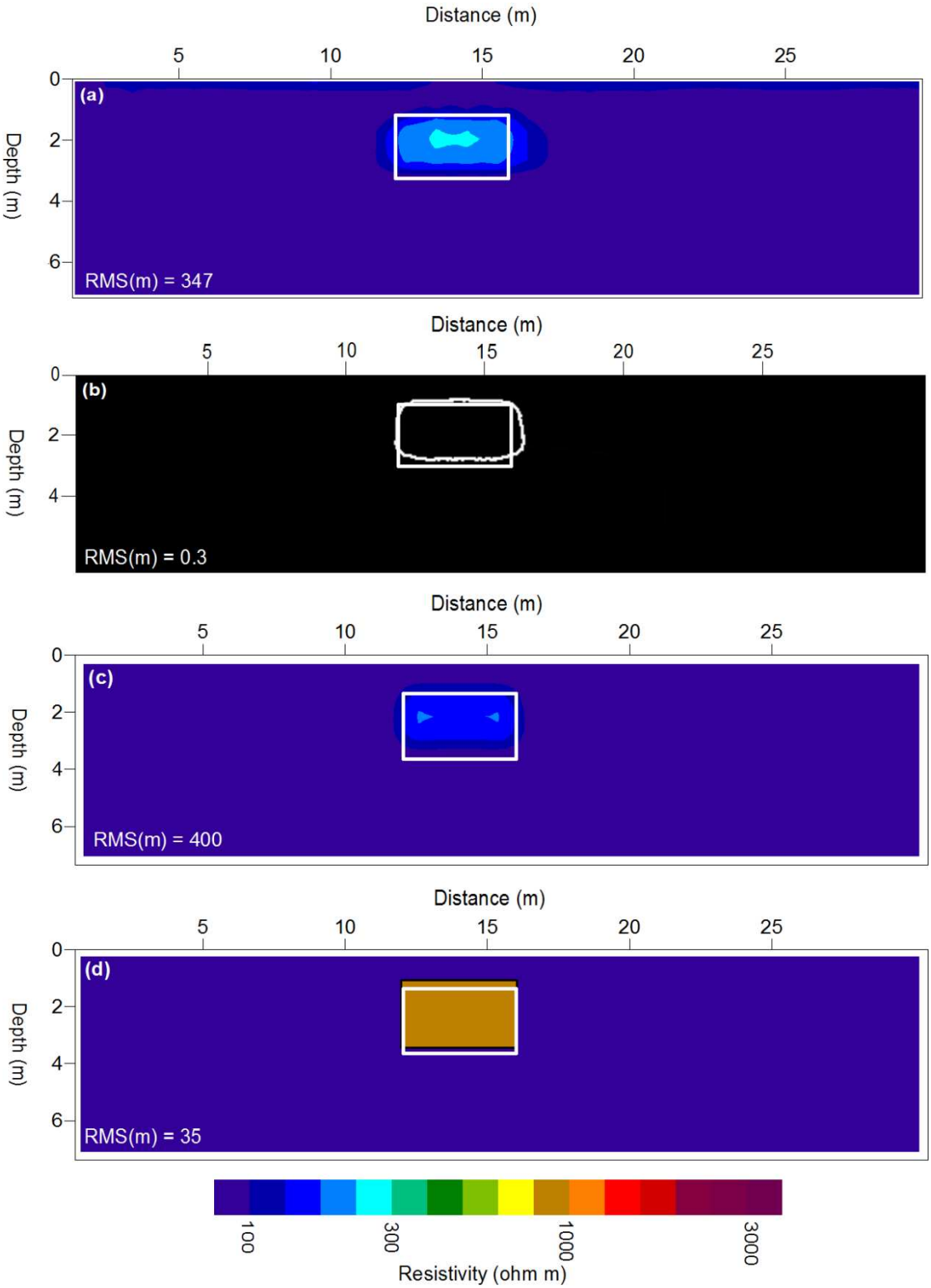

Figure 3.5: Results of the single cavity model (a) L1 norm section (b) detected boundaries based on a (c) disconnect inversion model (d) ANN model (model misfit are shown in sections and boxes denote true cavity outline).

The watershed algorithm was subsequently applied on these inverted resistivity images to predict likely boundaries of the target anomalies. The results of applying the watershed algorithm on the single, widely spaced, and closely spaced cavity models are shown in Figures 3.5b, 3.6b, 3.7b and 3.8b, respectively. The method predicts a boundary in the resistivity anomaly associated with the closely spaced cavities, despite that evidence for this boundary cannot be visually inferred from the inverted resistivity model. To better understand the influence of data noise on the watershed algorithm results, the data of the closely spaced cavity model was contaminated with either 2% or 10% noise and each data was inverted assuming 2%, 5% and 10% data noise. Figure 3.9 shows that the performance of the watershed algorithms is dependent on the accuracy of the inversion process.

The optimum result was obtained when assuming an accurate noise levels. However, in all cases, the watershed algorithm predicted a boundary between the two cavity anomaly. As the assumed data noise overestimates the actual noise level (Figure 3.9a), the accuracy of watershed prediction gets less accurate. Similarly, as the assumed data noise underestimates the actual noise, the accuracy of watershed prediction gets worse (Figure 3.9b). However, the accuracy of watershed prediction in case of overestimating the noise level is better than when underestimating it probably because the data itself is contaminated with less data noise. The watershed predicted target boundaries are used to define disconnects in the initial smoothness constraint inversion in order to estimate a model that better predicts the resistivity structure of the cavities as described in Elwaseif and Slater (2010). The watershed predicted target boundaries and the central resistivity

value of the resistivity anomalies were used as inputs to the ANN (Figure 3.1).

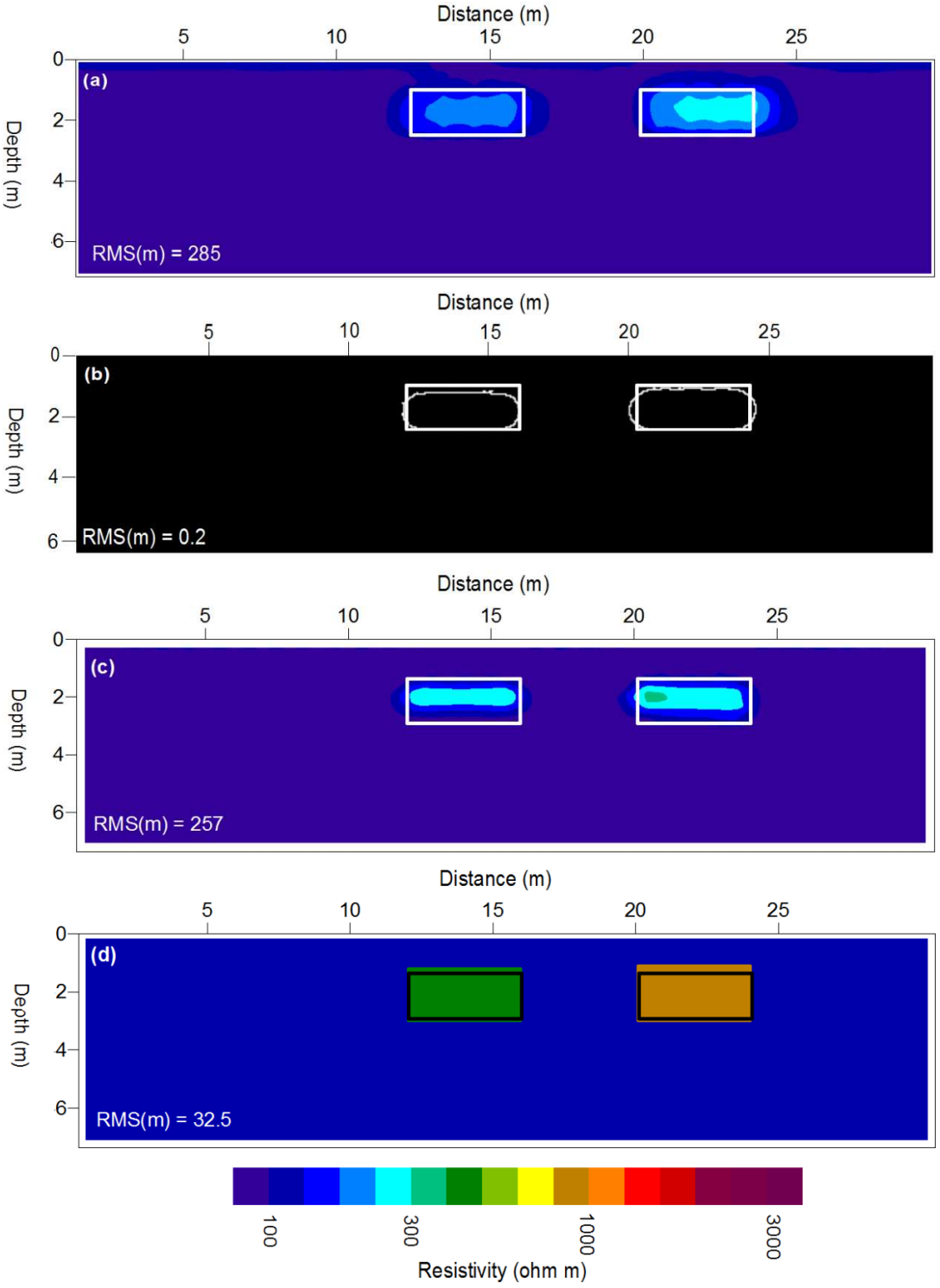

Figure 3.6: Results of the widely spaced cavities model (a) L1 norm section (b) detected boundaries based on a (c) disconnect inversion model (d) ANN model (model misfits are shown in sections and boxes denote true cavity outline).

3.5. Re-inverting datasets using the ANN

The ANN model was trained using 251 known synthetic cavity models, each having different geometries, resistivity values and host medium resistivity. All cavity targets were modeled as quadrilaterial objects in the training, being representative of target cavities often found at archaeological sites in Egypt (e.g., El-Qady et al., 2005; Miller et al., 2005) (Figure 3.3). The objective of the training was to establish a relationship between the inputs and outputs of the ANN, by minimizing the back-propagation objective function (Figure 3.2).

Figures 3.5c and 3.5d shows the disconnect inversion and ANN section for the single cavity model. The disconnect inversion results in an improved recovery of target geometry relative to that obtained from initial smoothness constraint inversion. The detected cavity boundary from the ANN model has an average model error of 0.1, while the average model error for the watershed predicted geometry is 0.3 In addition, the ANN shows improved recovery for the single cavity resistivity relative to that obtained from the initial smoothness constraint and disconnect inversions. The average model error when including the resistivity of the single cavity for the ANN is 35 relative to 375 in the L1 norm image and 400 in the disconnect inversion image.

Figures 3.6c and 3.6d shows the disconnect inversion and ANN section for the widely spaced cavities model. The disconnect inversion again results in an improved recovery of both geometries and resistivity of both cavities relative to that obtained from the initial smoothness constraint inversion. The ANN, however, has more success in predicting the

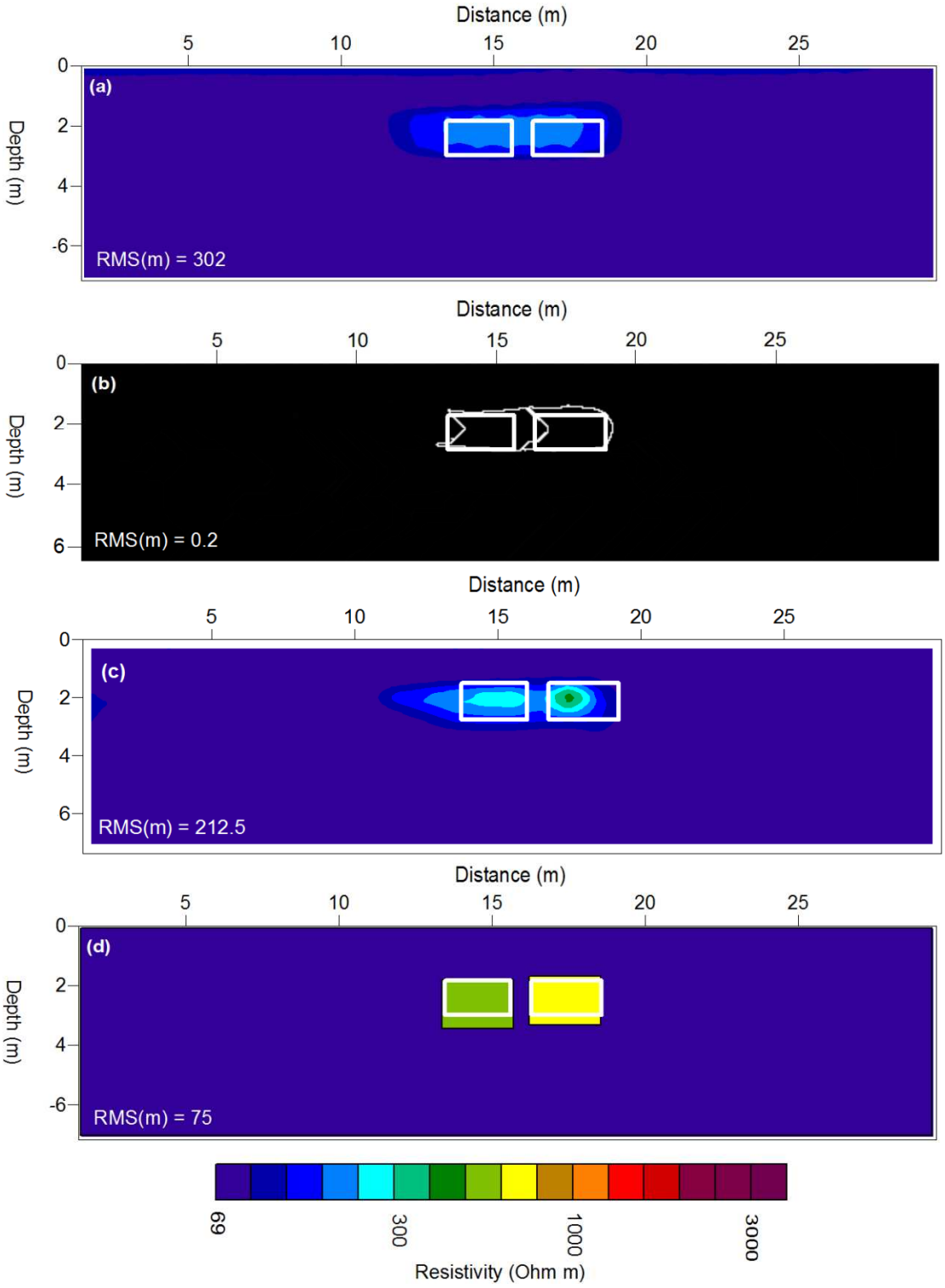

Figure 3.7: Results of the two closely spaced cavities model (a) L1 norm section (b) detected boundaries based on a (c) disconnect inversion model (d) ANN model (model misfits are shown in sections and boxes denote true cavity outline).

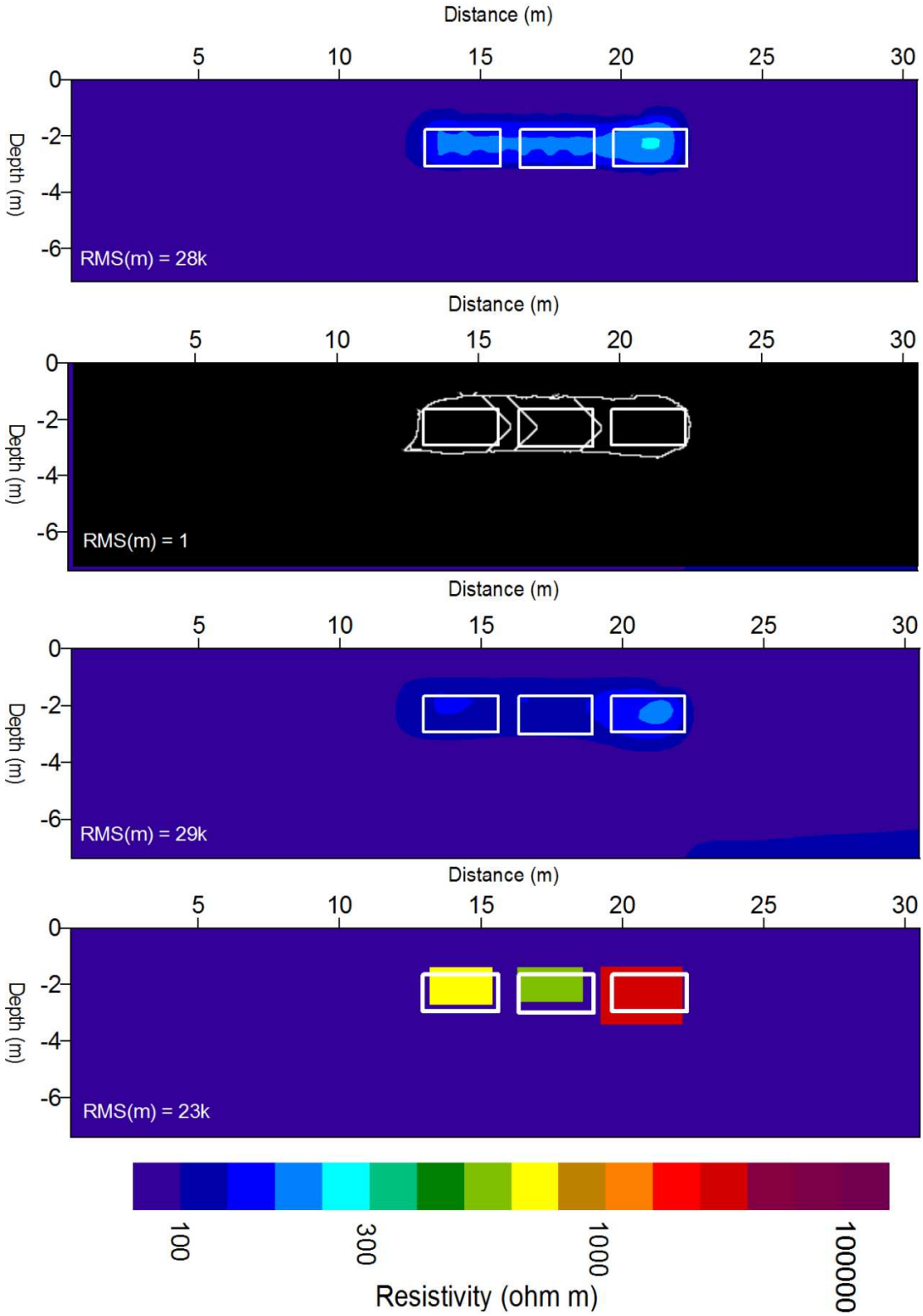

Figure 3.8: Results of the three closely spaced cavities model (a) L1 norm section (b) detected boundaries based on a (c) disconnect inversion model (d) ANN model (model misfits are shown in sections and boxes denote true cavity outline).

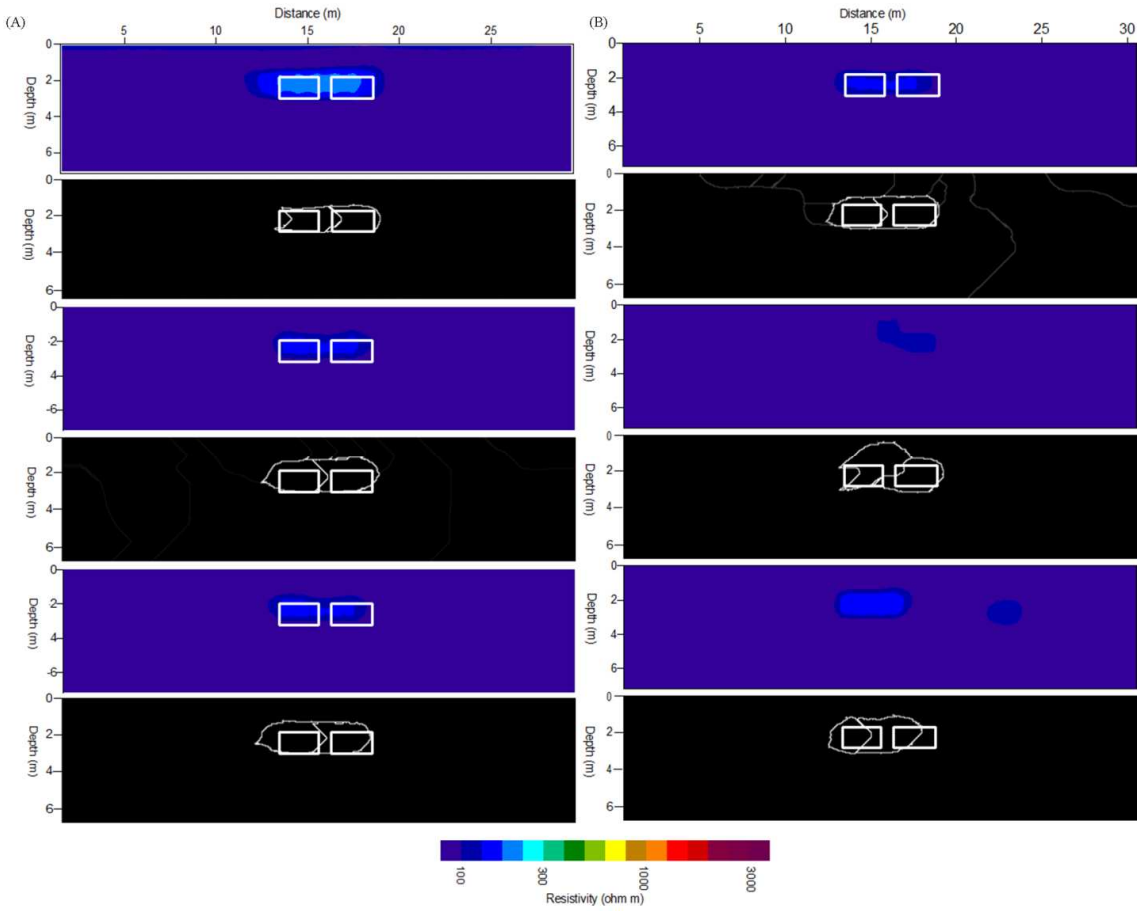

Figure 3.9: Influence of data noise on Watershed algorithm results (A) overestimating the actual data noise (2%) during inversion (assumed noise levels from top are 2%, 5% and 10%) (B) underestimating the real data noise (10%) during inversion (assumed noise levels from top are 10%, 2% and 5%) (boxes denote true cavity outline).

geometry and resistivity of each cavity than the watershed predicted geometry and disconnect image. The average model error when estimating cavities dimensions in case of ANN is 015relative to 0.2 in the weatershed image. The average model error when including the resistivity of each cavity for the ANN is 32.5 relative to 262.5 in the L1 norm image and 257 in the disconnect inversion image. Figures 3.7c and 3.7d shows the disconnect inversion and ANN section for the closely spaced cavities model. Unlike in the L1 norm and disconnect inversion approach (Elwaseif and Slater, 2010), the ANN

section clearly depicts the presence of two resistive features basically due to the initial success of the watershed algorithm in identifying them , with the cavity on the right predicted as the more resistive. The reconstruction of geometries and resistivity values of both cavities are improved compared with the results obtained from the L1 norm or disconnect inversion. The detected cavity boundaries from the ANN model has an average model error of 0.15 relative to 0.3 in case of watershed predicted geometry, whilst the model error when including the resistivity of each cavity for ANN is 75 relative to 302 in the L1 norm image and 212.5 in the disconnect inversion. Figures 3.8c and 3.8d shows the disconnect inversion and ANN section for the three closely spaced cavities model. As expected, the ANN section clearly depicts the presence of three resistive features, with the cavity on the right predicted as air filled. The reconstruction of geometries and resistivity values of the cavities are improved compared with the results obtained from watershed algorithm, L1 norm or disconnect inversion. The detected cavity boundaries from the ANN model has an average model error of 0.3 relative to 0.6 in case of watershed image, whilst the model error when including the resistivity of each cavity for ANN is 23k relative to 28k in the L1 norm image and 29k in the disconnect image.

Table 3.1 summarizes the performance of the disconnect inversion and the ANN for the four model scenarios. In general, the RMS error of the ANN model misfit is much less than the model misfit of the watershed algorithm or L1 norm for all model scenarios. In addition the RMS model misfit based on when the target resistivity is included in the model misfit calculation is significantly reduced compared to when it is included.

To test the performance of our ANN model on more noisy data, we applied our approach on the two closely spaced cavity model obtained from inverting data contaminated with 5% and 10% noise. We assumed an accurate data noise levels during the inversion process and we followed the same processing steps as described in other synthetic models. As shown in Figure 3.10, the ANN better recovers the geometry and resistivity values of the two cavities compared with the watershed algorithm, L1 norm model and the disconnect inversion model. In addition, the estimated geometry and resistivity of the two cavities are consistent with the previous results described in Figure 3.7d.

Table 3.1, Comparison between the model misfit results of disconnect inversion and ANN for the known field and synthetic models, where 'D' – depth, 'W'– width, 'H' – height, 'R' – resistivity (Ohm m), and 'L1' – L1 norm.

Resistivity Models	True dimensions (m)				Watershed Algorithm (WA)			L1	ANN				RMS model error			
	D	W	H	R	D	W	H	R	D	W	H	R	Without 'R'		With 'R'	
													WA	ANN	L1	ANN
One cavity	1.2	4.0	2.45	1000	0.8	4.3	2.1	200	1	3.9	2.5	930	0.3	0.1	375	35
Two cavities-widely spaced	1.0	4.0	1.7	500	1.2	4.0	1.5	200	1.1	4	1.9	444	0.2	0.1	150	28
	1.0	4.0	1.7	1000	1	4.3	1.7	250	1	4.1	2	926	0.2	0.2	375	37
Two cavities-closely spaced	1.7	2.8	1.5	500	1.6	3.1	1.4	200	1.8	2.9	1.7	562	0.2	0.1	125	31
	1.7	2.7	1.5	1000	1.4	2.9	1.6	200	1.6	2.8	1.8	759	0.2	0.2	300	120
Three cavities-closely spaced	1.7	2.7	1.5	500	1.1	2.8	2	200	1.4	2.6	1.3	501	0.5	0.2	150	0.5
	1.7	2.7	1.5	1000	1.1	3	2.1	200	1.4	2.5	1.4	630	0.5	0.2	400	185
	1.7	2.7	1.5	100k	1.1	3.5	2.4	250	1.4	2.9	2.1	17K	0.8	0.4	49k	41k
Field example	0.8	2.9	1.4	-	0.9	1.6	1.2	18k	1.02	2.9	0.98	176k	0.8	0.3	-	-

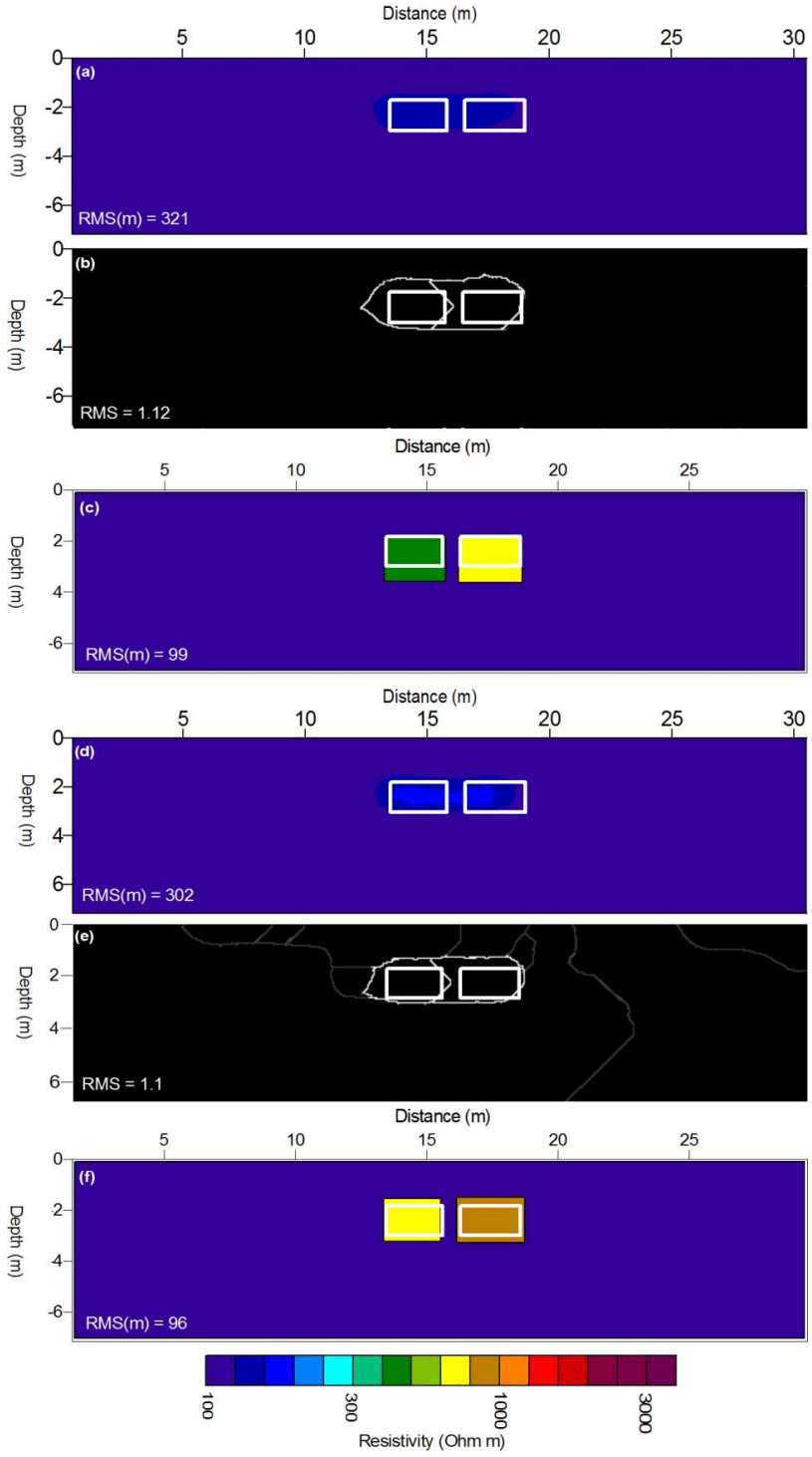

Figure 3.10: Results of the more noisy two closely spaced cavities model (a) L1 norm section obtained from inverting data contaminated with 5% noise (b) detected boundaries based on a (c) ANN model (d) L1 norm section obtained from inverting data contaminated with 10% noise (e) detected boundaries based on d (c) ANN model (model misfits are shown in sections and boxes denote true cavity outline).

3.6. Field studies

3.6a. Application to field data: Locating a known tunnel

In order to illustrate this approach on real datasets, the ANN was first applied on datasets acquired over a known void underneath a bridge. The depth and dimensions of the void underneath the bridge were recorded in the field. The void is filled with air and buried at a depth of 0.8 m, having a width and a length of 2.9 m and 1.4 m (Fig. 3.11a). The survey line was laid out about 1 m from the edge of the tunnel and the tunnel extended sufficiently far in the direction perpendicular to the survey line, that it can essentially be considered a 2D structure appropriate for 2D acquisition and inversion.

A 2D dipole-dipole array with 1 m electrode spacing and 6 depth levels was acquired using a Supersting automatic resistivity system (AGI Instruments, USA), providing 864 measurements, with a modeled maximum investigation depth of about 6 m. The inversion followed the same processing steps as performed on the synthetic datasets. Figure 3.8b shows the inverted resistivity profile using the initial smoothness constraint inversion and a homogeneous starting model. The section displays a wide range of resistivity values. The anomalous zone of high resistivity located between 11 to 13 m on the profile and at a depth of about 1 m coincides with the bridge and is assumed to be the response of the void underneath the bridge. This anomaly is elongated, and is not a good representation of the known geometry of the void. In addition, the void is not represented by a feature with a homogeneous resistivity. The results of applying the watershed by simulated immersion technique on Figure 3.11b is shown in Figure 3.11c. Based on this result, the

void is predicted at 1.1 m depth, with a width and a length of 1.5 m and 1.7 m respectively. The disconnect inversion results is shown in Figure 3.11d. The anomalous zone belonging to the void has sharper boundaries, but is still elongated and its resistivity is significantly less than that expected from an air-filled void. The results from the initial smoothness constraint inversion and the watershed algorithms were input in the ANN and the result is shown in Figure 3.11c. The ANN predicts a void with a very high resistivity 176300 Ohm m) and with a geometry that has an RMS model error of 0.3 relative to 0.8 in the watershed image based on the known field geometry (Table 3.1).

3.6b. Application to field data: mapping cavities in Qurnet Murai

We next applied both the disconnect inversion and ANN on datasets acquired from Qurnet Murai, Egypt (Figure 3.12). The site is located on the western bank of Luxor city. Resistivity surveys have been conducted at this site in an effort to locate undiscovered artifacts, primarily tombs. As previously discussed, the geometries of those tombs are expected to have similar dimensions to the synthetic cavities explored in this study (Elwaseif and Slater, 2010). Eight parallel 2D resistivity lines, 32 m long and spaced 5 m apart, were collected at the survey site in May 2006. A dipole-dipole array with 1 m electrode spacing and 6 depth levels was utilized, providing 111 measurements and a maximum investigation depth of about 4 m. Due to time constraints in the field, additional quadripoles used in the synthetic studies were not collected during this experiment. Figure 3.12a shows the inverted resistivity profile from the initial smoothness constraint inversion. The section displays a wide range of resistivity values. The top resistive layer (~ 3000 ohm m) is common in this environment due to very dry

sediments at the surface as a result of extensive evaporation driven by high temperatures (regularly reaching 46° C at this site). Below this surface layer, resistivities are much lower, ranging from 20-300 ohm m, primarily due to increasing moisture content with depth. An anomalous, relatively high resistivity zone (between 1-3.5 m depth) occupies the area between 16 to 20 m along the line and is suspected to relate to a cavity filled with friable soils.

The results of applying the watershed by simulated immersion technique predict that this suspected cavity is located at 1.6 m depth and is 4 m wide (fig 3.12b). The disconnect inversion result is presented in figure 3.12c. The root mean square error between the theoretical and measured data was 9.3 % without using the disconnect boundary in the inversion, compared with 7 % after employing it. Applying the ANN (Fig. 3.12d), the suspected cavity is located at 1.2 m depth, is 5 m wide and is 4 m long. The estimated depth of this cavity, is consistent with the presence of diffraction hyperbolae at a horizontal distance of around 14 m on the profile and at a depth of 1.25 m recorded in a radar profile collected very close to the resistivity line (Elwaseif and Slater, 2010). The predicted cavity dimension is also consistent with previous excavations at field sites in Egypt (e.g., Metwaly et al., 2005).

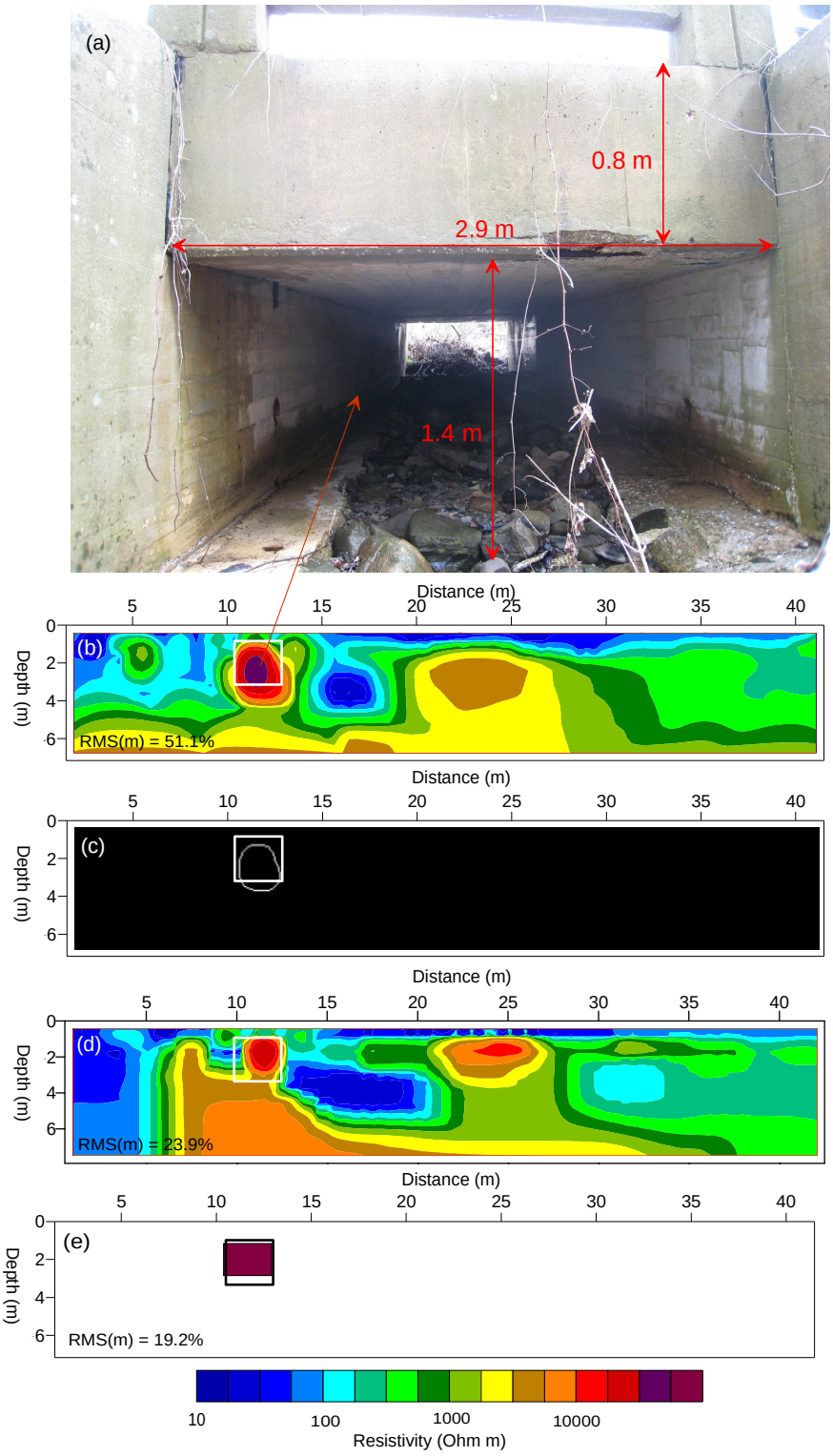

Figure 3.11: Results of the known cavity model (a) Photo of the cavity (b) L1 norm section (c) detected boundaries based on a (d) disconnect inversion model (e) ANN model (model misfits are shown in sections and boxes denote true cavity outline).

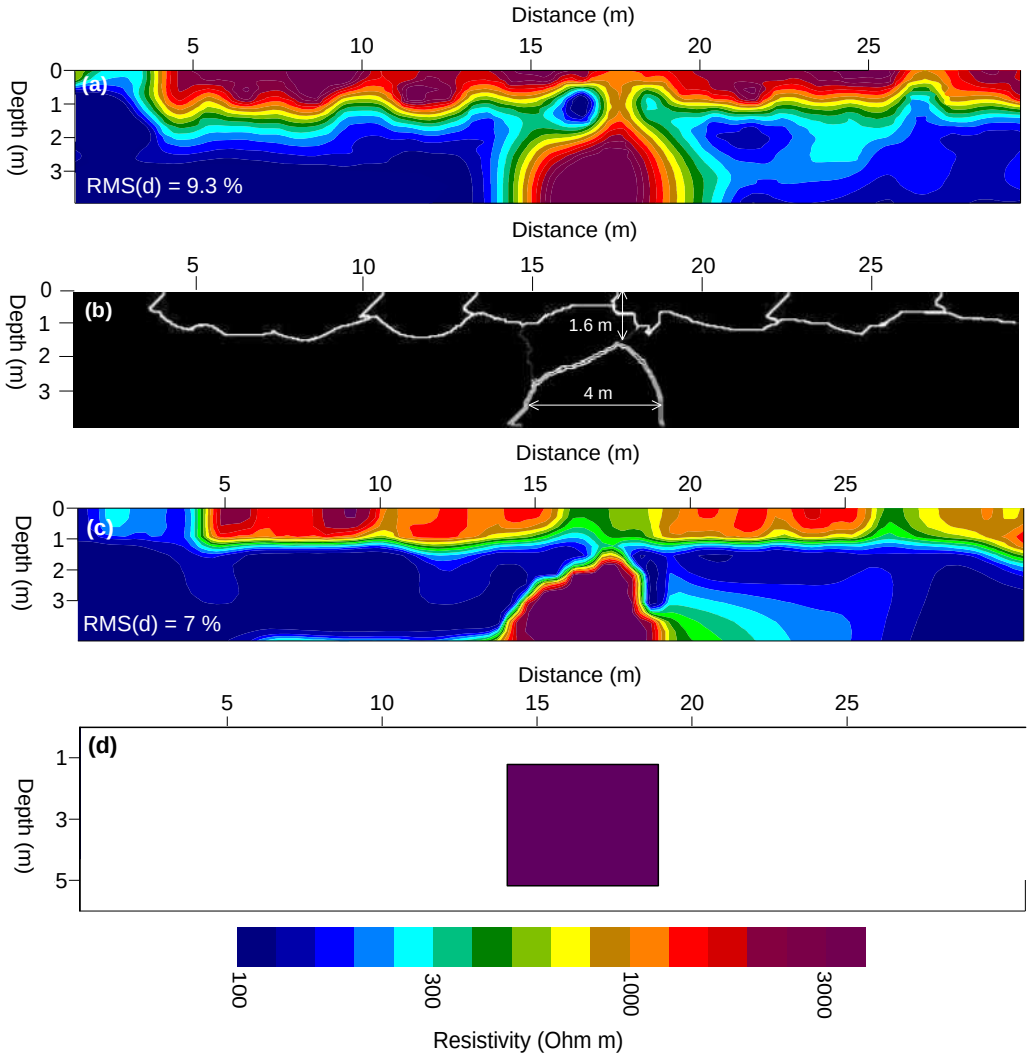

Figure 3.12: Results of the unknown field model (a) L1 norm section (b) detected boundaries based on a (c) disconnect inversion model (d) ANN model.

3.7. Discussion

The commonly applied smoothness constraint inversion is not ideal for imaging buried targets with sharp resistivity edges, since it generates models characterized by a smooth distribution of resistivities over a wide range of values. Using a disconnect boundary in the inversion estimated from the watershed algorithm can improve imaging the geometry of such targets, although target resistivity values are underestimated and closely spaced

targets are not individually resolved (Elwaseif and Slater, 2010). We have shown here that using a trained ANN in place of this disconnect step can improve the reconstruction of dimensions and resistivities of such targets. For example, based on the synthetic studies, the single cavity and the closely spaced cavities models show very similar smooth inversion results and both images would likely be interpreted as evidence of a single buried cavity. Although the watershed identifies boundaries in the closely spaced cavity image, the resistivity and dimensions of the two cavities are not well predicted in the disconnect inversion model. In contrast, as shown in Figure 7d, the ANN significantly improved the reconstruction of the resistivity and geometries of these closely spaced cavities.

We have described a two step approach whereby image processing of an initial smoothness constraint inversion is used to determine a first estimate of likely target location and geometry, from which the ANN is able to optimize. The performance of the ANN depends significantly on the given model scenarios during the training stage. Better performance will be achieved when a large number of model scenarios with different dimensions and resistivity values are input. Here, the ANN was trained on quadrilateral targets due to our *a priori* knowledge that the targets of interest fit this geometry. Thus, unlike the disconnect inversion approach described by Elwaseif and Slater (2010) that does not require any *priori* information, the expected shape of the targets used in the training is the required *a priori* information in this approach. Since the shape of the target is known *priori,* it might be not surprising that the ANN gives better results than the disconnect inversion approach. However, further training on a wider array of target

shapes would reduce the amount of a priori information effectively incorporated within the ANN. That said, the strength of the ANN is that it provides a very effective way to incorporate appropriate a prior information through training when targets have specific shapes as often the case for archaeological features.

Synthetic studies demonstrate that the ANN largely reduces the model misfit relative to that obtained with the initial smoothness constraint and disconnect inversions and generates more realistic representations of discrete targets considered here. Data misfit is compromised, but this is to be expected given that the ANN is trained to predict few model parameters that are only related to target anomalies. The highly over-parameterized smoothness-constrained inversion will always find numerous models from the large number of possible parameter combinations that result in a low data misfit. However, these models usually do not provide a good estimate of target dimensions in the case of discrete targets.

The ANN used here is effective at predicting target location and geometry. In addition, our approach shows more success in reconstructing the geometry and resistivity of targets than the L1 norm, disconnect inversion approach or watershed algorithm. This is clearly shown from the model misfit results presented in table 1. The model misfit for excluding resistivity (i.e. only using target geometries) is less than the model misfit when the target resistivity is included. The estimation of target resistivity and geometry could be improved by increasing the number of models used in training the ANN. However, the limited accuracy in the target resistivity will often not be a major concern in many

archaeological and engineering studies where we are most often interested in target location and geometry.

We have demonstrated the application of our approach to field datasets collected at a site in NJ over a known void and a site in Egypt where cavities are suspected. The approach, particularly the application of the watershed, is somewhat subjective, especially in the case of dealing with noisy data when smooth resistivity images will likely contain image artifacts or additional local resistivity structure beyond that caused by the targets of interest. Without additional information (as was available in the survey over a known tunnel), it would be difficult to identify appropriate boundaries from the watershed algorithm. Such ambiguity could be reduced from the results of other geophysical methods as we describe in our field study at Qurnet Murai. In this field study, the suspected anomaly in the resistivity model that results from the cavity was confirmed using the GPR data.

Our synthetic studies were overly simple in that they assumed a single uniform background resistivity that the ANN was trained to predict. However, as a result of the highly variable resistivity away from targets at real field sites, the ANN approach was adjusted to search only for target resistivity and dimensions. In this case, the ANN was given the average resistivity outside of the predicted watershed target boundaries as input. Based on observations during the training of the ANN the ratio of target to background resistivity has a significant effect on both the dimensions and the centre resistivity of predicted targets. For example, as the ratio of target to background resistivity increases,

the predicted target anomaly will have sharper boundaries but the centre resistivity value of the anomaly will be smaller than the actual value.

Results from the field and the synthetic studies suggest that the ANN approach has potential for reconstructing the geometry and resistivity of discrete targets in field datasets. One interesting advantage of our approach is that it can be applied to images, without needing raw data, to provide estimates of target geometry. The average host medium resistivity and the target central resistivity value can be estimated from the resistivity scale, whereas the target boundaries can be estimated using the watershed algorithms. These estimations can be used as an input to the ANN in order to estimate an updated model of the target resistivity and geometry.

Our approach is subject to some distinct limitations. Firstly, the performance of an ANN will depend on the adequacy of the training effort. In this study, the training of the ANN is based only on synthetic datasets. Ideally, the ANN should be trained on field data where target are known (Park et al., 2010). Unfortunately, such datasets are most often unavailable. Furthermore, the ANN output is ultimately in part conditioned on the original smoothness constraint step on which the watershed algorithm was applied.

3.8. Conclusions

Application of an ANN conditioned on the results of an initial smoothness constraint inversion and subsequent image processing, appears to be a viable approach for determining the location of discrete targets in resistivity datasets. We have shown that the

predicted boundaries and resistivity of the targets using an ANN are significantly improved when compared with results from the initial smoothness constraint, disconnect inversions and watershed algorithm. However, the ANN approach shows more success in predicting the geometries of targets than their resistivity values, which make it an appropriate approach for studies that focus more on recovering the geometry of subsurface targets such as archaeological studies. Using this approach the geometry of multiple targets, even when separated by a distance less than the unit electrode spacing, are fairly well recovered. Our approach was demonstrated on targets that have rectangular shapes, but it can be adjusted to fit any target shape by retraining the ANN on those shapes. The approach appears promising for predicting archaeological artifacts in Egypt where previous excavation confirmed the same shapes described here. In addition to archaeological artifacts, the approach might also be appropriate for predicting the location of engineering structures and voids in karst environments.

Chapter 4: Improved Resistivity Imaging of Targets with Sharp Boundaries Using an Iterative Disconnect Procedure[1]

Abstract

The smoothness constraint inversion is not appropriate for imaging sharp targets such as archaeological structures. Alternative approaches requires either a priori information about the subsurface (e.g. disconnect inversion) or requires two or more geophysical datasets to be collected at the same site (e.g. joint inversion). Here we propose a 3D inversion strategy that does not require a priori information and is theoretically more appropriate for imaging targets with sharp resistivity contrasts. Our approach combines an initial smoothness constraint inversion that is used only at the first iteration to recover a resistivity model that is fairly consistent with the measured data, from which an initial target location is estimated using an edge detector method and from which a disconnect in the inversion is identified. This disconnect defining the target outline is then progressively improved following each iteration of the inverse procedure. We applied our approach on 3D synthetic studies that include a single cavity, widely and closely spaced cavity models. In addition, we tested our approach on a challenging synthetic field model scenario that simulates archaeological field sites in Egypt. Synthetic studies demonstrate the effectiveness of our approach in recovering both resistivity and geometry of buried targets over the smoothness constraint inversion approach.

[1]This chapter has been accepted as: Elwaseif, M., and Slater, L., 2012, Improved Resistivity Imaging of Targets with Sharp Boundaries Using an Iterative Disconnect Procedure, Journal of Environmental and Engineering Geophysics, Accepted.

4.1. Introduction

The resistivity method is used to predict buried targets that have a detectable electrical resistivity contrast relative to the host medium. The success of the method in imaging targets is based on employing both an appropriate data collection setup and an appropriate inversion strategy honoring the characteristics of the subsurface environment. The data collection setup should take into account a number of parameters such as subsurface geology, depth and dimensions of investigated targets (e.g., Loke, 2004). Such parameters would determine the amount of injected current to the ground, array configuration, and electrode spacing. Recent advances in multi-channel resistivity meters, in addition to advances in computing power make three-dimensional (3D) resistivity surveys more common, less time consuming and less cost-prohibitive. Such 3D surveys and accompanying 3D inversion are inherently more appropriate to image targets such as isolated cavities at archaeological sites than 2D surveys and 2D inversion, since such cavities are inherently 3D targets.

The choice of an appropriate inversion strategy is based upon the availability of *a priori* subsurface information from geological logs or information from other geophysical methods, along with the characteristics of the edge of suspected targets [i.e., diffuse vs. sharp]. In the absence of *a priori* subsurface information on the geometry and distribution of buried targets, the smoothness constraint inversion is utilized to produce smooth resistivity images that represent the minimal structure required to satisfy the data. Such a regularization constraint is often very appropriate when the objective is to predict changes in resistivity due to variations in moisture and/or salinity across space and time.

However, when the objective is to predict targets that have sharp resistivity edges (e.g., cavities, tunnels, voids), the smoothness constraint is conceptually inappropriate as such targets represent a sharp change in resistivity across some unknown boundary location. Therefore, it is difficult to assess the true resistivity and edges of these targets from the obtained resistivity models.

When *a priori* information is available, other inversion strategies more appropriate for defining sharp resistive targets such as disconnect or joint inversion can be utilized. For example, Slater and Binley (2006) describe a modification of the smoothness constraint to accommodate sharp boundaries whereby a 'disconnect' in the smoothing is defined along the boundary of an object. The inversion then solves for a smoothly varying model structure across the host medium and within the disconnected target but does not permit smoothing across the boundary defined by the disconnect. Bouchedda et al. (2012) describe a joint structural inversion algorithm for cross-hole electrical resistance tomography (ERT) and cross-hole radar travel time tomography (RTT) that better reconstruct zones characterized by sharp boundaries.

A few studies have been conducted to improve the reconstruction of targets characterized by sharp boundaries without the need for *a priori* information. For example, Hordt et al. (2007) and Blaschek et al. (2008)) describe a 2D complex resistivity inversion that incorporates a regularization parameter that attempts to estimate sharp boundaries based on minimum gradient support. However, since different values of that regularization parameter will lead to different models, these studies still require additional constraints

on expected subsurface geology to achieve a reliable model. Elwaseif and Slater (2010) describe processing procedures for the reconstruction of geometries and resistivities of buried targets. Their approach combines an initial 2D smoothness constraint inversion coupled with a digital image processing technique known as the watershed algorithm to predict the target boundary and a second inversion step incorporating a disconnect in the regularization based on the boundary output by the watershed algorithm. Although this approach resulted in an improved estimate of the geometries of individual targets, it was not very effective at predicting the resistivity of the targets or resolving closely spaced targets. Elwaseif and Slater (under review) enhanced their previous approach by replacing the second disconnect inversion step with a trained Artificial Neural Network (ANN). Although this approach has been proven effective for resolving widely and closely spaced archeological targets, it is time consuming and the results depend largely on the quality of ANN training.

Here we propose a 3D resistivity inversion approach that does not require *a priori* information, and is more appropriate for imaging targets with high resistivity contrasts. Our approach combines smoothness constraint and disconnect inversion coupled with a digital edge detector technique called Roberts' cross-gradient operator to improve the model through iterative updates of both the resistivity model parameters and the disconnect boundary. We tested our combined inversion approach on 3D synthetic studies that of a single cavity, widely and closely spaced cavity models, and a field model scenario.

We focus on synthetic studies of discrete targets representative of expected features at archaeological sites in Egypt. We emphasize that, in such archaeological studies, recovering the geometry and resistivity of those targets is needed to fulfill the objectives of a non-invasive archaeological survey. The resistivity of these targets provides information on the material filling the cavities, whereas the geometry of these targets is important for performing a successful excavation operation. Synthetic studies demonstrate the effectiveness of our approach in recovering the resistivity and geometry for single and multiple cavity features.

4.2. Methodology

4.2.1. Smoothness constraint and disconnect inversion

The objective of resistivity inversion is to find a model that contains a resistivity structure consistent with expectations regarding the likely distribution of resistivity within the subsurface, whilst providing a set of theoretical measurements that fit the measured data to some pre-described acceptable level (e.g., Loke et al., 2003; Gunther et al., 2006). The smoothness constraint inversion is utilized to produce smooth resistivity images that represent the minimal structure required to satisfy the data (respecting the noise level) when subsurface *a priori* information is absent. Smoothness regularization is commonly based on two minimization schemes commonly referred to as the L2 norm and the L1 norm (Ellis and Oldenburg, 1994). The L2 norm emphasizes models with smoother variations of resistivity as it minimizes the squares of the differences between the measured and modeled transfer resistances and/or differences between the estimated

model and expected model structure. The L1 norm emphasizes models with sharper boundaries between regions of different resistivity, since it minimizes the absolute differences between measured and modeled resistivity values (and/or differences between the estimated model and expected model structure) (Loke et al., 2003). The L1 norm is therefore conceptually more appropriate for imaging sharp resistive targets than the L2 norm, although it suffers from being more sensitive to data noise (Hordt et al., 2007).

The resistivity inversion is an underdetermined problem since the number of model parameters is much larger than the number of measurements. In addition, since many models can fit the measured data to the same accuracy level, regularization is a critical component in the inversion process to ensure finding a reasonable resistivity model. The smoothness constraint inversion is carried out by solving the following objective function (Claerbout and Muir, 1973):

$$\varphi(\mathbf{m}) = \frac{1}{2}\|\mathbf{W_d}(\mathbf{d_{meas}} - \mathbf{d_{obs}})\|^2 + \frac{\beta}{2}\|\mathbf{W}(\mathbf{m} - \mathbf{m_{ref}})\|^2 \quad \ldots(4.1)$$

where W_d is the data weighting matrix, d_{meas} represents forward response for a specified model, d_{obs} is the measured field data, β is the regularization parameter, **W** is the regularization matrix, **m** is a model at a given iteration, and $\mathbf{m_{ref}}$ is the reference model. The objective function in equation (4.1) has both data and model terms to ensure obtaining a reliable final model. The first term, data misfit, ensures that the forward response of the predicted model is consistent with the measured data. The data weighing matrix permits incorporation of the data noise in the inversion process. The second term forces the model to fit our expectations based on the *a priori* information contained in the

regularization matrix. The regularization matrix has the following form (Loke and Lane, 2002):

$$\mathbf{W} = \alpha_x \mathbf{C}_x^T \mathbf{R}_m \mathbf{C}_x + \alpha_y \mathbf{C}_y^T \mathbf{R}_m \mathbf{C}_y + \alpha_z \mathbf{C}_z^T \mathbf{R}_m \mathbf{C}_z \ldots (4.2),$$

where α is the smoothing parameter, **C** is the roughness matrix, and $\mathbf{R_m}$ is the model weighting matrix. Starting from a homogeneous earth model, the Gauss-Newton approach is used to invert for the 'best' model that is close to our priori expectations and well fits the observed data. The approach minimizes the objective function by estimating the model perturbation using the following equation (Pidlisecky et al., 2007):

$$(\mathbf{J}^T\mathbf{J} + \beta\mathbf{W}^T\mathbf{W})\Delta\mathbf{m} = -\left(\mathbf{J}^T(\mathbf{d}_{meas} - \mathbf{d}_{obs}) + \beta\mathbf{W}^T\mathbf{W}(\mathbf{m} - \mathbf{m}_{ref})\right) (3)$$

$$(\mathbf{J}^T\mathbf{J} + \beta\mathbf{W}^T\mathbf{W})\Delta\mathbf{m} = -\left(\mathbf{J}^T(\mathbf{d}_{meas} - \mathbf{d}_{obs}) + \beta\mathbf{W}^T\mathbf{W}(\mathbf{m} - \mathbf{m}_{ref})\right) (4.3)$$

where **J** is the Jacobian matrix and Δ**m** is the model perturbation.

The disconnect inversion is a modification of the traditional smoothness constraint to accommodate sharp boundaries whereby a 'disconnect' in the model space is defined along the boundary of an object (Slater and Binley, 2006). However, the method requires that the boundary of the target be known *a priori*. In the case of a known subsurface boundary, the disconnect inversion is be implemented by giving small weights within the weighting matrix at the position of the boundary and specifying a different regularization weight inside the boundary region (e.g., Loke and Lane, 2002; Bouchedda et al., 2012). The regularization matrix (equation 4.2) is then updated based on the information

contained in the weighing matrix, which results in models containing sharp gradients at the locations of a known boundary.

4.2.2. Edge detection using Roberts' Cross-gradient Operator

Edge detector methods can be applied on resistivity images to locate the edges of different target anomalies. Locating an edge involves applying filter masks to compute the magnitude of the gradient at every pixel location within an image (Gonzalez and Woods, 1992). The masks employed in the Roberts' cross-gradient operator (Robert, 1963) and sample image are shown in Figure 4.1. Consider a 3 x 3 resistivity image having gray values with intensity "Z_i" where i = 1 to 9. The first-order partial derivative at Z_5 in the x and y directions can be estimated using equations (4.4 and 4.5),

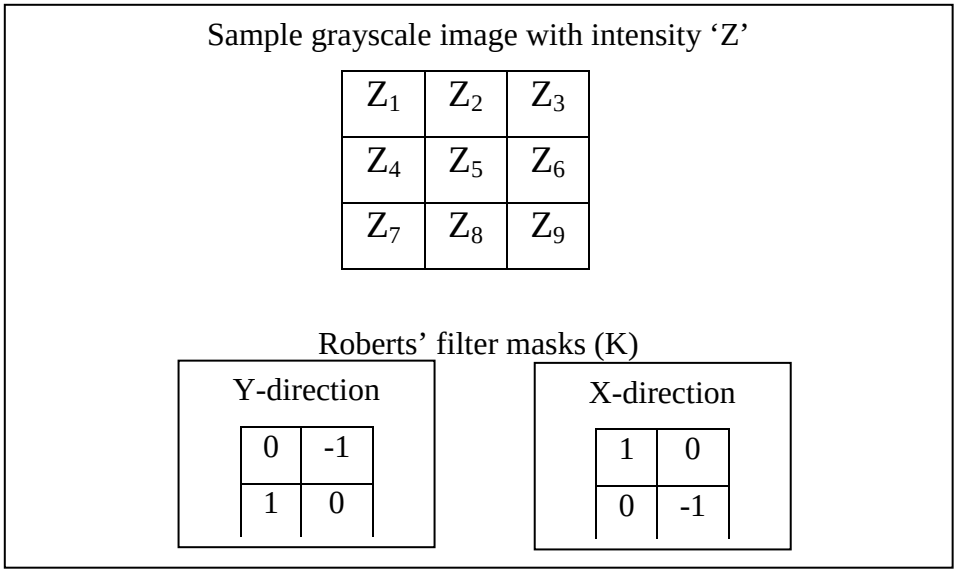

Figure 4.1: An example image and masks used to compute the edges using Roberts' operator (after Gonzalez and Woods, 1992).

$$G_x = (Z_9 - Z_5)K \ldots (4.4)$$

$$G_y = (Z_8 - Z_6)K \ldots (4.5)$$

where **K** is the Roberts' filter masks shown in Figure 4.1.

The magnitude of the gradient, as well as the direction of an edge perpendicular to the direction of a gradient vector, are computed using equations (6 and 7) (Gonzalez and Woods, 1992).

$$\nabla f = mag(\nabla F) = \left[G_x^2 + G_y^2\right]^{\frac{1}{2}} k \ldots (4.6)$$

$$\propto (x, y) = tan^{-1}\left(\frac{G_y}{G_x}\right) k \ldots (4.7)$$

The Roberts' cross-gradient Operator was selected among other popular edge detector methods such as Canny (Canny, 1986) and Sobel (Engel et al., 2006), since it provided more accurate edges when tested on different 3D resistivity images. Figure 4.2 shows a comparison between the performances of the three edge detector methods when applied on a resistivity image to locate the edges of two anomalies. The Canny method overestimated the edge locations and created additional unrealistic edges, whereas the Sobel method underestimated the edge locations. The Roberts' method gives the closest approximation to the actual edges.

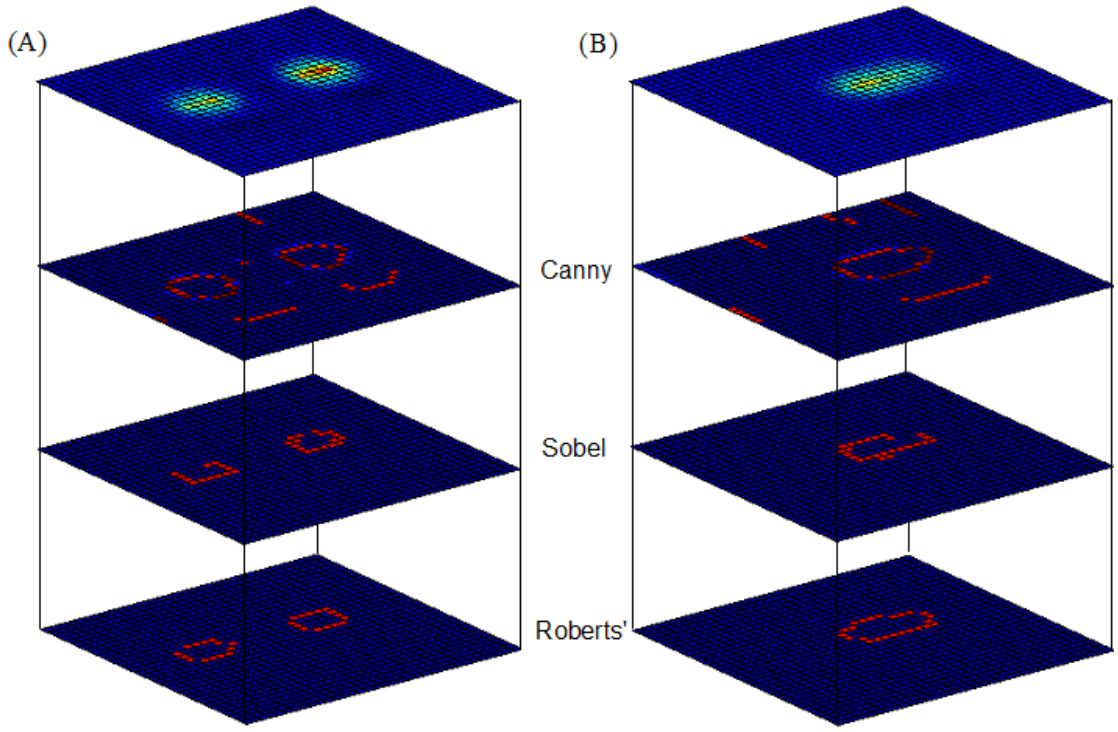

Figure 4.2: Results of applying the Canny, Sobel, and Roberts' edge detectors on the (A) widely spaced cavity model, and (B) closely spaced cavity model.

4.2.3. Description of the approach

We propose a combined inversion strategy that does not require *a priori* information and involves both smoothness constraint and disconnect inversion coupled with digital image processing. The disconnect inversion is carried out using *a priori* information on the target locations obtained from the Roberts' cross-gradient operator. The major element and advantage of our approach is that it iteratively improves the location of the disconnect boundary after each iteration, allowing for a better prediction of both resistivity and geometry of buried targets.

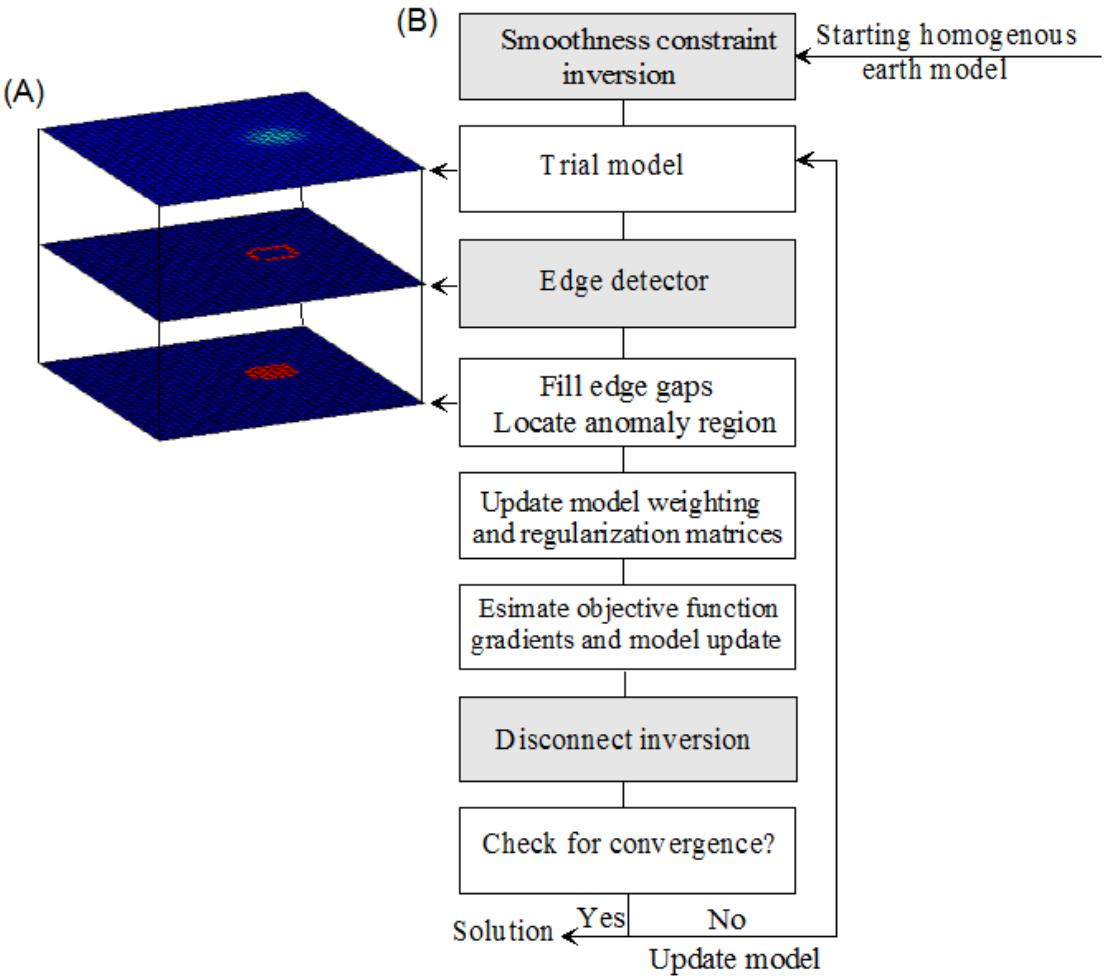

Figure 4.3: Flow chart showing (A) digital image processing steps and (B) the processing steps used in this study.

The sequence of processing steps involved in our approach is described in Figure 4.3. During the inversion process, starting from a homogenous earth model, the smoothness constraint inversion is performed only on the first iteration of the non-linear iterative optimization algorithm, since it usually produces an initial resistivity model that is fairly consistent with the measured data The Roberts' cross gradient operator is then applied on that model to predict the edges of any targets. A second image processing step is then applied on the resultant edge detector image to ensure that the predicted edge is fully

closed and to fill the boundary region. The result of the second step is a binary image with 1's located at the anomaly region and 0's everywhere else. The latter two steps help to identify the location of the edges and the entire anomaly regions as shown in Figure 4.2a. Those locations are then used to update the model weighting and regularization matrices as described above. The inversion process then progresses using the disconnect inversion and the above steps are repeated until the solution converges. Figure 4.4 shows the iterative inversion results for the single cavity model using our approach. The resistivity and geometry of the cavity anomaly progressively improve after each iteration.

4.3. Synthetic models

We calculated the synthetic apparent resistivity datasets for a sediment filled single cavity, two widely spaced cavities (separation >> unit electrode spacing), two closely spaced cavities (separation < unit electrode spacing), and a field model scenario consists of a single cavity buried underneath a top resistive layer considered to be representative of site conditions in Egypt. The 3D forward modeling datasets were generated using the forward modeling and inversion code, RESINVM3D (Pidlisecky et al., 2007). The cavities were assigned a resistivity of either 500 or 1000 Ohm m, whereas the host medium was assigned a resistivity of 100 Ohm m in all scenarios. These were considered reasonable representative values based on known results from cavities at archaeological sites in Egpyt (e.g., Metwaly et al., 2005). We followed the simulation setup as described in Pidlisecky et al. (2007). In each case, ninety six electrodes were used to create the synthetic data; thirty eight of these electrodes act only as potential electrodes, whereas the remaining fifty eight electrodes act as both current and potential electrodes. The electrode

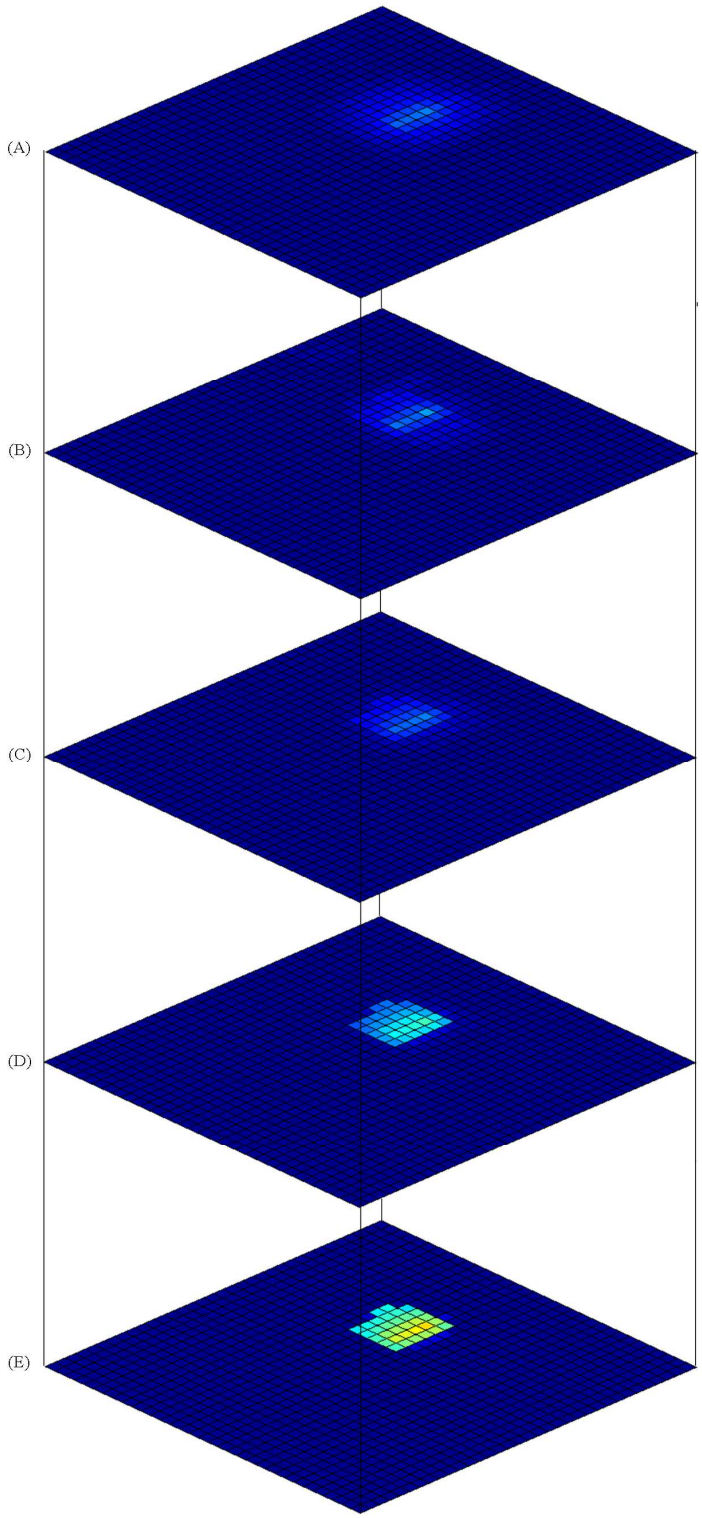

Figure 4.4: Example of the combined inversion results per iteration (A) first iteration using smoothness constraint inversion, (B) to (E) are the second to fifth iterations using disconnect inversion.

spacing is 1m and the simulations involve forty one independent current pairs. For each of these pairs, data are recoded using dipoles at the remaining ninety four electrodes, providing 3813 measurements for each model scenario. All synthetic datasets were contaminated with 3% Gaussian noise, representative of noise levels expected in typical field data.

The first single cavity model involved a cavity buried at 1.3 m depth, having a width and breadth of 2.5 m and a length of 1.5 m and resistivity of 1000 Ohm m (Figure 4.5a). The second scenario involved two cavities having the same geometry (depth, breadth and length) as the single cavity and resistivity values of 500 and 1000 Ohm m. Two cases of this two cavity model were considered (a) a widely-spaced cavities spaced 4 m apart (edge to edge) i.e. greater than unit electrode spacing (Figure 4.6a); (b) a closely-spaced cavities model spaced 0.5 m apart (edge to edge) i.e. less than the unit electrode spacing (Figure 4.7a). In the last scenario (Fig. 4.8a), a single cavity was buried at 1.7 m depth, having a width and breadth of 4 m, length of 1.7 m and resistivity of 1000 Ohm m, overlain by a high resistivity (2000 Ohm m), 1.7 m thick layer. This model is more representative of expected field scenarios at archaeological sites in southern Egypt, where the hot weather conditions makes the near surface soil resistive (Elwaseif and Slater, 2010).

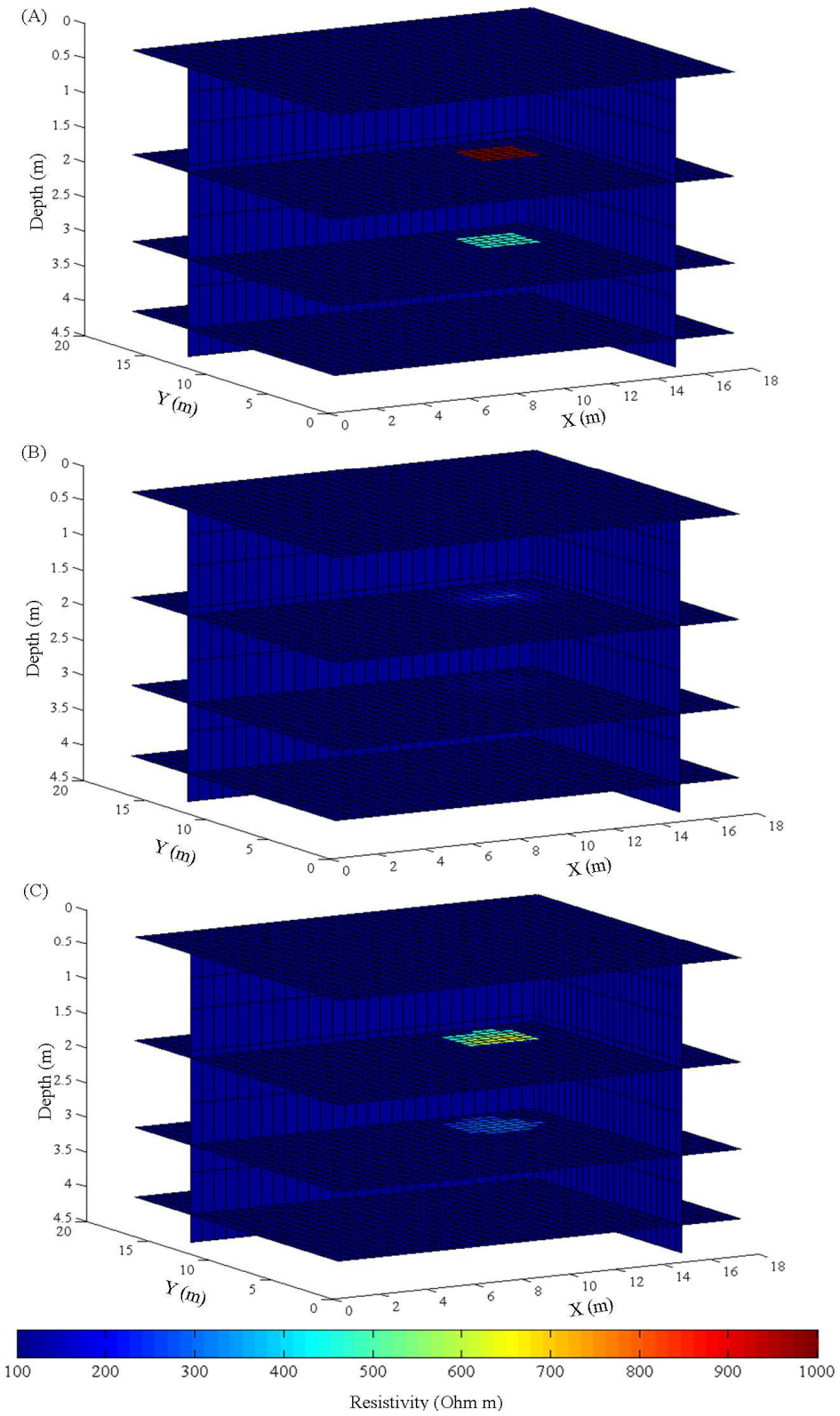

Figure 4.5: Inversion results of the single cavity model (A) subsurface model (B) smoothness constraint inversion (C) combined smoothness and disconnect inversion

4.3.1. Smoothness constraint inversion

The synthetic data were inverted using RESINVM3D (Pidlisecky et al., 2007). The regularization part of the code was modified to perform our iteratively updated disconnect inversion approach. We chose to invert all the data using the L1 norm approach, since cavities exhibit sharp contrasts within the host medium at distinct boundaries. In all cases a homogeneous medium based on the average apparent resistivity of the synthetic dataset was used as the starting model, and five iterations were performed. The results of applying the inversion on the single, widely spaced, closely spaced cavity, and field model are shown in Figures 4.5b, 4.6b, 4.7b and 4.8b, respectively. In all cases, the resistivity value of the recovered targets is underestimated. In addition, it is difficult to identify a clear outline of each target anomaly. The widely spaced cavities are clearly associated with individual anomalies in the resistivity images (Fig. 4.6b). However, the two closely spaced cavities appear as a single anomaly (Fig. 4.7b), instead of two separate features, due to the small spacing between cavities (here less than the unit electrode spacing). Finally, the single cavity in the field model scenario (Fig. 4.8b) is not clearly recovered, due to the highly resistive overburden.

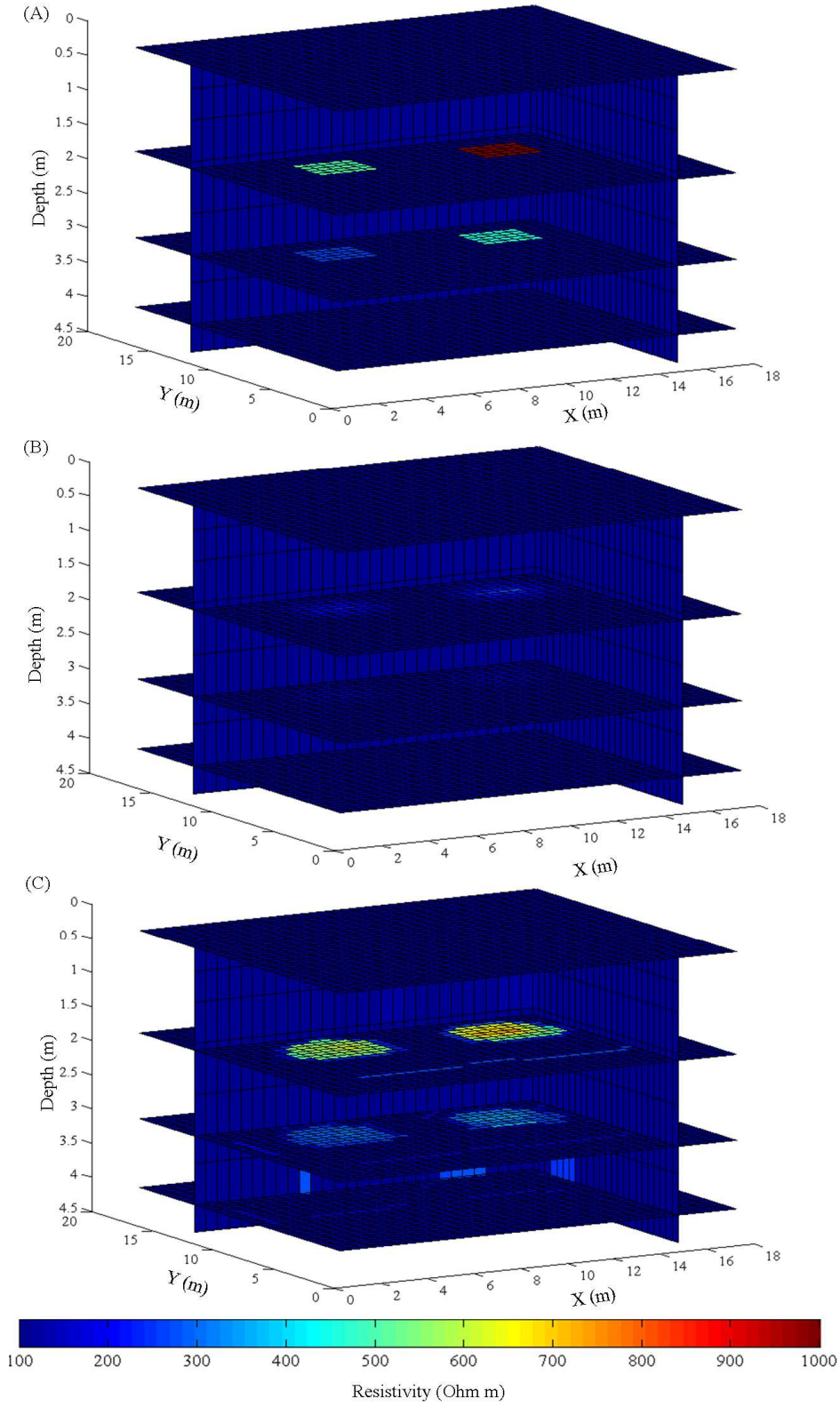

Figure 4.6: Inversion results of the widely spaced cavity model (A) subsurface model (B) smoothness constraint inversion (C) combined smoothness and disconnect inversion

4.3.2. Re-inverting datasets using our combined inversion approach

The geometry and resistivity of different synthetic targets are difficult to predict from the smoothness constraint inversion results, since the method produces models characterized by a smooth distribution of resistivity over a wide range of values. Re-inverting the data with an additional constraint on the inferred location of cavity boundaries could lead to an improved estimate of resistivity structure within the host medium or within the target (Elwaseif and Slater, 2010). Figures 4.5c, 4.6c, 4.7c and 4.8c show the final inverted images of the single cavity, widely spaced double cavity, closely spaced double cavity, and the synthetic field model using the combined inversion approach described in Figure 4.3. Our approach results in an improved recovery of both resistivity structure of the single cavity and widely spaced cavity models relative to that obtained from the smoothness constraint inversion. The edge detector method was unsuccessful in resolving two separate closely spaced anomalies (Figure 4.2) presumably because there was not sufficient grey level contrast within the single feature resolved by the inversion. However, the result for the closely spaced model clearly depicts the presence of two resistive features coincident with the cavities. Consistent with the true model, the cavity on the left is predicted as the more resistive. Finally, the resistivity of the single cavity and the top resistive layer of the field model scenario are better recovered using our approach (Fig. 4.8c). In addition, the combined inversion clearly shows the outline of the single cavity especially at higher depth. However, it shows the same inversion artifacts as in the smoothness constraint inversion results.

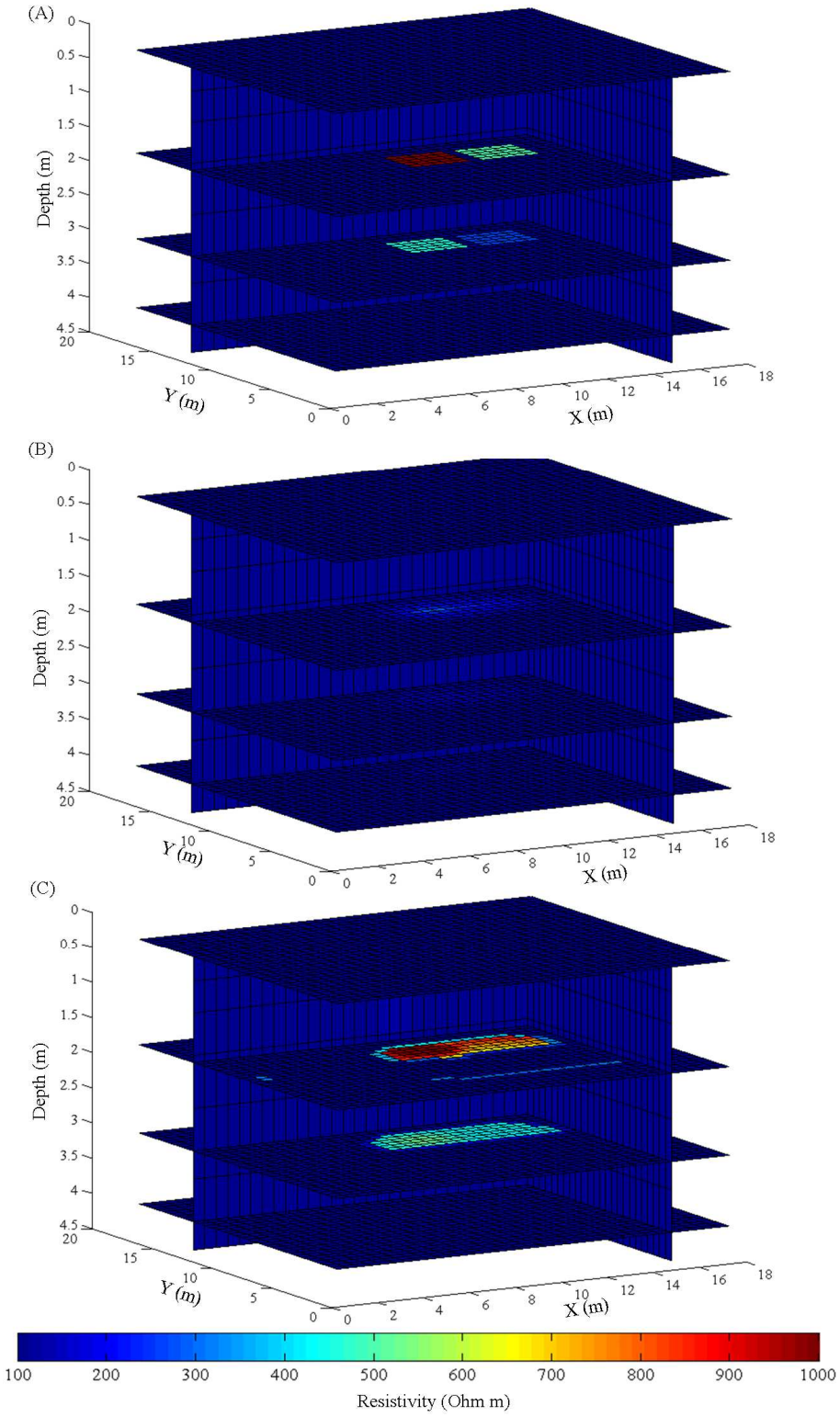

Figure 4.7: Inversion results of the closely spaced cavity model (A) subsurface model (B) smoothness constraint inversion (C) combined smoothness and disconnect inversion

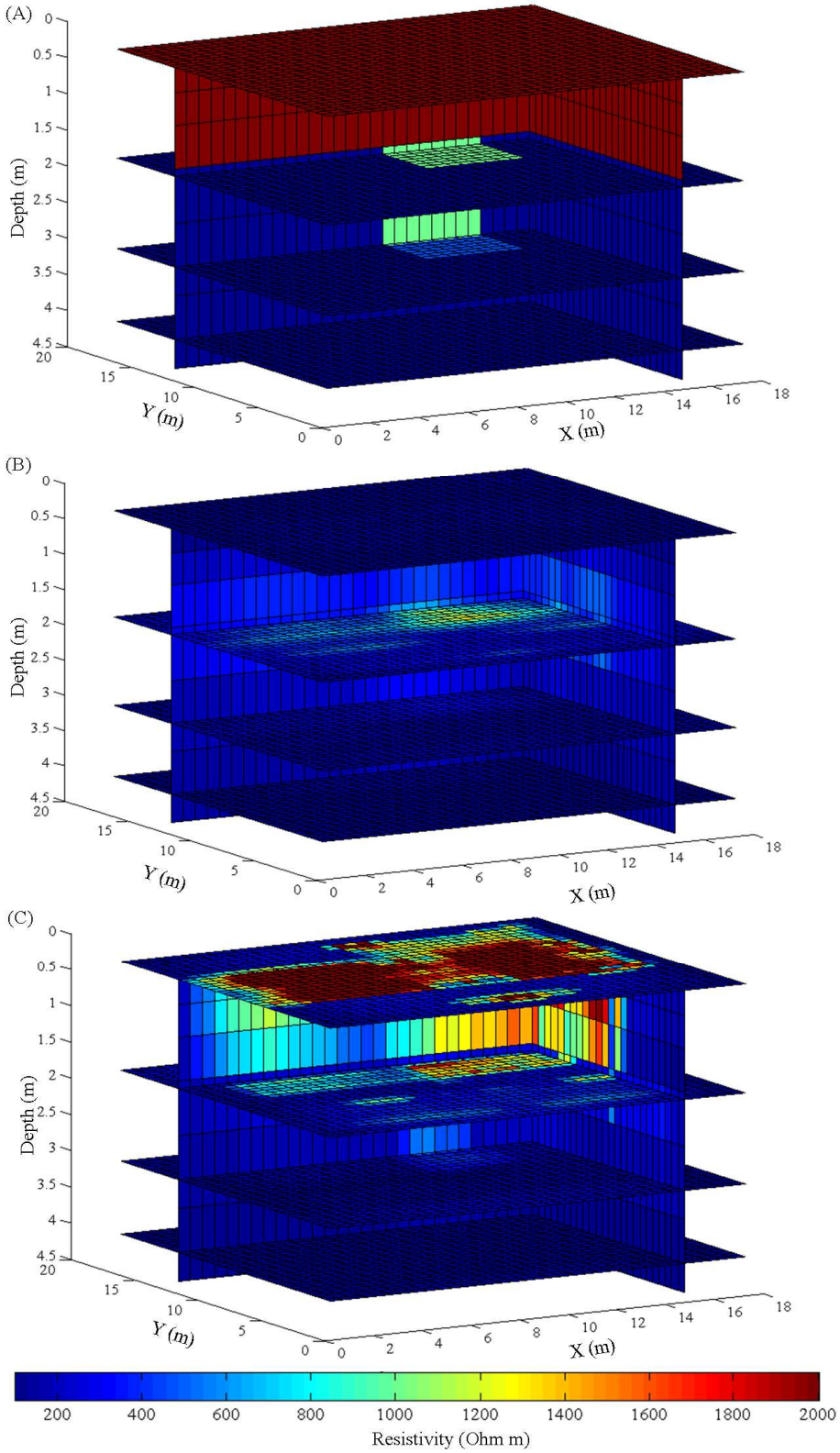

Figure 8: Inversion results of the synthetic field data model (A) subsurface model (B) smoothness constraint inversion (C) combined smoothness and disconnect inversion.

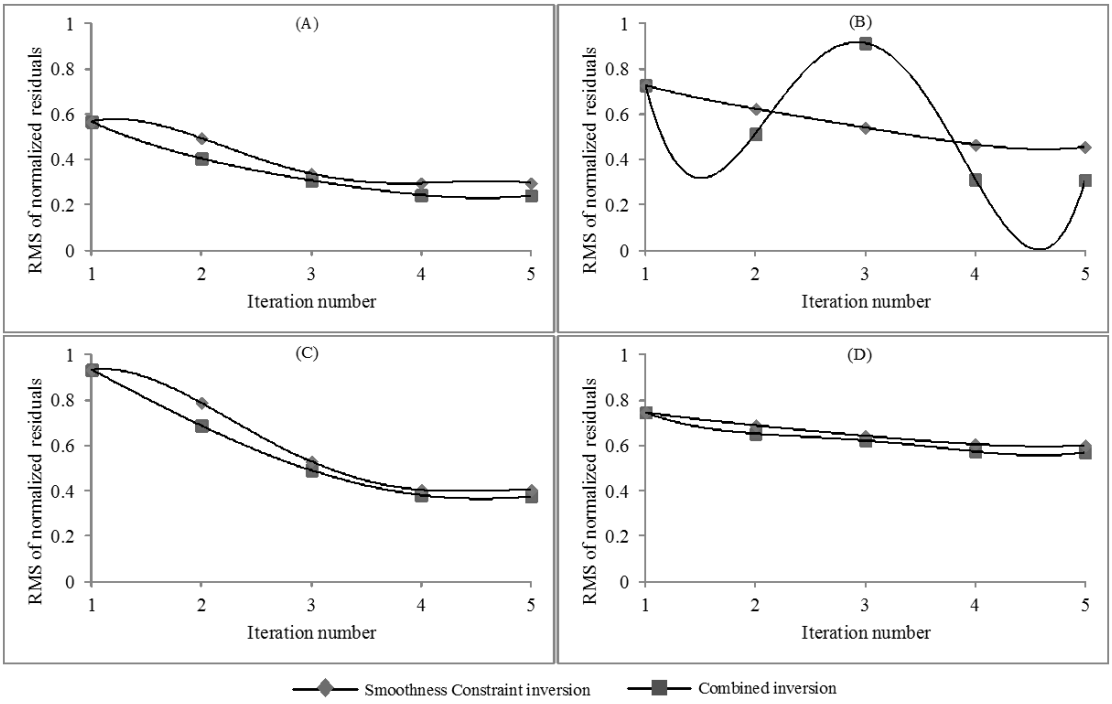

Figure 4.9: RMS values of the normalized residuals for different models (A) single cavity (B) widely spaced cavity (C) closely spaced cavity (D) field model.

To assess the performance of the smoothness constraint and our combined inversions in a more quantitative way, the values of data misfit curves are plotted at all five iteration steps for different model scenarios in Figure 4.9. The misfits are low for all models. However, the RMS curve of the combined inversion in Figure 4.9b shows an oscillatory pattern, suggesting that the solution is trapped in a local minimum at iteration 3. Despite this disturbance, the average data misfits for all iterations are about 6% lower in the case of the combined inversion.

4.4. Discussion

The commonly applied smoothness constraint inversion is not ideal for imaging buried targets with sharp resistivity edges, since it generates models characterized by a smooth

distribution of resistivities over a wide range of values. For example, based on the synthetic studies, the single cavity and the closely spaced cavities models show similar smooth inversion results and both images would likely be interpreted as evidence of a single buried cavity. Using a disconnect boundary in the inversion can improve imaging the geometry and resistivity of such targets. As shown in Figure 6b, although the closely spaced targets are not individually resolved, the resistivity of these targets is close to the actual resistivity values (i.e., 500 and 100 Ohm m).

We have shown here that such disconnect boundary can be estimated *without a priori information* using the Roberts' cross-gradient operator. In addition, unlike traditional disconnect inversion that has a fixed location of the known boundary, our approach optimizes the location of the boundary after each iteration. Such updates will refine the estimate of the anomaly edges and results in improved target location.

We have described a 3D inversion approach whereby the smoothness constraint inversion is used only at the first iteration to recover a resistivity model that is fairly consistent with the measured data, from which an initial target location is determined using an edge detector method and from which the disconnect inversion is able to optimize.

The performance of our approach depends significantly on the accuracy of the edge detector step. We assume that the boundaries of cavities predicted using the Robert's cross-gradient operator are consistent with the edges of resistivity models characterized

by sharp boundaries for which we only have a smooth resistivity model. However, the success of the edge detector method to predict accurate target boundaries depends on the success of the initial smoothness constraint inversion step in defining the general location of investigated targets. That said, the final model obtained from our inversion strategy is sensitive to the definition of the boundary extracted from the Roberts' cross-gradient operator. However, even when the Roberts' cross-gradient operator method cannot accurately reproduce the target dimensions, we find that our approach can still improve the interpretation of the subsurface model structure. For example, although the Roberts' cross-gradient operator was not able to identify a boundary between the closely spaced cavity model because of the low gray level contrast between the two anomalies (see Figure 2b), the recovered resistivity values of the two cavities are close to the actual resistivity values.

Results from the synthetic studies suggest that our approach has potential for reconstructing the geometry and resistivity of discrete targets in field datasets. One advantage of our approach is that it does not require *a priori* information and the entire processing steps are done automatically within the inversion routine without any interference from the user. However, the approach might suffer from distinct limitations when applied to field data as the effect of inversion artifacts on the final model result is currently unclear. Given that the field studies are far more complex than the synthetic studies presented here, the inversion might contain unrealistic anomalies and both the edge detector and disconnect inversion would deal with those artifacts as real anomalies. For example, given the inversion results of the synthetic field model scenario (Fig. 8), it

is clear that our combined inversion approach recovers the resistivity and geometry of the single cavity better than the smoothness constraint inversion. However, the approach magnifies the artifacts in the smoothness constraint model. Therefore, it will be necessary to avoid inversion artifacts by correctly quantifying noise levels in the data and starting with a homogenous model that represents the best guess of the *in situ* resistivity. In the case of no priori information about the background resistivity, it is appropriate to use the average value of the measured apparent resistivities as a starting model.

4.5. Conclusions

Application of the smoothness constraint inversion coupled with an interatively updated inversion disconnect and digital image processing, appears to be a viable approach for determining the resistivity and location of discrete targets in resistivity datasets. We have shown that the predicted boundaries and resistivity of the targets using our combined inversion approach are significantly improved when compared with results from the smoothness constraint inversion. Using this approach the geometry and resistivity of multiple targets, even when separated by a distance less than the unit electrode spacing, are fairly well recovered. The approach appears promising for predicting archaeological artifacts in Egypt where the field model scenario presented here confirmed the effectiveness of our approach. In addition to archaeological artifacts, the approach will also be appropriate for predicting the location of engineering structures and voids in karst environments.

Chapter 5: Conclusions

5.1. Summary and conclusions

The main objective of this research was to develop a resistivity inversion strategy that: [1] does not require priori information, and [ii] is more appropriate for recovering the geometry and resistivity of isolated and closely spaced targets particularly those expected at archaeological sites in Egypt. I have developed three resistivity inversion approaches that were applied on field data collected at an archaeological site in Egypt and/or synthetic data representative of expected features at archaeological sites in Egypt. The common idea of the three approaches is centered on applying edge detector techniques on smooth resistivity models explicitly or implicitly during the resistivity inverse procedures. The first approach involves applying a watershed algorithm on 2D smooth resistivity images to predict target boundaries that can subsequently be used to define disconnects in the inversion, whereas the second approach uses the predicted boundaries from the watershed algorithm along with the L1 norm recovered host medium resistivity and target's central resistivity as an input to a trained ANN. The final approach is a 3D iterative inversion strategy that combines smoothness constraint inversion that is used only at the first iteration to recover a resistivity model that is fairly consistent with the measured data, from which an initial target location is estimated using Roberts cross-gradient operator and from which a disconnect in the inversion is identified and updated until the solution converges. Generally, the three approaches improve the resistivity imaging of investigated targets better than the smoothness constraint inversion. The first approach is effective only at predicting the geometry of isolated resistive targets.

Although the second approach is effective in estimating the geometry and resistivity of isolated and closely spaced resistive targets, the output of the ANN depends largely on the initial L1 inversion step and the accuracy of the watershed predicted geometry. The third approach, in contrast, gives the optimum results over other approaches in terms of speed, and confidence levels of retrieval.

5.2. Technical contributions

The dissertation presents three novel strategies for offsetting the pitfalls that result from applying the smoothness-based regularization approach for reconstruction of the geometries and resistivities of subsurface resistivity targets at archaeological sites in Egypt. The first two approaches can be applied to inverted resistivity images directly, without needing raw data, to extract quantitative information on target dimensions not ascertainable from the inverted images. Furthermore, the boundaries can subsequently be used as input to a trained ANN in order to estimate an updated model of the resistivity structure of the targets. The third iterative disconnect procedure approach can be applied as well to determine the resistivity and location of conductive discrete targets in resistivity datasets. In addition, the three approaches will also be appropriate for predicting the location of engineering structures and voids in karst environments.

5.3. Recommendations for future work

The watershed algorithm appears to be an effective approach at predicting targets geometries from the smooth resistivity images examined in this research. However, further work is needed to examine the performance of the watershed algorithm under

more complex model scenarios (e.g., models that contain targets having different geometries, varied resistivity values and buried in heterogeneous host medium). Furthermore, more work is needed to better understand the effects of using different inversion algorithms on the watershed results and also to find ways to enhance the geometry prediction of the watershed algorithm when applied to noisy data sets.

The application of the ANN approach on more field data collected at different archaeological sites in Egypt is needed to refine the approach, for example, by increasing the learning capacity of the ANN by training it using real field data.

Although the iterative disconnect approach has been proven effective in synthetic studies, application of the method on field data is essential to examine the performance of the approach. Furthermore, finding alternative edge detector methods more appropriate in predicting edges in 3D smooth images and more efficient in predicting closely spaced targets might significantly improve the performance of the approach. In addition to examine it on field archaeological data, the approach can be adapted to invert hydrogephysical resistivity data, particularly when there is a sharp change in resistivity between subsurface layers.

References

Adler, A., Dai, T. Lionnheart, W.R.B., 2007. Temporal image reconstruction in electrical impedance tomography. Physiol. Meas., 28, S1-S11.

Barraud, J., 2006. The use of watershed segmentation and GIS software for textural analysis of thin sections, J. Volcanol. Geotherm. Res. 154, 17–33.

Blaschek, R., Hordt, A. Kemna, A., 2008. A new sensitivity-controlled focusing regularization scheme for the inversion of induced polarization data based on the minimum gradient support. Geophysics. 73, NO. 2, F45–F54.

Bouchedda, A., Chouteau, M., Binley, A. Giroux, B., 2012, 2-D joint structural inversion of cross-hole electrical resistance and ground penetrating radar data: Journal of Applied Geophysics, 78, 52–67.

Beucher, S., 1992. The watershed transformation applied to image segmentation, Cambridge, UK, Scanning Microscopy International suppl. 6, 299-314.

Burger, W., Burger, M., 2008. Digital Image Processing - An Algorithmic Approach using Java, 1st ed. Springer, New York

Canny, J., 1986, A computational approach to edge detection, IEEE Trans. Pattern Analysis and Machine Intelligence, vol 8, 679-714.

Casas , A., Himi, M., Diaz, Y., Pinto, V., Font, X. Tapias, J.C., 2007. Assessing aquifer vulnerability to pollutants by electrical resistivity tomography (ERT) at a nitrate vulnerable zone in NE Spain. Environmental Geology. 54, No. 3, 515-520.

Chambers, J.E., Kuras, O., Meldrum, P.I., Ogilvy, R.D. Jonathan, H., 2006. Electrical resistivity tomography applied to geologic, hydrogeologic, and engineering investigations at a former waste-disposal site. Geophysics. 71 , B231-239.

Christiansen, A.V. Auken, E., 2004. Optimizing a layered and laterally constrained 2D inversion of resistivity data using Broyden's update and 1D derivatives. Journal of Applied Geophysics. 56 , 247-261.

Claerbout, J.F., Muir, F., 1973, Robust modeling with erratic data, Geophysics, 38, 826-844.

Dahlin, T. Zhou, B., 2004. A numerical comparison of 2D resistivity imaging with 10 electrode arrays: Geophysical Prospecting. 52, 379–398.

Ellis, R.G. and Oldenburg, D.W., 1994, applied geophysical inversion: Geophysical Journal International, 116, 5-11.

El-Qady, G., Hafez, M., Abdalla, M. Ushijima, K., 2005. Imaging Subsurface Cavities Using Geoelectric Tomography and Ground-Penetrating radar. Journal of Cave and Karst Studies. 67, no. 3, 174–181.

Elwaseif, M., 2006. Application of Geophysics for Archaeological Prospection and Conservation of some Archaeological sites in the Western bank of Luxor – Egypt. MS thesis, Geophysics Dept., Faculty of science, Ain-Shams University.

Elwaseif, M., Slater, L., 2010, Quantifying Tomb Geometries in Resistivity ImagesUsing Watershed Algorithms, Journal of Archaeological Science, Vol. 37, Issue 7, pp 1424-1436.

Elwaseif, M., and Slater, L., 2012, Improved Resistivity Imaging of Targets with Sharp Boundaries Using an Iterative Disconnect Procedure, Journal of Environmental and Engineering Geophysics, Accepted.

Elwaseif, M., and Slater, L., under review, Improving Reconstruction of Discrete Resistivity Targets Using Coupled Artificial Neural Networks and Watershed Algorithms. Submitted to Near Surface Geophysics Journal (nsg-2011-0641).

Engel, K, Hadwiger, Kniss, J., Rezk-Salama, C., 2006, Real-Time Volume Graphics, 2006, A K Peters, Wellesley, MA.

Feng, H., Karl, W.C. Castanon, D.A., 2004. A curve evolution approach to object-based tomographic reconstruction. IEEE Transactions on Image Processing. 12, 44-57.

Frohlich, R., Barosh, P. Boving T., 2008. Investigating changes of electrical characteristics of the saturated zone affected by hazardous organic waste. Journal of Applied Geophysics. 64, 25–36.

Furman, A., Ferre, T.P.A. Warrick, A.W., 2003. A Sensitivity Analysis of Electrical Resistivity Tomography Array Types Using Analytical Element Modeling. Vadose Zone Journal. 2, 416-423.

Gibert, D., Nicollin, F., Kergosien, B., Bossart, P., Nussbaum, Ch., A. Grislin, A., Conil, F. Hoteit, N., 2006. Electrical Tomography Monitoring of the Excavation Damaged Zone of the Gallery 04 in the Mont Terri Rock Laboratory: Field Experiments, Modelling, and Relationship With Structural Geology. Applied clay Science. 33, 21-34.

Gibson, P.J., Lyle, P. George, D.M., 2004. Application of resistivity and magnetometry geophysical techniques for near-surface investigations in karstic terranes in Ireland. Journal of Cave and Karst Studies. 66, No. 2, 35–38.

Gokturkler, G., Balkaya, C., Erhan, Z. Yurdakul, A., 2008. Investigation of a shallow alluvial aquifer using geoelectrical methods: a case from Turkey. Environ Geol. 54, 1283–1290.

Gonzalez, R. Woods, R., 1992. Digital Imaging Processing, Prentice hall, New Jersey.

Gunther, T., Rucker, C. Spitzer, K., 2006. 3-d modeling and inversion of DC resistivity data incorporating topography - Part II: Inversion. Geophys. J. Int.166 , 506-517.

Hordt, A., Blaschek, R., Kemna, A., and Zisser, N., 2007, Hydraulic conductivity estimation from induced polarisation data at the field scale — the Krauthausen case history. Journal of Applied Geophysics, 62, 33-46.

Kemna, A., Vanderborght, J., Hardelauf, H. Vereecken, H., 2004. Quantitative imaging of 3D solute transport using 2D time-lapse ERT: a synthetic feasibility study: Proc. Symp. Application of Geophysics to Engineering and Environmental Problems, Environ. Eng. Geophys. Soc., 342-353.

Lane, J.W., Day-Lewis, F.D., Versteeg, R.J. Casey, C.C., 2004. Object-based inversion of crosswell radar tomography data to monitor vegetable oil injection experiments. Journal of Environmental & Engineering Geophysics. 9, issue 2, 63-77.

Leucci, G. De Giorgi, L., 2005. Integrated geophysical surveys to assess the structural conditions of a karstic cave of archaeological importance. Natural Hazards and Earth System Sciences. 5, 17–22.

Leucci, G., 2006. Contribution of Ground Penetrating Radar and Electrical Resistivity Tomography to identify the cavity and fractures under the main Church in Botrugno (Lecce, Italy). Journal of Archaeological Science. 33, 1194-1204.

Leucci, G., Greco, F., Giorgi, L. Mauceri, R., 2007. Three-dimensional image of seismic refraction tomography and electrical resistivity tomography survey in the castle of Occhiola (Sicily, Italy). Journal of Archaeological Science. 34, 233-242.

Loke, M., 2004. 2-D and 3-D electrical imaging surveys, (PDF available from http://www.geoelectrical.com/).

Loke, M. H. Barker, R. D., 1996. Rapid least-squares inversion of apparent resistiity pseudosections by a quasi-Newton method. Geophysical Prospecting. 44, 131–152.

Loke, M., Acworth, I. Dahlin, T., 2003. A comparison of smooth and blocky inversion methods in 2-D electrical imaging surveys. Exploration Geophysics. 34, 182–187.

Loke, M.H., and Lane, J.W., 2002, The use of constraints in 2D and 3D resistivity modeling: Proceedings of the 8th meeting of the Environmental and Engineering Geophysical Society – European section.

Marescot, L., Palma Lopes, S., Rigobert, S. Green, A., 2008. Non-linear inversion of geoelectrical data acquired across 3D objects using a finite element method. Geophysics, 73, F 121- F 133.

Metwaly, M., Green, A., Horstmeyer, H., Maurer, H., Abbas, A., andHassaneen, A., 2005, Combined Seismic Tomographic and Ultra shallow Seismic Reflection Study of an Early Dynastic Mastaba, Saqqara, Egypt. Archaeol. Prospect. 12, 245–256.

Miller, C. R., Allen, A. L., Speece, M. A., El- Werr, A. Kh., and Link, C. A., 2005, Land Streamer Aided Geophysical Studies at Saqqara, Egypt. Journal of Environmental & Engineering Geophysics, 10, 371-380.

Negri, S., Leucci, G. Mazzone, F., 2008. High resolution 3D ERT to help GPR data interpretation for researching archaeological items in a geologically complex subsurface. Journal of Applied Geophysics. 65, 111–120.

Negri, S. Leucci, G., 2006. Geophysical investigation of the Temple of Apollo (Hierapolis, Turkey). Journal of Archaeological Science. 33, 1505-1513.

Nixon, M. Aguado, A., 2002. Feature extraction and Image processing, Newnes, Linacre House, Jordan Hill, Oxford OX2 8DP.

Park, G., Park, S., and Kim, J., 2010, Estimating the existence probability of cavities using integrated geophysics and a neural network approach, Computers & Geosciences, 36, 1161–1167.

Pidlisecky, A., E. Haber, and R. Knight (2007), RESINVM3D: A Matlab 3-D resistivity inversion package, Geophysics, 72(2), H1 – H10.

Raiche, A., 1991, A pattern recognition approach to geophysical inversion using neural nets., Geophysical Journal International, 105, 629-648.

Roberts, L., 1963, Machine Perception of Three-Dimensional Solids, Garland Publishing, New York.

Roerdink, J. B.T.M. Meijster, A., 2001. The Watershed Transform: Definitions, Algorithms and Parallelization Strategies, Fundamenta Informaticae. vol. 41, 187-228.

Roueff, A., Chanussot, J., Mars, J. Nguyen, M.Q., 2004. Unsupervised separation of seismic waves using the watershed algorithm on time-scale images. Geophysical Prospecting. 52, Issue 4, 287 – 300.

Rumelhart, D. E, Hinton, G. E., & Williams, R. J. (1986). Learning internal representations by error propagation. In E. Rumelhart, L. McClelland, & PDP Research Group (Eds.), Foundations: Vol. 1. Parallel distributed processing. Cambridge, MA: MIT Press.

Simpson, P.K., 1990, Artificial Neural Systems: Foundations, Paradigms, Applications, and Implementations, Pergamon Press, p.47-69.

Slater, L. Binley, A., 2003. Evaluation of permeable reactive barrier (PRB) integrity using electrical imaging methods, Geophysics, 68, No. 3, 911-921.

Slater, L., Binley, A., 2006. Engineered barriers for pollutant containment and remediation in: Vereeken, H., Binley, A., Cassiani, G., Revil, A. Titov, K. (Eds.), Applied Hydrogeophysics. NATO Science Series IV, Earth and Environmental Sciences, Springer, pp. 293-317.

Smith, M., 1993. Neural Networks for Statistical Modeling. Van Nostrand Reinhold, New York.

Soleimani, M., Lionheart, W.R.B. Peyton, A. J., 2007. Image reconstruction for high contrast conductivity imaging in mutual induction tomography for industrial applications. IEEE Trans. Ins. & Meas. 56, No. 5, 2024-2032.

Soupios, P., Papadopoulos, N., Papadopoulos, I., Kouli, M., Vallianatos, F., Sarris, A. Manios, T., 2007. Application of integrated methods in mapping waste disposal areas. Environ Geol. 53, 661–675.

Stanley, K. O., and Miikkulainen, R. (2002d). Evolving neural networks through augmenting topologies. Evolutionary Computation, 10(2), 99–127.

Stummer, P., Maurer, H. Green, A.G., 2004. Experimental design: Electrical resistivity data sets that provide optimum subsurface information. Geophysics, 69, No.1, 120-139.

Urbini , S., Cafarella, L., Marchetti, M., Chiarucci, P. Bonini, D., 2007. Fast geophysical prospecting applied to archaeology: results at Villa ai Cavallacci (Albano Laziale, Rome) site. Annals of Geophysics. 50, No. 3, 291-299.

Weinstein-Evron, M., Beck, A. Ezersky, M., 2003. Geophysical investigations in the Service of Mount Carmel Prehistoric Research. Journal of Archaeological Science. 30, 1331-1341.

Winkler, E., W. Seiberl, A. Ahl, 2003, Interpretation Of Airborne Electromagnetic Data with Neural Networks: In Geophysical Applications of Artificial Neural Networks and Fuzzy Logic, Sandham,W. and Leggett M. (Eds.), Kluwer Academic Publishers.

Zhang, L., and Poulton, M., 2001, Neural network inversion of EM39 induction log data: accepted in B. Sandham and M. Leggett (Eds), Geophysical Applications of Artificial Neural Networks and Fuzzy Logic: Kluwer Academic Publishing, Netherlands.

Appendices

Appendix I: Applying the watershed algorithm and disconnect inversion on resistivity images

[1] Required codes:

[a] A 2D resistivity forward modeling and inversion code such as Resd2inv and R2 (free for academic use).

[b] A digital image processing code with the watershed algorithm included such as ImageJ or Matlab with image processing toolbox included.

[2] Step by step instructions on applying the watershed algorithm on resistivity images:

[a] Plotting the inverted resistivity model without scaling the model resistivity values.

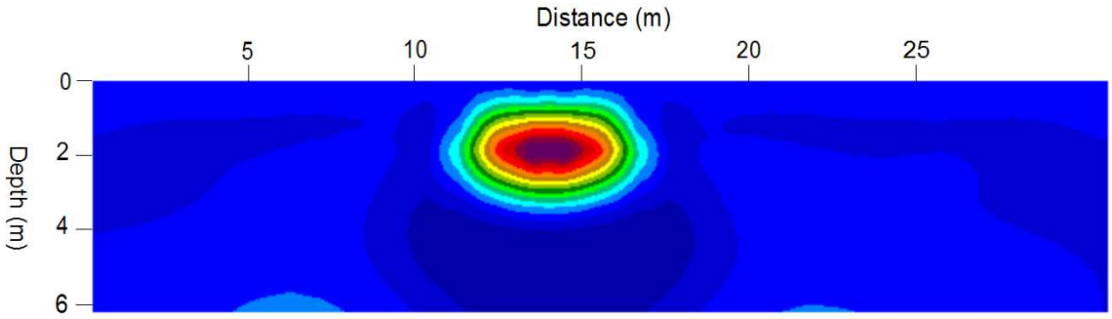

Inverted resistivity image

[b] Converting the resistivity image to a grey scale image.

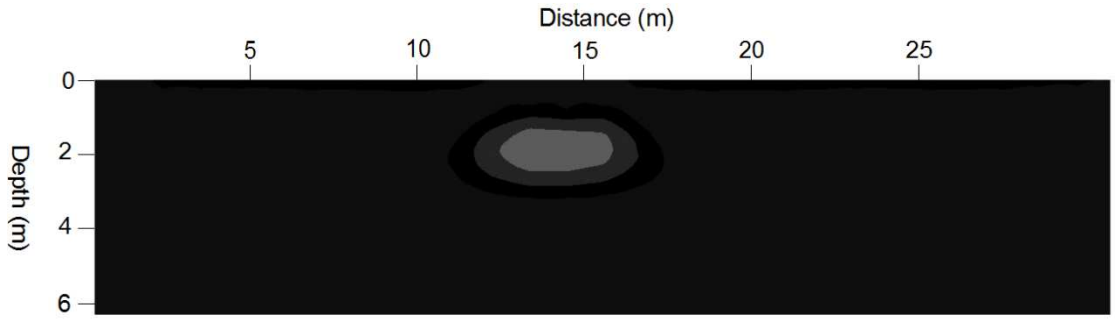

Grey scale resistivity image

[c] Applying the Gaussian blur and mean filters to the Grey scale image.

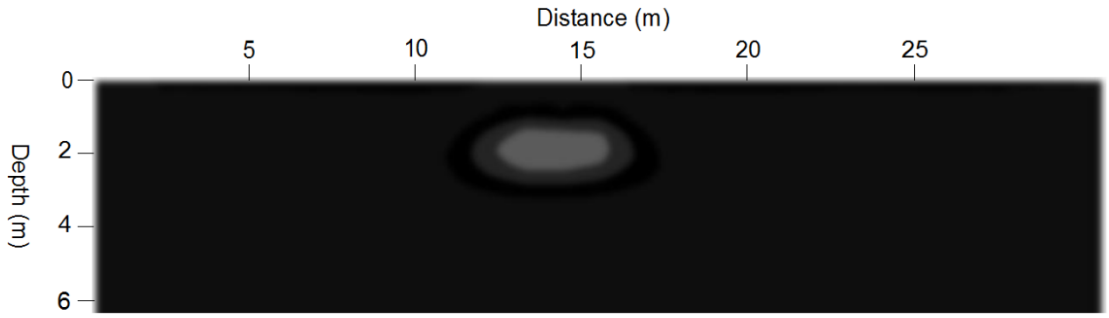

Filtered resistivity image using Gaussian blur filter

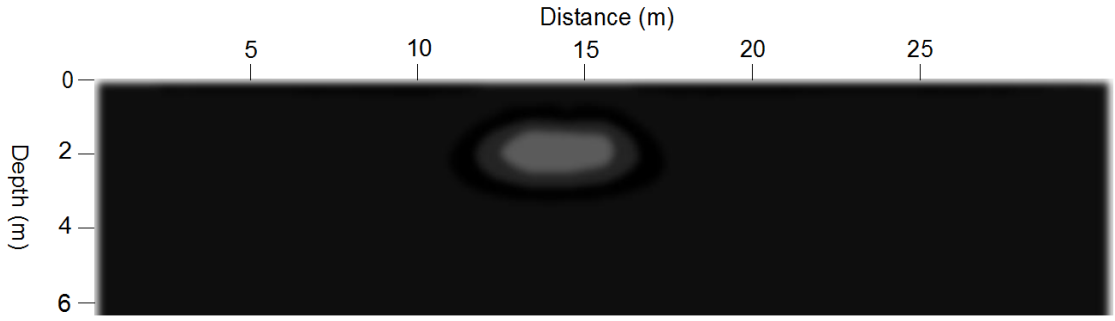

Filtered resistivity image using mean filter

[d] Applying the watershed algorithm on the filtered image.

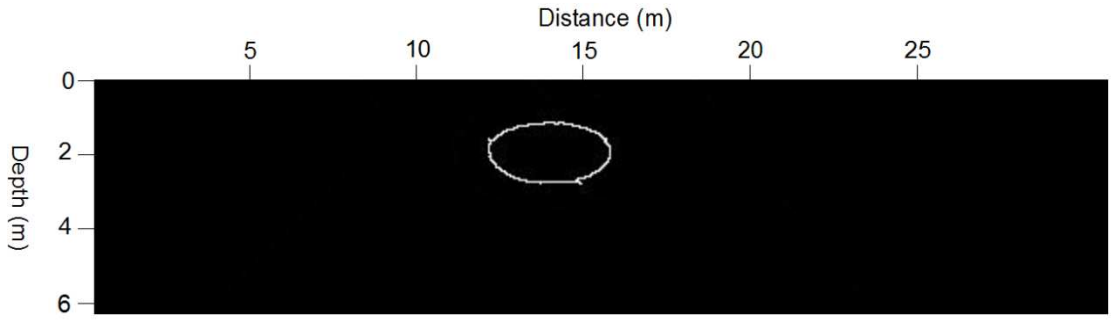

Results of applying the watershed algorithm on the filtered image

Note: the Gaussian blur and mean filters are necessary to prevent over segmentation as shown in the figure below.

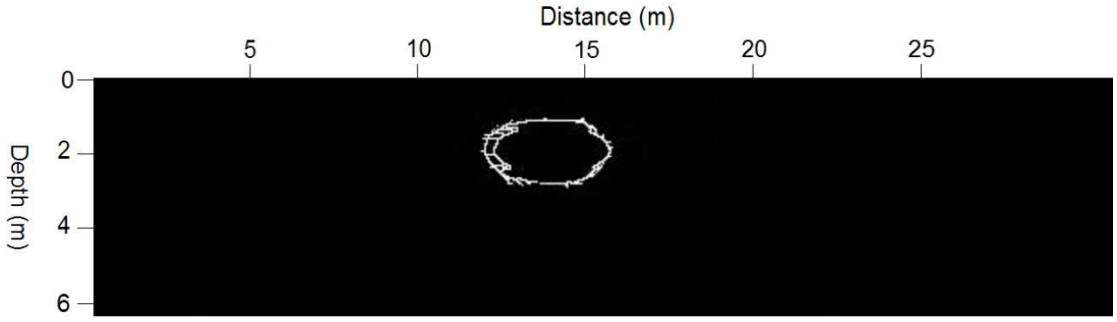

Results of applying the watershed algorithm on the unfiltered image

[3] Inverting the data using the disconnect inversion approach

Most commercially (or academically) available resistivity inversion codes such as Res2dinv allows for the direct incorporation of known boundaries in the inversion process. Following the application of watershed algorithm, the x and z locations of the predicted boundaries are used as priori information in the disconnect inversion approach.

Appendix II: Applying the watershed algorithm coupled with the L1 norm and Artificial Neural Networks (ANN).

[1] Required codes:

[a] 2D resistivity forward modeling and inversion code.

[b] A digital image processing code with the watershed algorithm included.

[c] ANN software such as Neurosolutions and Matlab (with Neural Networks toolbox included).

[2] Instructions for training the ANN:

[a] Creating resistivity synthetic data that represent a wide range of possible expected targets at field sites, and contaminating that data with noise levels similar to those expected when collecting the real data.

[b] Inverting the data using the L1 norm approach by assuming correct, underestimate and overestimate noise levels.

[c] Applying the watershed algorithm on the inverted models and extracting the input parameters for the ANN as shown in the figure below (i.e., host medium resistivity and central resistivity value of each target anomaly, and depth, width, and height of each target anomaly).

[d] Training the ANN by using as an input the extracted parameters from the L1 norm and watershed algorithm, and using as an output the actual parameters of the synthetic targets.

[3] Notes:

[a] The performance of the ANN will significantly improved if the ANN is trained using field data in addition to synthetic data.

[b] The ANN could be trained to recover targets that have irregular geometries by increasing the number of inputs for each parameter. For example, the depth of a target could be defined using three values instead of one; one value at each end of the target surface and one value at the center.

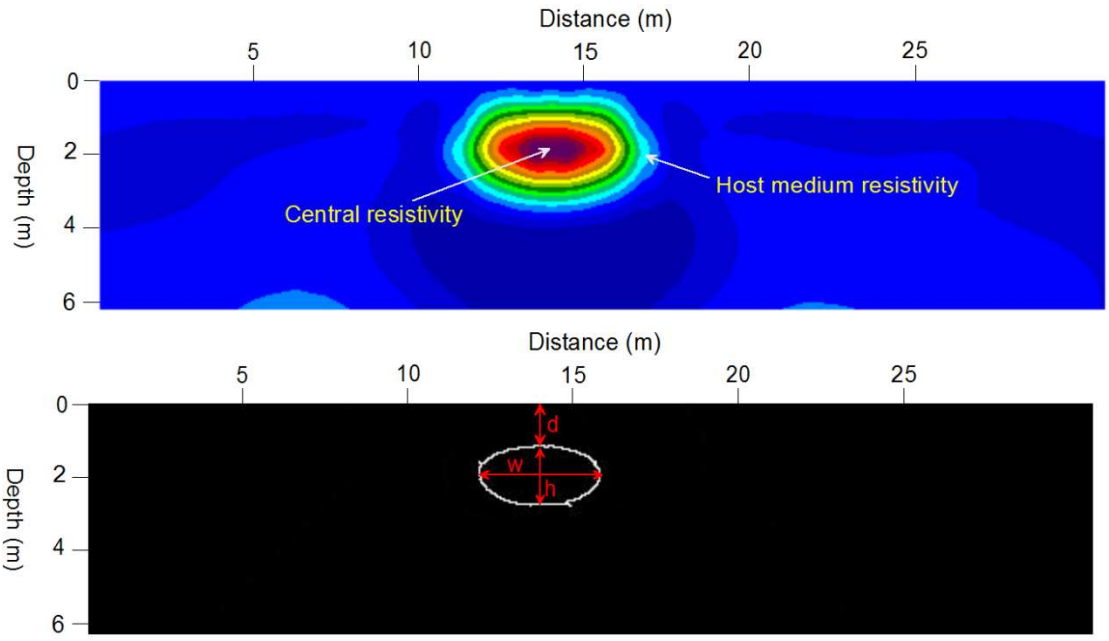

Extracting the input parameters for the ANN. Note that the host medium resistivity value should be defined using the resistivity value of the same color contour for all models, and the target's width (w), depth (d), and height (h) are extracted at the middle of the watershed boundary.

Apendix III: Iterative disconnect inversion

[1] Required codes:

Open source 3D resistivity inversion code such as RESINVM3D.

[2] Instructions for the approach:

The resistivity code should be modified such that the edge detector method is applied on the smoothness constraint resistivity model that obtained from the first iteration. The model weighting matrix is then updated by defining small weighting values at the locations of the predicted boundaries. The later step will initiate the disconnect inversion procedure, which will continue until the solution converges.

Appendix IV: Geophysical and Hydrological Investigations at the West Bank of Nile River (Luxor, Egypt)[1]

Abstract

Luxor, the modern Egyptian city that occupies the site of ancient Thebes, is famed for its magnificent ancient monuments. Since 1967 the Aswan high dam has prevented the annual flooding of the Nile River, resulting in excessive salt accumulation on the Nile floodplains and on exposed monument surfaces. In addition, the expansion of agricultural land within the Luxor study area has resulted in increased salinity and groundwater level. These conditions accelerate the degradation of buried and exposed monuments that were fairly well preserved in the past. To mitigate this problem, it is necessary to first understand the near-surface setting and the groundwater conditions of the Luxor area. A geophysical investigation was carried out using resistivity and electromagnetic surveys. Additionally, a chemical analysis was conducted of some surface water samples collected from canals and the sacred lake of Memnon Temple. Based on the results of the geophysical surveys and the chemical analysis of the water samples, the shallow subsurface was characterized into four geoelecterical units. Groundwater flow directions were determined to be from the central area to the west, causing a rise in the groundwater levels and groundwater salinity in the area of monuments.

[1]This paper has published as: Elwaseif, M., Abdalla, M., Abdel-Rahman, M., and Ismail, A., 2012, Geophysical and Hydrological Investigations at the West Bank of Nile River (Luxor, Egypt), Environmental Earth Sciences Journal, doi: 10.1007/s12665-012-1525-2

Introduction

Luxor, Egypt, occupies the site ancient Thebes, which was known for its buildings and many large gates. The west bank of Luxor (Figure 1) contains more than thirty known limestone temples, most of them built by the rulers of the New Kingdom (1549-1069 BC). Both buried and exposed archaeological features are affected by the high level of saline groundwater at the west bank of Luxor area since the construction of Aswan high dam and the resultant expansion of agricultural lands around the temples' area. Saline groundwater is transported into the monuments' foundations through underlying soil by means of capillary rise. When those saline waters evaporate, residual salts accumulate on the surface and within the pore spaces of the foundations. The pressure developed during crystallization and hydration of the residual salts exfoliates the outer layers of the foundations' stone, increasing their susceptibility to erosion by wind and other physical processes (Rodriguez-Navarro and Doehne 1999). Figure 2 shows an example of the monuments' degradation at Habu Temple in the west bank of Luxor.

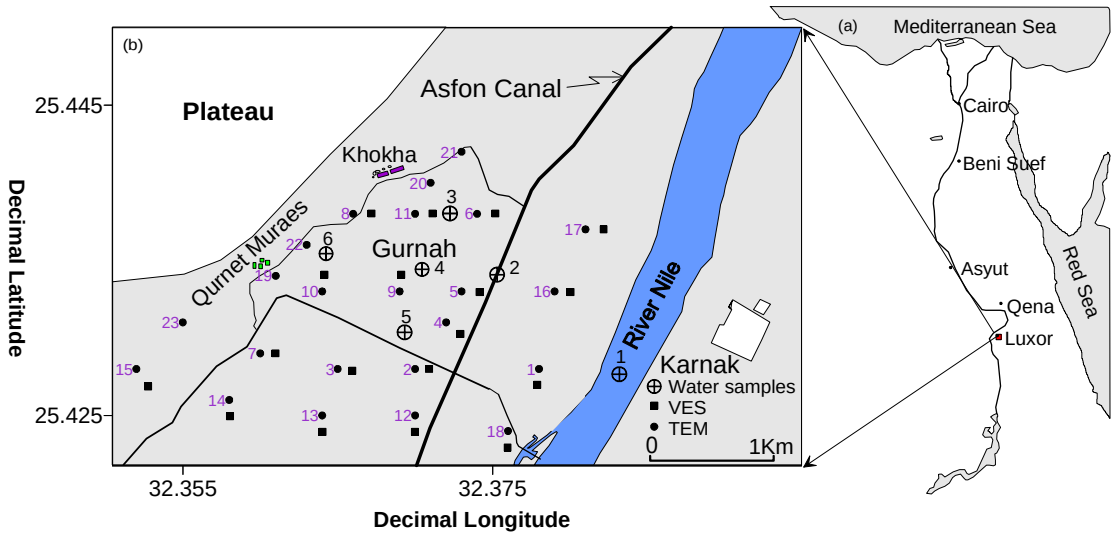

Figure 1: Location map of a- Egypt, and b- Luxor study area including the locations of collected water samples, VES and TEM data.

Geophysical methods have been widely applied to groundwater exploration (e.g., Asfahani 2007; Ismail 2003; Albouy et al. 2001). Asfahani (2007) employed vertical electrical sounding (VES) at the Khanasser Valley (Syria) and successfully identified the nature and geometry of a deep aquifer. Ismail (2003) conducted a study to mitigate the degradation of monuments on the east bank of Luxor, employingVES and seismic surveys to characterize the hydrostratigraphy of the shallow subsurface. Albouy et al. (2001) examined the merits of using VES and transient electromagnetic (TEM) methods for coastal groundwater exploration north of Biarritz and at two selected sites at the flanks of le Piton de la Fournaise, France. Those scientists showed that joint inversion of VES and TEM data is an efficient tool to resolve the ambiguity of each measurement method alone, especially in the absence of supportive geological information such as well log data.

Figure 2: Effects of shallow saline groundwater on the Habu temple (note the severe cracks and salt accumulations)

The TEM method is an electromagnetic induction technique by which the response of the earth to an electromagnetic impulse is measured in the time domain. The VES method uses direct current to measure the resistance of the subsurface using grounded steel electrodes. Although electrical resistivity and electromagnetic techniques measure the same physical property, soil resistivity, the techniques are sensitive to different characteristics (Gomez-Trevino and Edwards 1983; Raiche et al. 1985). Well-resolved electrical resistivity data obtained using the VES method are the product of layer resistivity and layer thickness (Fitterman et al. 1988). Such data do not provide good independent estimates of layer resistivity and layer thickness. In contrast, electromagnetic methods are good for establishing the thicknesses of layers but not their resistivity values (Fitterman et al. 1988). The combined inversion of TEM and VES data constrains the resistivity-depth geophysical model and reduces ambiguities in the interpretation of the measurements (Sasaki 1989; Sandberg 1993; Albouy et al. 2001).

In this study, a large-scale geophysical survey was conducted and chemical analysis performed of surface water samples at the west bank of the Nile River (west Luxor area) to characterize the near subsurface hydrogeologic setting and to identify the sources responsible for increasing the salinity of groundwater. The geophysical survey is in the form of integrated TEM and VES measurements. The groundwater analysis included chemical analysis of six surface samples collected from areas adjacent to the degraded monuments. The results of this study will be critical to developing conservation plans for the existing archaeological structures.

2. Study area

The study area, located on the alluvial plains of the Nile Valley and surrounded by elevated structural plateaus capped by Eocene limestone, is underlain by Paleocene shale (Figure 3). The alluvial plains generally exhibit flat surfaces that gently slope northward. The average ground surface elevation is about 75.5 m above mean sea level, but rises to about 79 m at the fringes of the Nile Valley. These alluvial plains can be differentiated into (1) a densely cultivated younger plain occupying the central part of the Nile Valley and covered by Holocene silt and clay, and (2) an older reclaimed plain covered by Pleistocene sand and gravel (El Hossary 1994; Research Institute of Groundwater 1997).

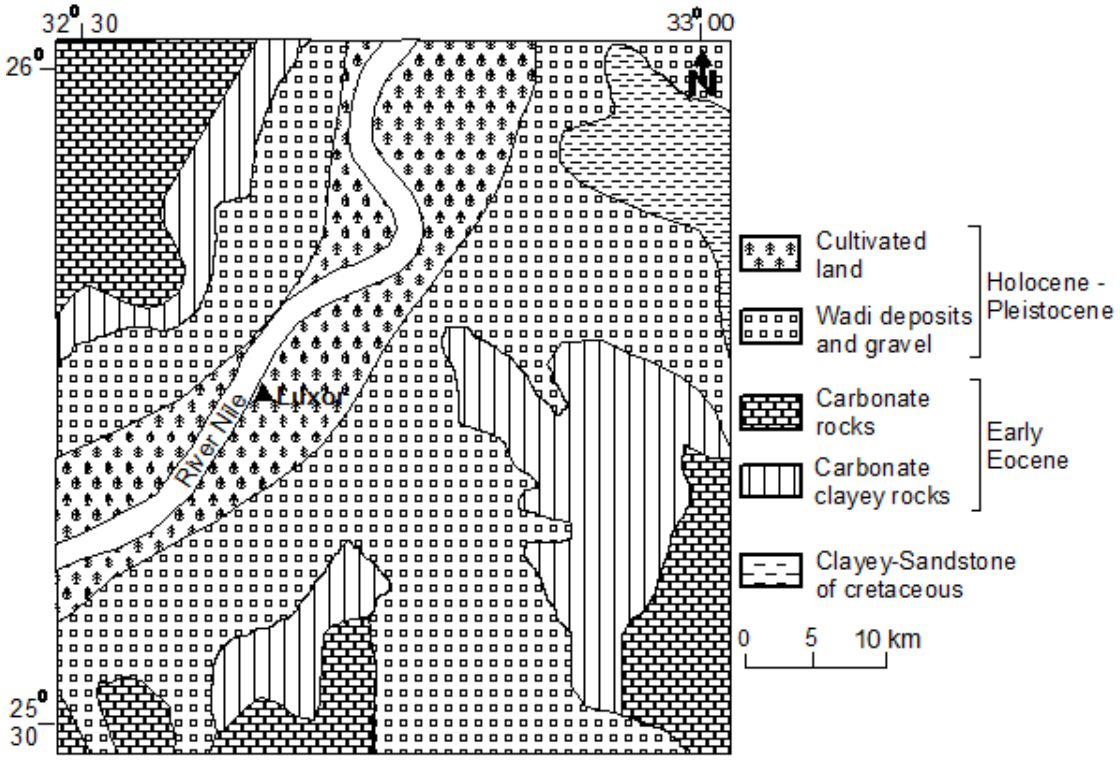

Figure 3: Geologic map of Luxor area (El Hosary, 1994)

The near-surface Pliocene-Holocene sediments in the central part of the Nile Valley rest uncomformably on a succession of Late Cretaceous-Early Eocene marine sediments. The Pliocene-Holocene sediments have been subdivided into different lithological units, each of which was deposited by an identified ancestral-modern river system (Ismail 2003), including the Eonile, Paleonile, Protonile, Prenile, and Neonile.

Two main aquifer systems are distinguished within the Pliocene-Pleistocene in the Luxor study area: the shallow Quaternary aquifer and the underlying Pliocene-Pleistocene aquifer. The Quaternary aquifer is composed mainly of graded sand and gravel and locally thickness ranges from 5 to 95 m and salinity is about 2.6 mg/L. The underlying Pliocene-Pleistocene aquifer, composed of sand and clay, is the secondary aquifer in the study area and has an average salinity value of 700 mg/L (Ismail 2003).

4. Geophysical Data Acquisition and Processing

Eighteen VESs were acquired using the Syscal R2 instrument (Figure 1). The Schlumberger electrode configuration was employed, and the maximum current electrode spacing (AB/2) varied from 300 to 400 m. The VESs were spaced at 0.5-km to 1-km intervals. The measurements were taken in the east-westdirection, perpendicular to the Nile Valley. The measured apparent resistivities from each VES were plotted simultaneously against AB/2 values on log-log paper in the field for quality control of the data.

A suite of 23 TEM soundings were measured using the SEROTEM system close to the locations of the resistivity measurements. A simple coincident loop configuration was employed; in this configuration, the same loop transmits and receives signals. The loop side length was 50 m. During data aquisition, measurements were repeated several times to ensure a high signal-to-noise ratio.

Due to the lack of boreholes at the study site and in order to roughly control the VES interpretation, the present study used the lithoresistivity model of Ismail (2003), based on two boreholes located about 200 m away from the acquired VESs at the east bank of Luxor. In that model, four litho-resistivity units were characterized: (1) an upper unit of dry silty clay with relatively high resistivity (~20 ohm-m), (2) a lower unit with significantly low resistivity (~4 ohm-m) assigned to the moist silty clay, (3) a thick unit (> 20 ohm-m) with high resistivity assigned to the main Quaternary aquifer layer, and (4) a low resistivity layer (< 4 ohm-m) assigned to a secondary aquifer layer (Figure 4a and b).

The resistivity data were first inverted in terms of one-dimensional (1-D) resistivity-depth models using software described by Zohdy (1989) and Meju (1991). The output models were used as initial models for inverting the nearby TEM data using TEMIXXL (1996) software. The resultant TEMIXXL models were used again as initial models for inverting the resistivity data in RESIST (1988) software. The misfit errors between the measured and calculated models for the whole data set range from 2.8 and 7.3% (Figure 4c and d). This iterative method was continued until reliable resistivity-depth models were obtained

that seemed to be consistent with the subsurface geologic setting. The final models were interpolated to generate 2-D resistivity cross sections parallel and perpendicular to the Nile River.

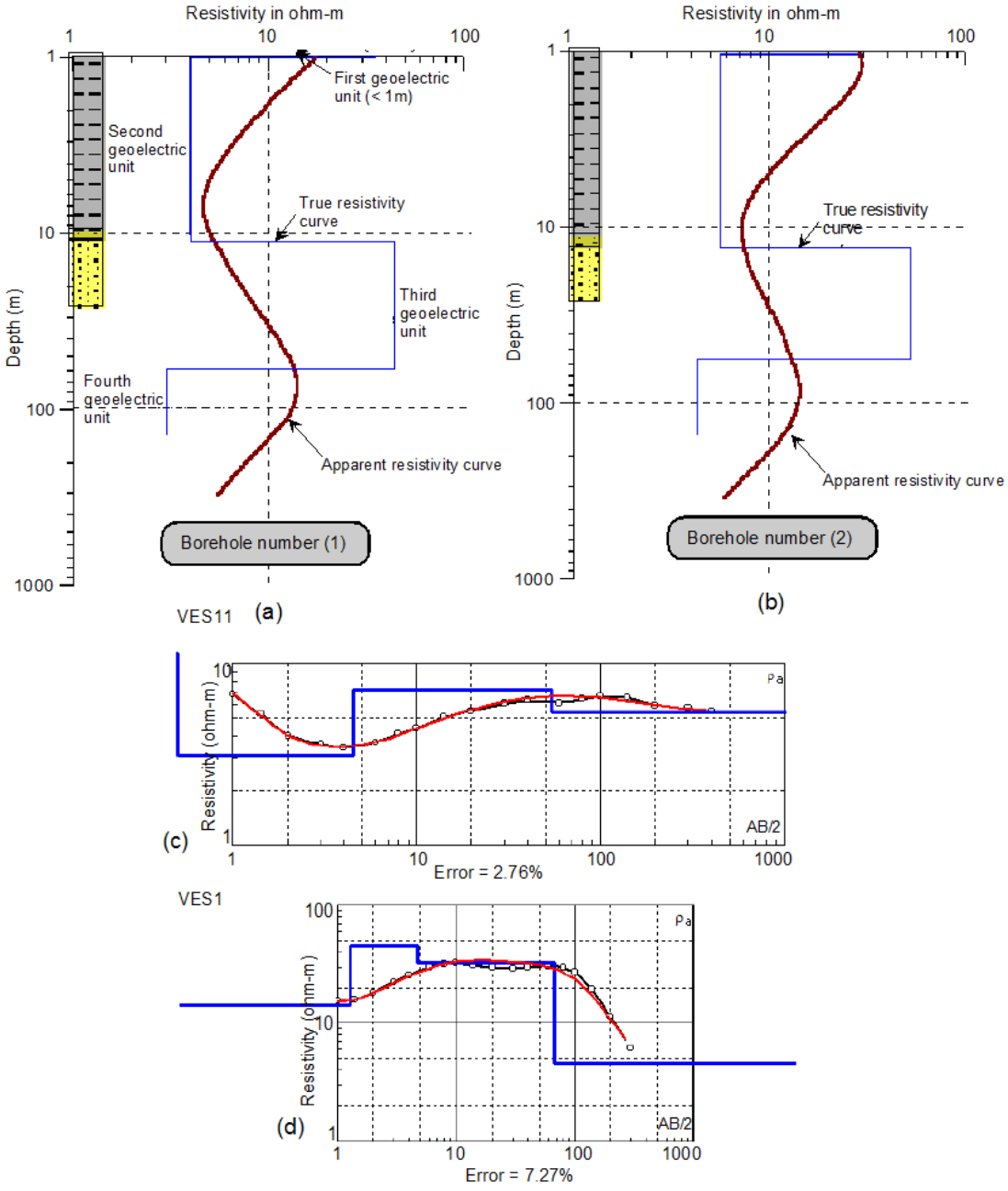

Figure 4: Calibration of the measured apparent resistivity with the corresponding lithologic units at two boreholes (a and b), c and d are the processing results of two VESs (after Ismail, 2003)

5. VES and TEM results

Based on the joint inversion of resistivity and electromagnetic data, two geoelectrical resistivity cross sections were generated, one parallel to the Nile River, and the other perpendicular to the Nile (Figures 5 and 6). The geoelectrical resistivity cross sections exhibit four geoelectrical units. No significant lateral resistivity variation was found within individual units:

1- The first (upper) geoelectrical unit consists of (1) a relatively dry silty clay agricultural soil less than 4 m thick with resistivity values ranging from 5 to 28 ohm-m, and (2) dry silty clay and gravel soil, having a resistivity value of 50 ohm-m and a thickness of 2 m.

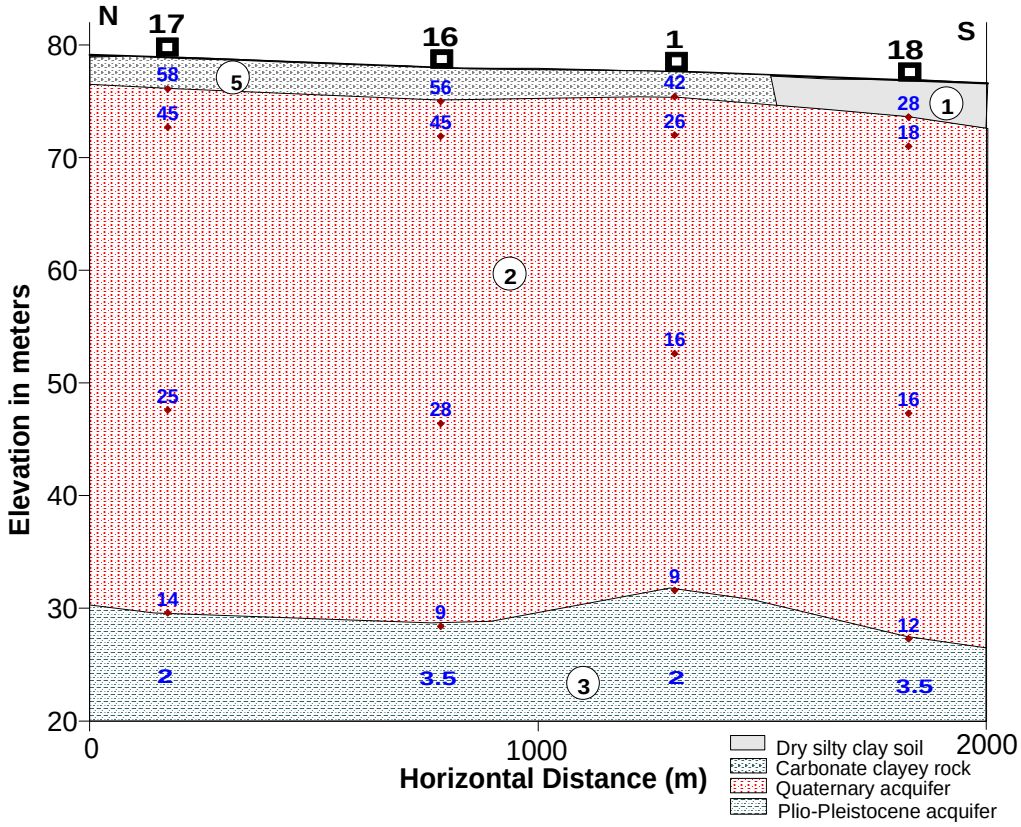

Figure 5: Geoelectrical cross-section extending parallel to the River Nile

2- The second geoelectrical unit consists of sand, silt, and gravel of the main Quaternary aquifer. The average resistivity value is 20 ohm-m, andthickness is about 48 m. The thickness of the aquifer layer decreases significantly toward the west plateau.

3- The third geoelectrical unit is characterized by low resistivity value (< 5 ohm-m) and thickness ranging from about 4 m near the Nile River to about 48 m near the western plateau. This unit represents the secondary aquifer in the study area (Pliocene-Pleistocene aquifer). The significant resistivity contrast between the Quaternary aquifer and the underlying Pliocene-Pleistocene aquifer is attributed to the higher salinity (700 mg/L vs. 2.6 mg/L) and clay content of the sediments within the Plio-Pleistocene aquifer (Ismail 2003).

4- The fourth geoelectrical unit is characterized by a resistivity value of about 10 ohm-m. This unit appears only at the base of the plateau area at a depth of 2 m to 5 m. This unit represents the Paleocene shale layer. Its low resistivity is due to lateral seepage of groundwater from the adjacent Pliocene-Pleistocene aquifer. A normal fault separates the third and fourth units, and this fault was traced on the resistivity section of Figure 11. The location and orientation of this fault seem to be consistent with the major fault forming the Nile Valley in this area (El Hosary 1994).

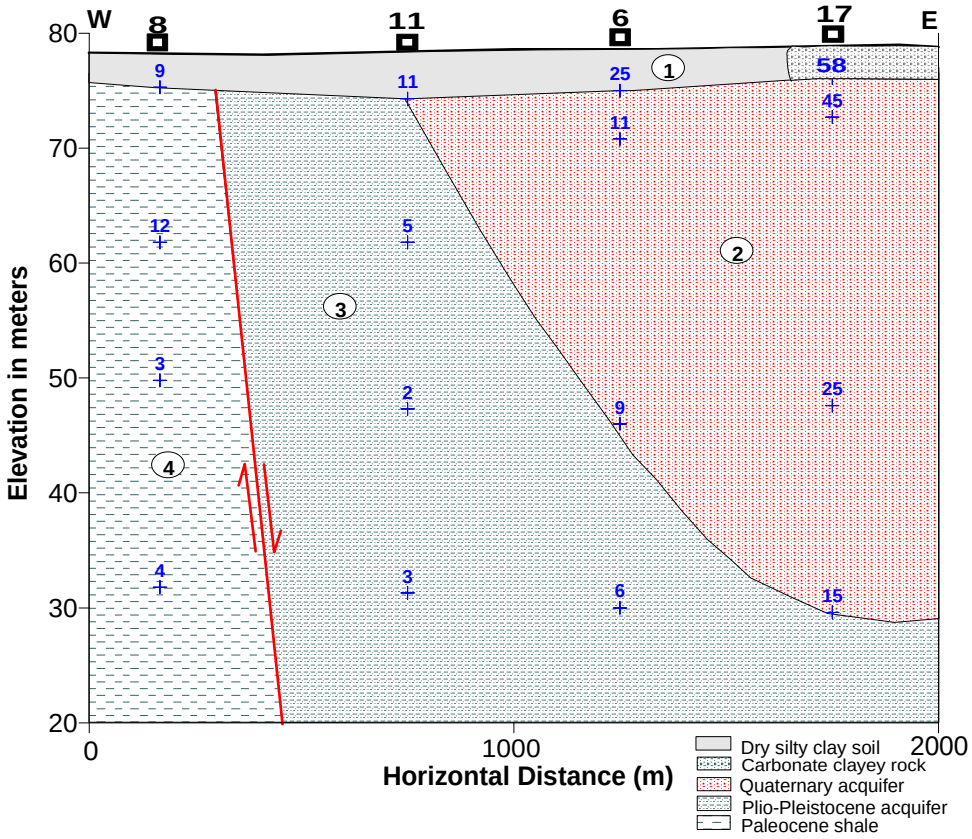

Figure 6: Geoelectrical cross-section extending perpendicular to the River Nile

The inverted resistivity, or “true” resistivity, of each of the specified geoelectric units was mapped to better demonstrate the lateral resistivity variation with depth and its possible impact on the degradation of the area’s monuments.

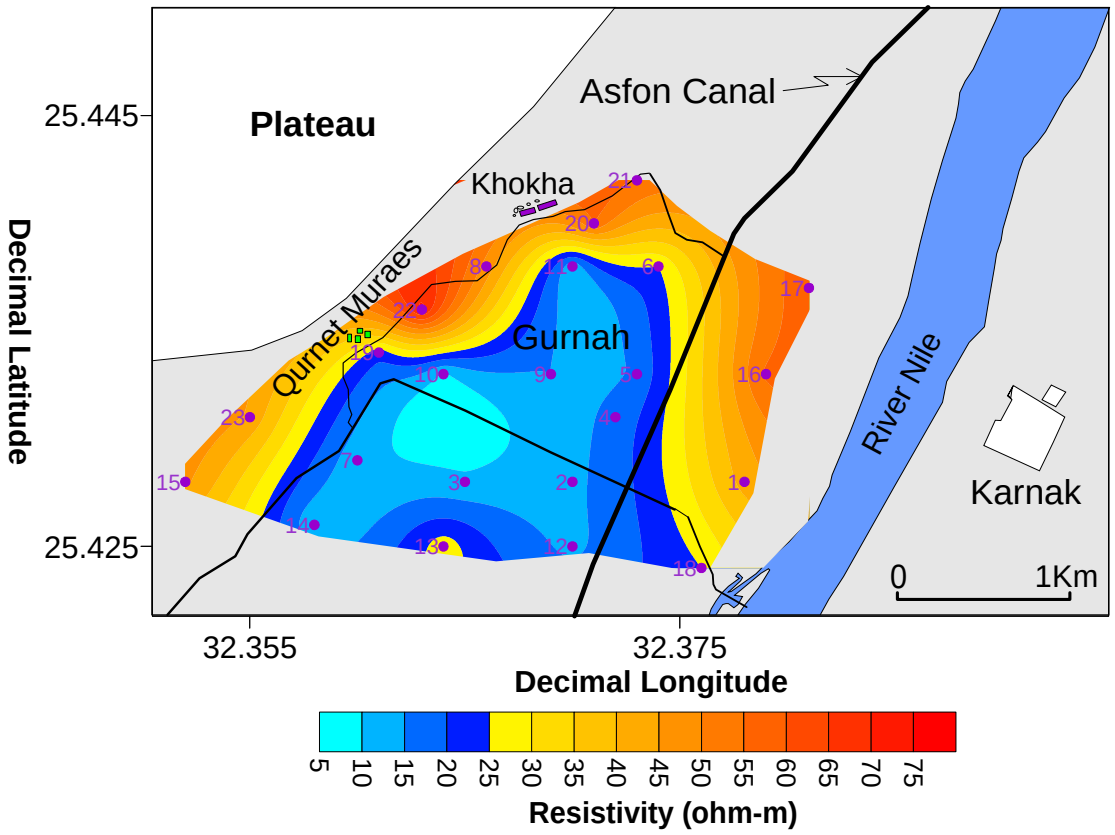

Figure 7: Spatial resistivity distributions at 1 m depth

Resistivity distribution at 1 m depth: The first unit represents the dry silty clay topsoil. The resistivity values of this unit vary from 5 to 75 ohm-m (Figure 7). Although surface conditions, such as farming and urbanization, affect resistivity distribution, the values still provide a good indication of the moisture and/or salinity distribution within the topsoil, which is in direct contact with the archaeological features. The high-resistivity values of 25 to 75 ohm-m are observed near the urban areas (parallel to the Nile River) and near the limestone plateau. The low resistivity values of less than 24 ohm-m are found for the central cultivated areas in the study site. These low values are a direct result

of increased moisture content due to irrigation and increased salinity caused by excessive evaporation and use of fertilizers.

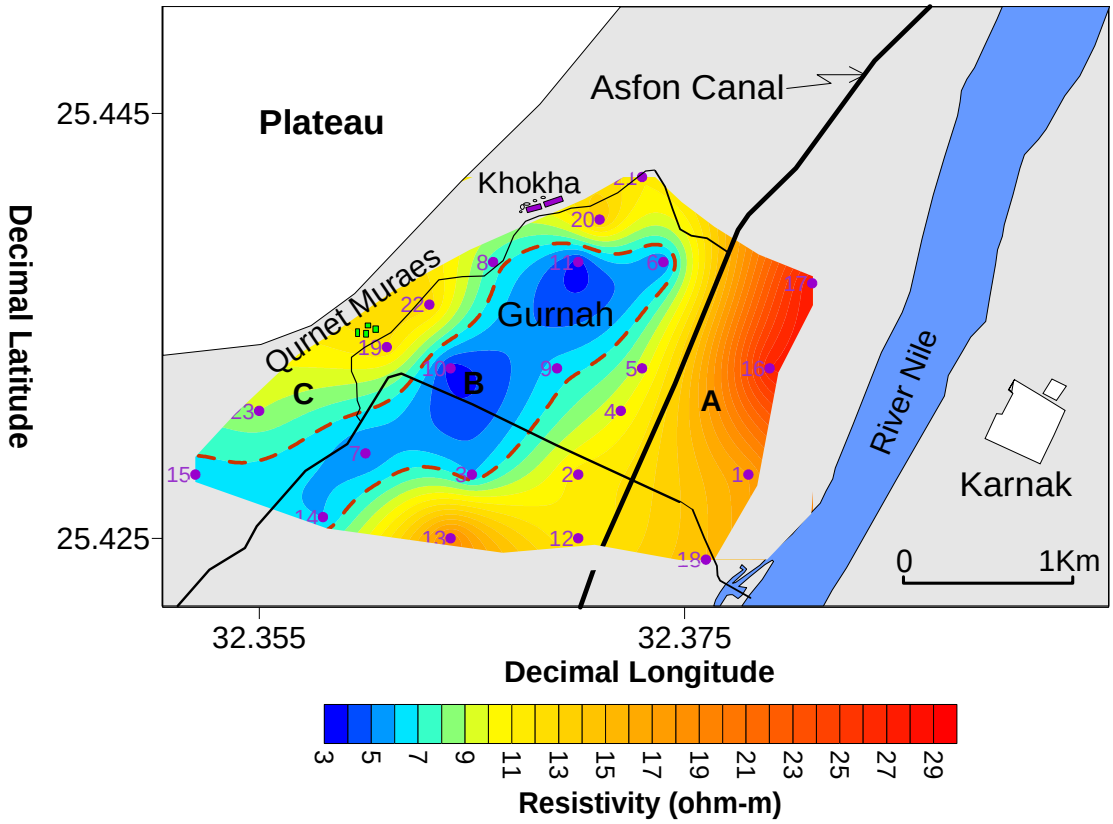

Figure 8: Spatial resistivity distributions at 4 m depth

Resistivity distribution at a depth of 4 m: This unit has resistivity values range from 3 and 29 ohm-m and is characterized by three main resistivity zones (A, B and C), which correspond to the second, third, and fourth geoelectrical units, respectively (Figure 8). Resistivity values range from 10 to 29 ohm-m for Zone A, which represents the saturated sand and silt sediments of the Quaternary aquifer. The water within this aquifer seems to be fresh and originating from the Nile and irrigation canals (e.g., Asfon canal) in the

study area . The resistivity value is low (5 ohm-m) for Zone B, which representsthe Pliocene-Pleistocene aquifer in the study area. Zone C, representing the Paleocene shale, has resistivity values ranging from 8 to 16 ohm-m, probably because of its high moisture content and/or salt.

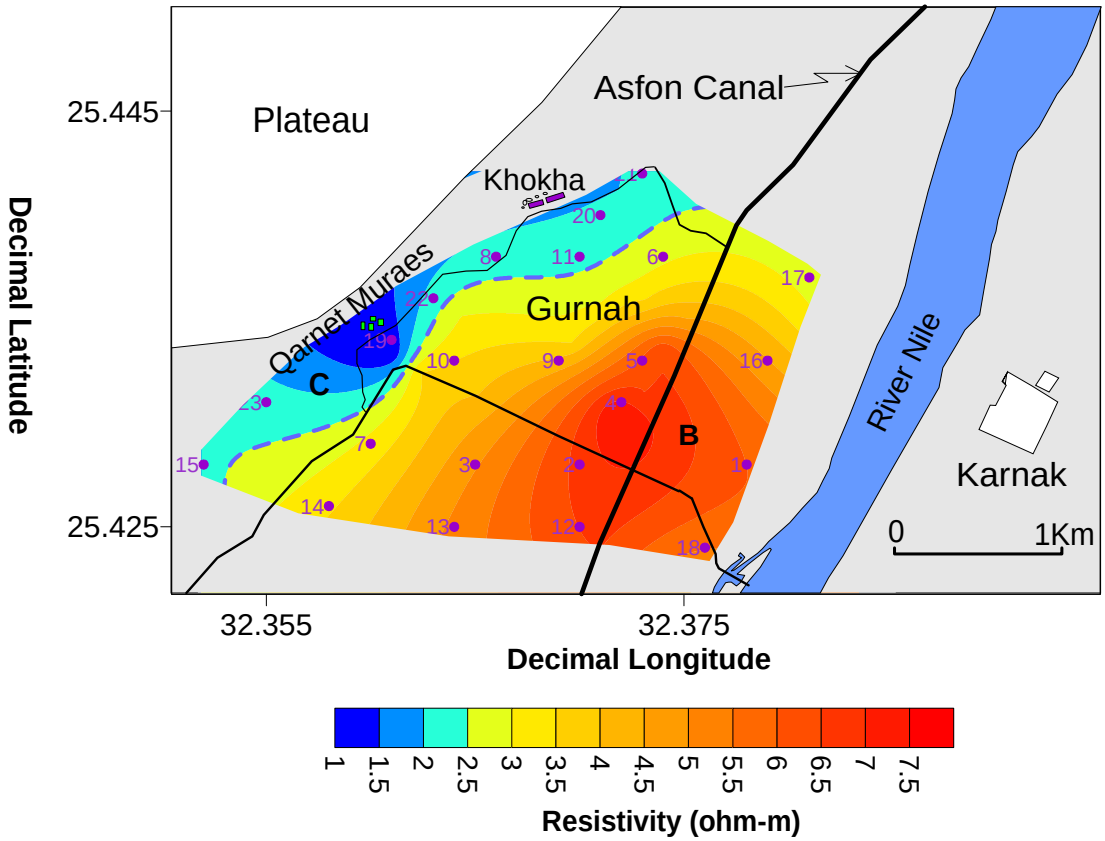

Figure 9: Spatial resistivity distributions at 48 m depth

Resistivity distribution at 48 m depth: This unit has low resistivity values ranging from 1 to 7.5 ohm-m. Although the range is narrow, Zones B and C are obvious, as shown in Figure 9. Zone B resistivity values range between 2.5 and 7.5 ohm-m. This zone is probably an extension of the Pliocene-Pleistocene aquifer that consists of sand with

clayey sediments. Zone C, which corresponds to the moist Paleocene shale layer, exhibits a very low resistivity value of 2 ohm-m.

To better visualize the surface and subsurface at the study site, we constructed a composite model that shows the spatial resistivity distribution of subsurface geoelectrical units, the surface location of temples, cultivated areas, and the Nile River. As shown in Figure 10, the Nile River does not contribute to the groundwater recharge in the study area, since the resistivity values of different strata increase toward the east (i.e., toward the Nile), which is consistent with the conclusion of Ismail (2003). The groundwater flow seems to flow from west to east, and, in the surface layer, from the cultivated areas outward.

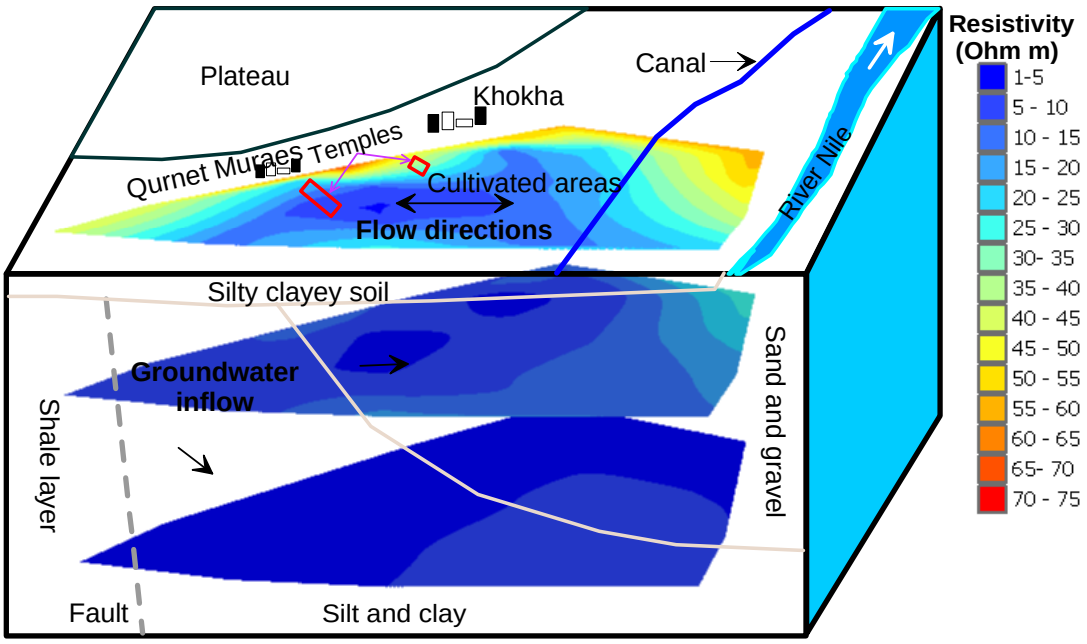

Figure 10: Composite model of Luxor study area

6. Chemical analysis of the water samples

Results of the chemical analysis of water samples can be integrated with the geophysical interpretation to yield valuable information on the causes of increasing salinity and groundwater level at Luxor study area. Six surface water samples were collected from the study area from the Nile River, the canals, and the sacred lake of Memnon Temple. The results of the chemical analyses are presented in Table 1. The sources of different ions in the examined water could be grouped as follow:

Table 1: Results of geochemical analysis of water samples (Figure 5 shows the location of these samples)

Sample No.	pH	T.D.S	Anions (ppm)				Cations (ppm)				EC
			CO_3^{-2}	HCO_3^{-1}	Cl^{-1}	SO_4^{-2}	Na^{+1}	K^{+1}	Ca^{+2}	Mg^{+2}	
1	8.3	217.6		122	28	28	36	1.17	16.5	12	340
2	8.2	211.2		134	22	23	41	1.17	14	9.5	330
3	8.2	211.2		122	25	28	38	1.17	12	12	330
4	8.2	217.6		134	24.5	24	38	1.6	14	12	340
5	8.3	204.8		134	21	19	41	1.17	10	11	320
Temple	8.3	716.8	30	354	190	96	195	3.5	22	18	1120

6.1. Cultivated lands

Sodium (Na^{+1}), an essential constituent used in fertilizers (e.g., Phillips et al. 2001), was 195 ppm in water sampled at Memnon Temple compared with 36 ppm from the River Nile. The high sodium concentration observed at the temple is evidence that the water inside the monument migrated from the nearby cultivated lands.

Potassium (K^{+1}) is an essential plant nutrient (e.g., Mengel and Kirby 1980). Potassium is highest (3.5 ppm) in the water sample taken from Memnon Temple, again supporting the interpretation that this water migrated from the surrounding cultivated areas.

Sulfate (SO_4^{-2}) is derived from gypsum, acid rains, and fertilizers (Garg 1978). The highest concentration (96 ppm) of sulfate is observed at Menmon Temple, indicating that its water probably comes from nearby cultivated areas.

Chloride (Cl^{-1}) is mostly presented either as salt crystals or in solution (Na^{+1} and Cl^{-1} ions) (Hem 1970). The concentration of chloride ranges from 21 ppm at the eastern side of the study area to 190 ppm at Memnon Temple. The high concentration of chloride at the temple is related to the successive accumulations of water inside the temple that probably migrated from cultivated areas.

6.2. Weathering of monuments/temples

Calcium (Ca^{2+}) and magnesium (Mg^{+2}**)** are the principal minerals forming carbonate rocks such as limestone ($CaCO_3$) and dolomite ($CaMg\ [CO_3]_2$). The highest calcium (22 ppm) and magnesium concentrations (18 ppm) were observed at Memnon Temple, probably due to the dissolution of carbonate rocks forming its stone foundations.

Bicarbonates (HCO_3^{-1}) are formed when carbon dioxide is dissolved or derived from limestone (e.g., Rogers et al. 1985). The bicarbonate concentration of water sampled from the Nile River is 122 ppm; from the irrigation channels, 134 ppm; and at Memnon Temple, 354 ppm. The high concentration of bicarbonate at Menmon Temple is because of the dissolution of the limestone of its stone foundations.

6.3. Natural sources

The pH value of water is a measure of the concentration of hydrogen ions (H^+). The pH values of the water samples from the study area vary between 8.2 and 8.3, indicating alkalinity and the dissolution of calcium and magnesium ions in the water samples (e.g., Psenner 1988). Electrical conductivity of surface waters increases from east (320 micro S/cm) to west at Menmon Temple (1120 micro S/cm). Water with high electrical conductivity contains sodium and magnesium cations as well as calcium, chloride, and bicarbonate anions (e.g., Freund et al. 1993). As expected, total dissolved solids (TDS) was highest (716.8 mg/l) in the water sample collected from the sacred lake of Memnon Temple and lowest (204.8 mg/l) in the water samples from canals in the eastern side of the study area. The high TDS value from the Memnon Temple is due to the evaporation of the water in the temple's sacred lake.

7. Discussion and conclusions

The joint inversion of VES and TEM data and the results of chemical analyses of water samples were successfully integrated to generate a suite of geoelectric resistivity cross sections and subsurface maps. The main disadvantage of the employed techniques is the

limited spatial subsurface coverage and the uncertainty when generating the 2-D cross sections. Obviously, 2-D/3-D techniques (e.g., resistivity and ground-penetrating radar) would produce more subsurface coverage and more accurate models. Those techniques, however, are probably not the best choice at this site given the large survey area, time constraints, and, most importantly, because the goal of this present study is not the detailed hydrogeology of the field site. Furthermore, the methods employed in the present study are inexpensive, data acquisition is quick, and achievable penetration depth can be very deep (depending on AB/2 spacing and the loop size of the TEM survey).

Study results indicate that the shallow subsurface in the Luxor study area is divided into four distinct geologic/hydrologic units. Such characterization represents the foundation of any plan to lower the groundwater level and decrease the salinity of capillary soil moisture in the area of the Luxor monuments. Shallow groundwater flow paths were expected to have originated from the recently cultivated areas west of Luxor and to flow toward the River Nile. The elevated groundwater in the area of the temples appears attributable to flood irrigation of recently reclaimed lands lying on the alluvial/floodplain transition. The progressive increase in salinity along the groundwater flow path is reflected in the recent deposition of precipitated salts observed at Habu Temple (Figure 2). Based on our interpretation of the acquired data and the field observations, the salt accumulation on the foundations of the monuments appears to be ascribable to salt transport by capillary water from the relatively high salinity groundwater or from connate water in the silty clay unit.

As a final comment on the study area, recommendations are to avoid cultivation of crops that require much water and to regulate the use of agricultural chemicals in areas of thin silty clay soil. Further recommendations are to conduct high-resolution geophysical surveys (e.g. 3-D electrical resistivity) and detailed chemical analysis of the water proximal to the Luxor monuments. These suggestions might reduce the groundwater discharge at the temple areas and reduce its effects on the stone foundations.

References

Albouy Y, Andrieux P, Rakotondrasoa G, Ritz M, Descloitres M, Join J, Rasolomanana, E. (2001), Mapping coastal aquifers by joint inversion of DC and TEM soundings–Three case histories. Groundwater 39: 87-97

Asfahani J (2007) Geoelectrical investigation for characterizing the hydrogeological conditions in semi-arid region in Khanasser valley, Syria. J Arid Environ 68: 31-52.

Domenico PA, Schwartz FW (1990) Physical and chemical hydrogeology. Wiley, New York.

El Hosary M (1994) Hydrogeological and hydrochemical studies on Luxor area, southern Egypt. MSc Thesis, Ain Shams University, Cairo, Egypt.

Fitterman D, Meekes J, Ritsema I (1988) Equivalence behaviour of three electrical Sounding methods as applied to hydrogeological problems. European Association of Exploration Geophysics, 50th Annual Meeting Technical Exhibition, The Hague, the Netherlands, 21 p.

Freund F, Freund M, and Batllo F (1993) Critical review of electrical conductivity measurements and charge distribution analysis of magnesium oxide: J Geophys Res98 (12): 209-230.

Garg S (1978) Groundwater and tube wells. Oxford and IBH Publishing, 333 p.

Gomez-Trevino E, Edwards R (1983) Electromagnetic soundings in the sedimentary basin of southern Ontario- A case history. Geophysics 48: 311-326.

Ismail A (2003) Geophysical, hydrological, and archaeological investigation in the east bank area of Luxor–southern Egypt, PhD thesis, Department of Geology and Geophysics, University of Missouri-Rolla, USA.

Meju M (1991) SLINy, V Ver. 1.1 A, A user-friendly Schlumberger resistivity forward and inverse modelling program. Schlumberger.

Mengel K, and Kirkby EA (1980) Potassium in crop production. Advan Agron 33 59-110.

Phillips C, Tenlep S, Pennell K, Omed H, and Chi P (2001) The effect of applying sodium fertilizer on the rate of digestion of perennial ryegrass and white clover incubated in rumen liquor, with implications for ruminal tympany in cattle. Vet J 161: 63-70.

Psenner, R (1988) Alkalinity generation in a soft-water lake: Watershed and in-lake processes. Limnol Oceanogr 33: 1463-1475.

Raiche A, Jupp D, Rutter H, Vozoff K (1985) The joint use of coincident loop transient electromagnetic and Schlumberger sounding to resolve layered structures. Geophysics 50: 1618-1627.

Research Institute of Groundwater (1997) Hydrogeological map of Luxor area, Scale 1:100 000. Explanatory notes.

Rodriguez-Navarro C, Doehne E (1999) Salt weathering: Influence of evaporation rate, super saturation and crystallization pattern. Earth Surface Processes Landforms 24: 91–209.

Rogers JA, Muller LD, Davis CL, Chalupa W, Kronfeld DS, Karcher LF, and Cummings KR (1985) Response of dairy cows to sodium bicarbonate and limestone in early lactation: J Dairy Sci 68 (3): 646-660.

Sandberg S (1993) Examples of resolution improvement in geoelectrical soundings applied To groundwater investigations. Geophys Prospect 41: 207-227

Sasaki Y (1989) Two-dimensional joint inversion of magnetotelluric and dipole-dipole resistivity data. Geophysics 54: 254-262.

TEMIXL XL V4 (1996) Temix V.4 user's manual, Interprex, 468 p.

Vander V (1988) Resist, a computer program for the interpretation of resistivity Sounding curves. An ITCD M. Sc. Research Project. ITCD, Delft, the Netherlands.

Zohdy A (1989) The use of Schlumberger and equatorial sounding in groundwater investigations near El-Paso, Texas. Geophysics 34: 713-728.

VITA

Mehrez H. Elwaseif

1980	Born June 11 in Alkordy, Egypt.
1996	Graduated Alkordy High School, Alkordy, Egypt.
1997-2001	B.Sc. in Geophysics Mansoura University, Mansoura, Egypt.
2002-2007	Assistant Researcher, National Research institute of Astronomy and Geophysics, Cairo, Egypt.
2004-2006	M.Sc. in Geophysics, Ain-Shams University, Cairo, Egypt.
2007-2012	Ph.D. Student, Rutgers University, Newark, New Jersey.
2007-2011	Teaching Assitant, Rutgers University, Newark, New Jersey.
2010	Peer-reviewed article: Elwaseif, M., Slater, L., Soliman, M., and Mesbah H, 2010, Improving Fractured Rock Characterization from Time Frequency Analysis of GPR Datasets , In, Miller, R., Bradford, J., and Holliger, K., (ed.) Advances in Near-Surface Seismology and Ground-Penetrating Radar, SEG publications, ISBN 978-1-56080-224-2.
2010	Peer-reviewed article: Elwaseif, M., Slater, L., 2010, Quantifying Tomb Geometries in Resistivity Images Using Watershed Algorithms: Journal of Archaeological Science, Vol. 37, Issue 7, pp 1424-1436.
2011- 2012	Graduate Fellowship, Rutgers University, Newark, New Jersey.
2012	Peer-reviewed article: Elwaseif, M., and Slater, L., 2012, Improved Resistivity Imaging of Targets with Sharp Boundaries Using an Iterative Disconnect Procedure, Journal of Environmental and Engineering Geophysics, in press.
2012	Peer-reviewed article: Elwaseif, M., Abdalla, M., Abdel-Rahman, M., and Ismail, A., 2012, Geophysical and Hydrological Investigations at the West Bank of Nile River (Luxor, Egypt), Environmental Earth Sciences Journal, doi: 10.1007/s12665-012-1525-2.
2012	Peer-reviewed article: Mwakanyamale, K. E., L. D. Slater, F. D. Day-Lewis, M. Elwaseif, and C. D. Johnson, 2012, Spatially variable stage-driven groundwater-surface water interaction inferred from time-frequency analysis of distributed temperature sensing data, Geophysical Research Letters, doi:10.1029/2011GL050824.